

# INNOVATIVE RUNNING GEAR SOLUTIONS FOR NEW DEPENDABLE, SUSTAINABLE, INTELLIGENT AND COMFORTABLE RAIL VEHICLES

## Task 2.3 – Novel Materials and Manufacturing Concept solutions

### Deliverable D2.3 Report on novel materials and manufacturing concept solutions

Due date of deliverable: 31/08/2019

Actual submission date: 02/09/2019

Leader/Responsible of this Deliverable: Roberto SORCI, Rina Consulting Centro Sviluppo Materiali

Reviewed: Y

Document status		
Revision	Date	Description
0.1	31/08/2019	First issue
0.2	13/09/2019	Intermediate for review
0.3	01/10/2019	Revised structure and contributors
0.4	02/09/2019	Final version after quality check

The information in this document is provided “as is”, and no guarantee or warranty is given that the information is fit for any particular purpose. The content of this document reflects only the author’s view – the Joint Undertaking is not responsible for any use that may be made of the information it contains. The users use the information at their sole risk and liability.

This project has received funding from Shift2Rail Joint Undertaking under the European Union’s Horizon 2020 research and innovation programme under grant agreement No 777564.

Dissemination Level		
PU	Public	X
CO	Confidential, restricted under conditions set out in Model Grant Agreement	
CI	Classified, information as referred to in Commission Decision 2001/844/EC	

Start date of project: 01/09/2017

Duration: 25 months

## REPORT CONTRIBUTORS

Name	Company	Details of Contribution
R. Sorci	RINA - CSM	Responsible of the Deliverable
A. Astri / A. Colaneri	RINA – CSM	Design and development of a new metallic alloy with improved mechanical properties for the final application
P.Farina, P.Gugliermetti, M.Gorlani	BLUE	Concept study for bogie frame
F. Braghin	POLIMI	Simulation of an innovative manufacturing processes
B. Previtali, A. G. Demir	POLIMI	Additive manufacturing by SLM



## EXECUTIVE SUMMARY

The RUN2RAIL project explores an ensemble of technical developments for future running gear, looking into ways to design trains that are more reliable, lighter, less damaging to the track, more comfortable and less noisy. In this contest, one of the main thematic work streams is the “Optimised materials & manufacturing technologies” one.

This report is focused on the use of novel materials and manufacturing methods in combination with intelligent / active suspensions to enable nonconventional running gear concepts.

BLUE performed a concept design concerning both a bogie frame and a single axle gear. In particular, after the innovative design, BLUE carried out virtual modelling and simulated manufacturing of some components, considering the candidate materials and process solutions (such as carbon fibre composites and additive manufacturing). Selected components were Axlebox and Link: indeed, both these components can be realised in innovative composite material respecting actual manufacturing requirements (Figure A).

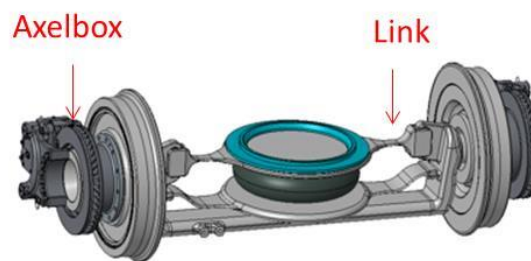


Figure A: Axlebox and Link of a bogie frame

In order to achieve lightness (that corresponds to energy saving) and high mechanical performance during working conditions, the idea is to realise the selected components by means of Additive Manufacturing (AM) processes. In fact, AM allows more degrees of freedom for designing and manufacturing components with complex shapes which would be impossible to make through traditional methods. For example, it also allows to obtain lighter structures with topological optimisation. Moreover, AM can be considered the key technology of the fourth industrial revolution, known as "Industry 4.0", which aims to improve the production methods and business models currently used in industrialized countries.

AM plays a pivotal role in changing the manufacturing paradigm and contributing to address the societal challenges of our time, such as global warming, energy transition, population ageing and decreasing resources. Today metal AM remains a niche technology because of the limited number of materials available. On the other hand, the demand for more efficient and lighter structures is continuously increasing, especially for the use of Al alloys. To answer the market demand, the development of new Al based alloys with improved properties, constitutes a key factor both in terms of process and product performance.

A review of the different AM processes has been done, based on the particular production characteristics, including the method of making the layers, raw materials and the energy source used. The ASTM F2792 - 12 standard divides AM technologies into 7 classes:

- Binder Jetting: where a liquid, acting as a binder, is selectively deposited to join powders of another material;
- Directed Energy Deposition: where a heat source is used to melt a material simultaneously with its deposition;
- Material Extrusion: where the material is selectively distributed through a nozzle or orifice;
- Material Jetting: where droplets of liquid material are selectively deposited;
- Powder Bed Fusion: where a laser source melts selected portions of the powder bed;
- Sheet Lamination: where sheets of material are joined together to create an object;
- Vat Photopolimerization: where a liquid photo-polymer is selectively cross-linked, using a radiation source.

In this context, nanomaterials may provide the leap of quality required for a wider use of AM Al-alloys. Metal Matrix Nano Composites (MMNCs) exhibit outstanding properties, especially on ductility, fracture toughness and machinability. A new aluminium alloy reinforced by alumina disperosoids has been designed and produced by Rina CSM to improve mechanical properties for the final application. In particular, the metal alloy powder was produced through VIGA (Vacuum Inert Gas Atomization). VIGA technology has the great advantage to make high-value added powders in controlled atmosphere. Obtained ODS (Oxide Dispersion Strengthened) powder are shown in Figure B.

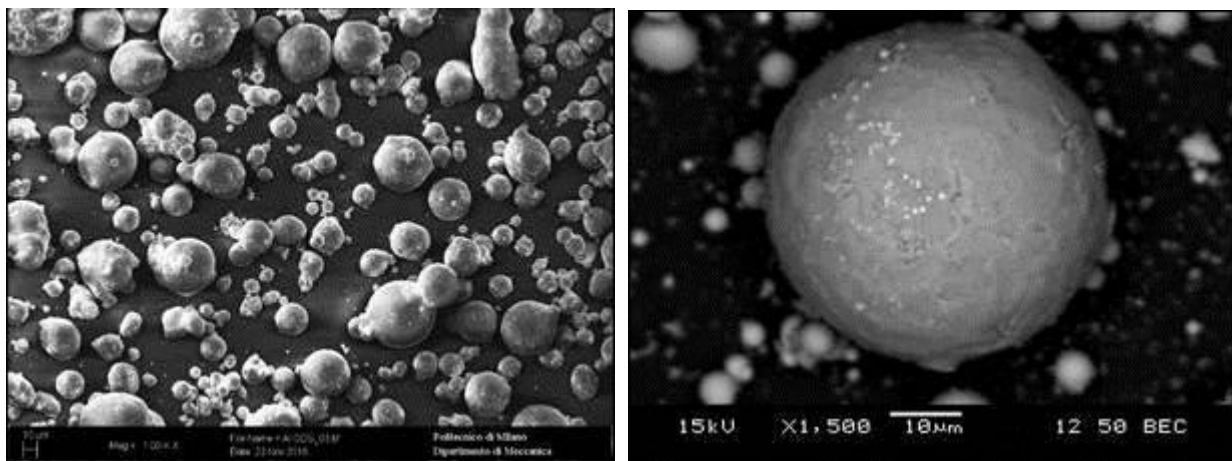


Figure B: Produced ODS powder

POLIMI selected the SLM (Selective Laser Melting) as additive manufacturing process. Hence, POLIMI produced samples for the assessment of mechanical and tribological behaviours (that have been accomplished by Rina CSM) Samples have been realised utilising both the master alloy powders (dispersoids-free AlSi7Mg) and the ODS powders (Figure C).

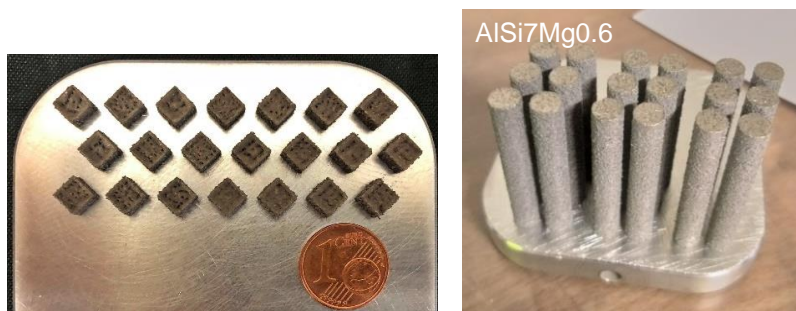


Figure C: Samples for mechanical (left) and tribological (right) tests

The results obtained show that, in general, the samples produced by AM process are mechanically and tribologically superior to those obtained by casting. The mechanical and tribological behaviour of ODS specimens and dispersoids - free specimens is comparable, no significant differences were measured in average coefficient of friction and wear rate values. Nevertheless, there is still a wide margin for improving the ODS powder characteristics and its processability by SLM.

In addition, POLIMI analysed systems for the laying of composite fibers. The first used production process, such as the hand lay-up, was manual and needed post-processing operations. Now, almost fully automated processes such as pultrusion, filament winding, automated tape laying (ATL) and automated fiber placement (AFP) are currently in use.

POLIMI contributed in the innovative production of composite material using a robotic system. The composite fibers have been produced and characterised (Figures D-E). This process enables the laying of the composite fibers according to the direction of stresses in the component as obtained from the structural analysis performed by BLUE. Mechanical properties were simulated and compared with required load cases.



Figure D: Examples of composite fibers

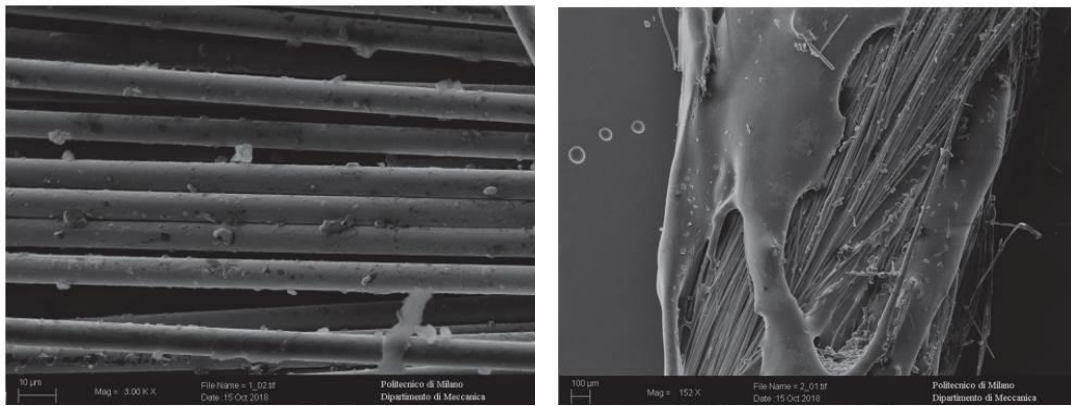


Figure E: NOT-consolidated (left) and consolidated (right) commingled yarn

In conclusion, both selected additive manufacturing processes (SLM and AFP) resulted very promising to produce lighter components for bogie frame with improved mechanical characteristics.



## ABBREVIATIONS AND ACRONYMS

$\alpha$	Activation energy
$\beta$	Angle of liquefier conical section
$\Delta P$	Pressure drop into the liquefier
$\Delta P_1$	Pressure drop in the zone I of liquefier
$\Delta P_2$	Pressure drop in the zone II of liquefier
$\Delta P_3$	Pressure drop in the zone III of liquefier
$\dot{\gamma}$	Shear rate
$\dot{m}$	Mass flow rate
$\eta$	Viscosity
$\eta T_0$	Viscosity at reference temperature
$\nu$	Poisson modulus
$\nu_f$	Fiber Poisson Modulus
$\nu_m$	Matrix Poisson modulus
$\nu_{12}$	Composite Poisson modulus
$\omega_r$	Rotational speed of the roller feeding system
$\rho$	Generic material density
$\rho_c$	Composite density
$d_f$	Filament diameter
$DAU_0$	Degree of bond at the initial time
$DAU$	Degree of bond
$DIC$	Degree of intimate contact
$E$	Elastic modulus
$\rho_f$	Fiber density
$\rho_m$	Matrix density
$\sigma$	Mechanical strength
$\sigma_\infty$	Cohesion strength
$\sigma_c$	Composite tensile strength along fiber direction
$\sigma_f$	Fiber tensile strength
$\sigma_m$	Matrix tensile strength
$\sigma_\vartheta$	Hoop stress of vessel
$\sigma_{ad}$	Adhesion strength
$\sigma_a$	Axial stress of vessel
$\tau_{cmax}$	Shear stress developed with the filament cutting system
$A_f$	Filament cross section
$C_m$	Feeding system motor torque
$c_p$	Specific heat capacity
$D$	Diameter of vessel
$D_1$	Diameter of the zone I of liquefier
$D_3$	Diameter of the zone III of liquefier
$E_f$	Fiber elastic modulus
$E_m$	Matrix elastic modulus
$E_{11}$	Composite longitudinal elastic modulus



$E_{22}$	Composite transversal elastic modulus
$F$	Force acting in longitudinal direction on the filament during the extrusion
$F_l$	Load of compaction system
$F_p$	Preload of compaction system
$F_s$	Force due to spring compression
$F_x$	Compaction system load component parallel to the deposition direction
$F_y$	Compaction system load component perpendicular to the deposition direction
$G$	Shear modulus
$H(T)$	Temperature-viscosity dependence coefficient
$I$	Current of the load
$I_{TripMAX}$	Maximum current provided by the stepper motor driver
$K$	Power law fitting coefficient
$k_s$	Spring elastic constant
$l$	Generic filament length
$L_1$	Length of the zone I of liquefier
$L_3$	Length of the zone III of liquefier
$L_f$	Length of filament from the feeding rollers to the liquefier entrance
$n$	Power law fitting coefficient
$P$	Internal pressure of vessel
$P_D$	Mosfet dissipation capability
$P_m$	Power supplied by the feeding system motor
$P_{app}$	Applied pressure during the contact of material interfaces
$P_{cr}$	Buckling critical pressure
$P_{MOSFET}$	Mosfet power due to load connection
$Q$	Composite volumetric flow rate in the nozzle
$R_r$	Radius of the feeding system
$R_s$	Stepper motor driver internal resistance
$R_{DS(on)}$	Mosfet Drain-Source On-State Resistance
$R_{thJA}$	Maximum Junction-to-Ambient coefficient
$s$	Thickness of vessel
$T$	Generic temperature value
$T_0$	Reference temperature value
$t_c$	Contact time
$T_i$	Temperature at the liquefier inlet
$T_m$	Temperature at which there is a complete diffusion into the polymer
$T_{amb}$	Ambient temperature
$T_J$	Maximum operating Junction Temperature
$V$	Composite volume (fibers and resin)
$v$	Filament extrusion velocity
$V_f$	Fiber volume
$v_f$	Fiber volume fraction
$v_m$	Matrix volume fraction
$V_{GS(th)}$	Mosfet Gate-Source Threshold Voltage



$V_{ref}$	Reference voltage of stepper motor driver
$w_f$	Fiber weight
$w_m$	Matrix weight
ODS	Oxide Dispersion Strengthened
SLM	Selective Laser Melting
VIM	Vacuum Induction Melting
VIGA	Vacuum Inert Gas Atomization



## TABLE OF CONTENTS

<b>REPORT CONTRIBUTORS.....</b>	<b>2</b>
<b>EXECUTIVE SUMMARY.....</b>	<b>3</b>
<b>ABBREVIATIONS AND ACRONYMS.....</b>	<b>7</b>
<b>TABLE OF CONTENTS.....</b>	<b>10</b>
<b>LIST OF FIGURES.....</b>	<b>12</b>
<b>LIST OF TABLES.....</b>	<b>17</b>
<b>SCOPE AND OBJECTIVES.....</b>	<b>18</b>
<b>1. BOGIE FRAME CONCEPT STUDY.....</b>	<b>19</b>
COMPONENTS SELECTION FOR NEW MANUFACTURING SOLUTIONS.....	22
SLM MODELLING.....	26
AXELBOX.....	27
LINK.....	30
<b>2. ADDITIVE MANUFACTURING.....</b>	<b>34</b>
METAL POWDER.....	36
STATE OF THE ART: OXIDE DISPERSION STRENGTHENED POWDER.....	39
ALSi10MG + 5%WT TiC.....	39
PURE AL + AL <sub>2</sub> O <sub>3</sub> .....	40
PURE AL + AL <sub>2</sub> O <sub>3</sub> .....	41
COMPOSITE FIBRES.....	42
STATE OF THE ART: COMPOSITE FIBERS.....	50
GLASS FIBERS.....	52
CARBON FIBERS.....	52
ARAMID FIBERS.....	53
NATURAL FIBERS.....	53
STATE OF THE ART: RESINS.....	53
THERMOSETTING RESINS.....	54
THERMOPLASTIC RESINS.....	55
<b>3. MANUFACTURING TECHNOLOGIES.....</b>	<b>57</b>
ADDITIVE MANUFACTURING TECHNOLOGIES.....	57
BINDER JETTING.....	58
DIRECTED ENERGY DEPOSITION.....	58
MATERIAL EXTRUSION.....	60
MATERIAL JETTING.....	61
POWDER BED FUSION.....	61
SHEET LAMINATION.....	62
VAT PHOTOPOLYMERIZATION.....	63
SYSTEM FOR THE LAYING OF COMPOSITE FIBRES.....	64



HAND LAY-UP .....	65
PULTRUSION .....	65
FILAMENT WINDING .....	66
AUTOMATED TAPE LAYERING .....	67
AUTOMATED FIBER PLACEMENT .....	70
<b><u>4. POWDER MANUFACTURING .....</u></b>	<b><u>72</u></b>
<b>VACUUM INDUCTION MELTING PROCESS.....</b>	<b>72</b>
<b>GAS ATOMIZATION PROCESS.....</b>	<b>74</b>
<b>POWDER CHARACTERIZATION.....</b>	<b>77</b>
<b>ODS POWDERS - DESIGN OF EXPERIMENT .....</b>	<b>79</b>
BALL MILLING PARAMETERS.....	79
MIXING POWDER.....	80
<b><u>5. SELECTIVE LASER MELTING SAMPLES PRODUCTION.....</u></b>	<b><u>85</u></b>
SLM SYSTEM.....	85
REDUCED BUILD VOLUME SYSTEM.....	86
PROCESS PARAMETERS INVOLVED IN SLM .....	87
MITUTOYO QUICK-VISION ACTIVE 202-PRO5F MICROSCOPE.....	88
EXPERIMENTAL DESIGN .....	89
MECHANICAL CHARACTERIZATION .....	92
TRIBOLOGICAL CHARACTERIZATION .....	98
<b><u>6. FDM AND ADHESION MODEL.....</u></b>	<b><u>105</u></b>
<b>EXTRUSION MECHANISM .....</b>	<b>105</b>
<b>CONTACT AND ADHESION MODEL.....</b>	<b>109</b>
<b>HEAD .....</b>	<b>112</b>
EXISTING PRINTING HEAD .....	113
MODIFIED PRINTING HEAD.....	117
<b>ROBOT SETUP.....</b>	<b>123</b>
ELECTRO-MECHANICAL SETUP.....	123
ROBOT TRAJECTORIES .....	127
<b>COMPARISON OF CCF FILAMENTS AND SAMPLE TESTS .....</b>	<b>129</b>
FILAMENT TESTS .....	132
SAMPLE TESTS .....	137
<b><u>7. CONCLUSIONS AND FUTURE WORK.....</u></b>	<b><u>144</u></b>
<b><u>REFERENCES .....</u></b>	<b><u>148</u></b>



## LIST OF FIGURES

Figure 1: Bogie frame: new architecture and main data.....	19
Figure 2: Bogie frame components.....	20
Figure 3: Single axle running gear: new architecture and main data.....	20
Figure 4: Single axle running gear components.....	21
Figure 5: Axlebox .....	23
Figure 6: Link .....	23
Figure 7: Renishaw AM 400 .....	24
Figure 8: Calibration process.....	25
Figure 9: Specimes for calibration .....	25
Figure 10: Displacement evaluation along Z.....	25
Figure 11: Support design .....	27
Figure 12: Support optimization.....	27
Figure 13: Distortion Compensation .....	28
Figure 14: Total displacement .....	28
Figure 15: Surface deviation.....	28
Figure 16: Total displacement .....	29
Figure 17: Surface deviation.....	29
Figure 18: Total displacement .....	29
Figure 19: Surface deviation.....	29
Figure 20: A piece of axlebox .....	30
Figure 21: Support design: Link.....	30
Figure 22: Support Optimization.....	31
Figure 23: Number of runs performed during the optimization phase.....	32
Figure 24: Total displacement .....	32
Figure 25: Surface deviation.....	32
Figure 26: Total displacement .....	33
Figure 27: Surface-deviation .....	33
Figure 28: Total Aluminum AM Powder Revenues by Applicant Segment \$ millions US 2017 - 2028 [1] .....	35
Figure 29: Impact of metal powder properties [2].....	37
Figure 30: Powder morphology due to different production process .....	38
Figure 31: AlSi10Mg + 5%wt TiC [5].....	40



Figure 32: The morphology of Al powder after milling for a) 0h b) 4h c) 8h d) 12h e) 16h f) 20h [6] ..... 41

Figure 33: SEM images showing the morphology of ball-milled composite [6] ..... 41

Figure 34: Pure Al + Al<sub>2</sub>O<sub>3</sub> results [7] ..... 42

Figure 35: Strain-stress matrix ..... 43

Figure 36: Planes of symmetry in an orthotropic material [8] ..... 44

Figure 37: Difference in deformations of isotropic (a), orthotropic (b) and anisotropic (c) materials subjected to uniaxial tension and pure shear stresses (b) and anisotropic (c) materials subjected to uniaxial tension and pure shear stresses [8] ..... 44

Figure 38: Angle-ply laminate [8] ..... 45

Figure 39: Prepreg carbon reinforced sheet for had lay-up process ..... 46

Figure 40: Manufacturing process of commingled carbon-PPS yarn [11] ..... 47

Figure 41: Commingled yarn cross section during consolidation process [12] ..... 47

Figure 42: Mechanical properties of a composite [11] ..... 48

Figure 43: Longitudinal and transversal elastic modulus ..... 48

Figure 44: Composite moduli along orthogonal directions as function of the reinforcing fiber volume fraction ..... 49

Figure 45: Effect of carbon fiber content on the unnotched Charpy impact test of 0° carbon-E-glass epoxy interply hybrid laminates ..... 49

Figure 46: Young modulus and shear modulus oblique to the fibre direction in a glass-epoxy lamina with  $\nu_f = 0.5$  ..... 50

Figure 47: Tensile stress-strain diagrams for various reinforcing fibers [8] ..... 51

Figure 48: Properties of the main commercial reinforcing fibers [8] ..... 51

Figure 49: Typical composition of glass fibers (in weight %) [8] ..... 52

Figure 50: Arrangement of carbon atoms in a graphite crystal [8] ..... 53

Figure 51: Difference between thermoplastic (a) and thermosetting (b) resins [8] ..... 54

Figure 52: Melting temperature and heat capacity of crystalline (a) and amorphous (b) solids ... 56

Figure 53: Elastic modulus of amorphous solid as function of temperature ..... 56

Figure 54: Binder jetting process [14] ..... 58

Figure 55: Directed Energy Deposition process [15] ..... 59

Figure 56: Material Extrusion process [15] ..... 60

Figure 57: Material Jetting process [15] ..... 61

Figure 58: Powder Bed Fusion [16] ..... 61

Figure 59: Sheet Lamination process [15] ..... 63

Figure 60: Vat Photopolymerization process [15] ..... 64

Figure 61: Pultrusion process [8] ..... 66



Figure 62: Filament winding process [19] .....	67
Figure 63: Cross section of possible filament-wound parts (a and b), example of a cross section that cannot be filament-wound (c) [19].....	67
Figure 64: ATL printing head [21] .....	68
Figure 65: Laps and gaps during ATL process [20] .....	69
Figure 66: Tow steering defects [20].....	69
Figure 67: ATL deposition and motion systems [22] .....	70
Figure 68: AFP printing head [24].....	71
Figure 69: Robot manipulator used for motion during an AFP process [24] .....	71
Figure 70: Steps of VIM process .....	73
Figure 71: Representative gas-atomization configurations [4]:.....	74
Figure 72: RINA CSM's VIGA plant .....	76
Figure 73: Induction furnace of RINA CSM's VIGA.....	77
Figure 74: Atomization phase .....	77
Figure 75: Particle Size Distribution.....	78
Figure 76: SEM images .....	78
Figure 77: Alumina sphere .....	79
Figure 78: RINA CSM Miller .....	80
Figure 79. The powder used in the experiment are observed with SEM .....	85
Figure 80 : Reinshaw AM250 SLM Machine.....	86
Figure 81 :RBV parts details and SLM of samples on RBV platform.....	87
Figure 82: Process parameters involved in SLM.....	88
Figure 83: Mitutoyo Quick-Vision Active 202-Pro5f Microscope.....	88
Figure 84: Examples of porosity as contrasting colour ranges in the indicated area, the porosity is then measured using the software as ratio to the indicated area .....	89
Figure 85: Macro images of the samples after SLM and after polishing.....	89
Figure 86 : Main effects and interaction plots for part density .....	90
Figure 87 : Normal plot of the standardized effects.....	90
Figure 88 :Part density as a function of energy density.....	90
Figure 89: Production of pins for tribological tests .....	91
Figure 90: A357 S1 Mass lost after PoD test.....	100
Figure 91: A357 S1 Pin shortening after PoD test .....	100
Figure 92: Average Coefficient of Friction measured during PoD test.....	101
Figure 93: ODS S1 Mass lost after PoD test.....	101
Figure 94: Pin shortening after PoD test.....	102



Figure 95: Average Coefficient of Friction measured during PoD test..... 102

Figure 96: CoF results from M. Lorusso [26]..... 104

Figure 97: Buckling of a filament between the feeding rollers and the liquefier inlet [23]..... 107

Figure 98: Model of liquefier ..... 109

Figure 99: Illustration of the adhesion phenomenon [27] ..... 110

Figure 100: Compaction evolution as a function of time and temperature [27]..... 111

Figure 101: Representation of surface models [28] ..... 112

Figure 102: Printing head and compression system of the first prototype ..... 114

Figure 103: Schematic representation of the first compaction system [29]..... 115

Figure 104: Schematic representation of the filament cutting system [29] ..... 115

Figure 105: Schematic representation of the hot chamber block ..... 117

Figure 106: Schematic representation of the modified compaction system..... 118

Figure 107: New printing head during the print of a carbon-PA6 sample ..... 118

Figure 108: Samples printed on the TAZ with the Markforged filament and the new printing head  
..... 119

Figure 109: Graphical results of the sample tensile test..... 121

Figure 110: Tensile test results of Young modulus (a) and UTS (b)..... 121

Figure 111: Load cell measurements: load time history (a) and FFT signal analysis (b) ..... 122

Figure 112: Robot-extruder connecting system ..... 123

Figure 113: Scheme of the printing head circuit..... 125

Figure 114: Final robot setup..... 128

Figure 115: Grasshopper script for sample trajectory definition ..... 128

Figure 116: Example of trajectory of crossed-layer composite 3D print sample ..... 129

Figure 117: Example of trajectory of simple composite 3D print sample ..... 129

Figure 118: Not-consolidated commingled yarn..... 131

Figure 119: Not-consolidated commingled yarn - SEM 500X..... 131

Figure 120: NOT-consolidated commingled yarn - SEM 3.00K X ..... 132

Figure 121: Manual consolidation of commingled yarn ..... 132

Figure 122: Consolidated commingled yarn - SEM 152X..... 133

Figure 123: Consolidated commingled yarn - SEM 1.43K X ..... 134

Figure 124: Tensile test comparison between consolidated and not-consolidated filament (PA6  
12k AS4A) ..... 134

Figure 125: Tensile test comparison between consolidated and not-consolidated filament (PA12  
12k AS4A) ..... 135



Figure 126: Tensile test comparison between consolidated and not-consolidated filament (PA6 3k AS4C)..... 135

Figure 127: PA12 12k AS4A filament printing test ..... 136

Figure 128: Tensile test of a single PA12 12k AS4A filament 3D printed ..... 137

Figure 129: Head setup for sample printing ..... 138

Figure 130: Samples of PA6 12k AS4A and PA12 12k AS4A..... 139

Figure 131: Spring preload: 10N (a), 20N (b), 30N (c) ..... 140

Figure 132: Compaction force components ..... 141

Figure 133: Load cell acquisitions during printing with different sping preload: 10N (a), 20N (b), 30N (c)..... 141

Figure 134: Force between roller and filament at compression start:  $F_l$  is the overall force exerted by the compaction roller,  $F_x$  is the component parallel to the extrusion direction and  $F_y$  is the component in vertical direction ..... 142

Figure 135: Tensile test of 12k AS4A PA6 samples (a) and Tensile test of 12k AS4A PA12 samples (b)..... 143

Figure 136: PA12 12k AS4A: tensile test results of Young modulus (a) and UTS (b)..... 143

Figure 137: Commercial SLM machine dimensions and build envelope geometries. Data provided by system manufacturers' websites. .... 145

Figure 138: Aerosud – South Africa 2000 x 500 mm<sup>3</sup> ..... 146

Figure 139: Adira - 1000 x 1000 x 500 mm<sup>3</sup>..... 146

Figure 140: GE Atlas -1000 x 1000 x 1000 mm<sup>3</sup> ..... 147



## LIST OF TABLES

Table 1: Bogie frame components: material, weight and manufacturing process.....	21
Table 2: Single axle running gear components: material, weight and manufacturing process.....	22
Table 3: Materials processed by AM [4].....	38
Table 4: AlSi10Mg + 5%wt TiC [5].....	39
Table 5: Pure Al + Al <sub>2</sub> O <sub>3</sub> [6].....	40
Table 6: Pure Al + Al <sub>2</sub> O <sub>3</sub> [7].....	41
Table 7: Chemical results.....	74
Table 8: Variables in gas atomization.....	75
Table 9: Process parameters.....	77
Table 10: Powder characterization results.....	77
Table 11: Ball Milling Process Parameters.....	79
Table 12. RBV platform dimensions.....	86
Table 13: Process parameters used to produce pins.....	91
Table 14: Pin-On-Disk Parameters.....	99
Table 15: A357 S1 Density.....	99
Table 16: ODS S1 Density.....	99
Table 17: A357 S1 PoD test results.....	99
Table 18: ODS S1 PoD test results.....	101
Table 19: Average wear loss and CoF.....	103
Table 20: Wear loss comparison with S. Khan [25].....	103
Table 21: Wear loss comparison with M. Lorusso [26].....	103
Table 22: Markforged filament properties [30].....	113
Table 23: Tensile test first samples.....	120
Table 24: Natural frequencies of extruder moving parts.....	122
Table 25: IRLZ44N n-channel MOSFET properties.....	126
Table 26: Heated bed and hot chamber properties.....	126
Table 27: Results of filaments tensile test.....	136
Table 28: Tensile test results of PA6 12k AS4A specimens.....	139
Table 29: Tensile test results of PA12 12k AS4A specimens.....	139
Table 30: Maximum achieved strength-to-weight ratio for PA6 12k AS4A and PA12 12k AS4A specimens.....	143
Table 31: Axlebox material [35].....	144



## **SCOPE AND OBJECTIVES**

---

The RUN2RAIL project explores an ensemble of technical developments for future running gear, looking into ways to design trains that are more reliable, lighter, less damaging to the track, more comfortable and less noisy. In this contest, one of the main thematic work stream is the “Optimised materials & manufacturing technologies” one.

This report is focused on the use of novel materials and manufacturing methods in combination with intelligent / active suspensions to enable nonconventional running gear concepts.

In particular:

- BLUE performed a concept design concerning a bogie frame and a single axle gear. Virtual modelling and simulated manufacturing of some components were performed, considering the candidate materials and process solutions. Selected components were Axlebox and Link because they can be realised in innovative composite material respecting actual manufacturing requirements,
- Rina CSM focused attention on manufacturing innovative metal powder through VIGA (Vacuum Inert Gas Atomization). A new aluminium alloy, reinforced by alumina disperosoids to improve mechanical properties for the final application, has been produced. Utilising the new metal powder, POLIMI prepared specimens with SLM (Selective-Laser-Melting) process. These specimens were mechanically and tribologically characterised by Rina.
- POLIMI contributed in the novel production of the bogie frame composite material, using a robotic system for the laying of composite fibres. This process enables the laying of the composite fibres according to the direction of stresses in the component as obtained from the structural analysis performed by BLUE. Mechanical properties were simulated and compared with required load cases.



## 1. BOGIE FRAME CONCEPT STUDY

During the first phase of the project, a new architecture has been designed for:

- a bogie frame (Figures 1-2) and
- a single axle running gear (Figure 3-4).

Moreover, the adoption of new materials for some of their components has been assessed in order to produce them more reliable, lighter, less damaging to the track, more comfortable and less noisy. Tables 1-2 summarizes selected material, weight and manufacturing process for each component.

Main data	
Length	3470 mm
Width	2520 mm
Height	970 mm
Weight assessment	~ 5000 kg

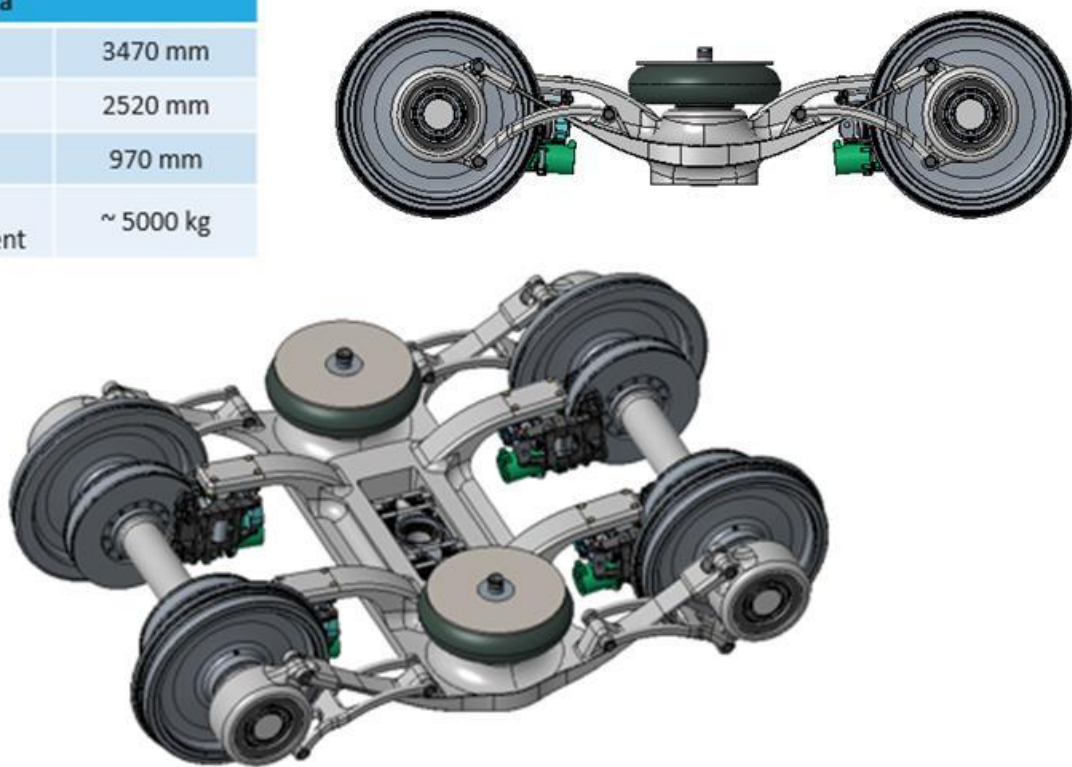


**Figure 1: Bogie frame: new architecture and main data**

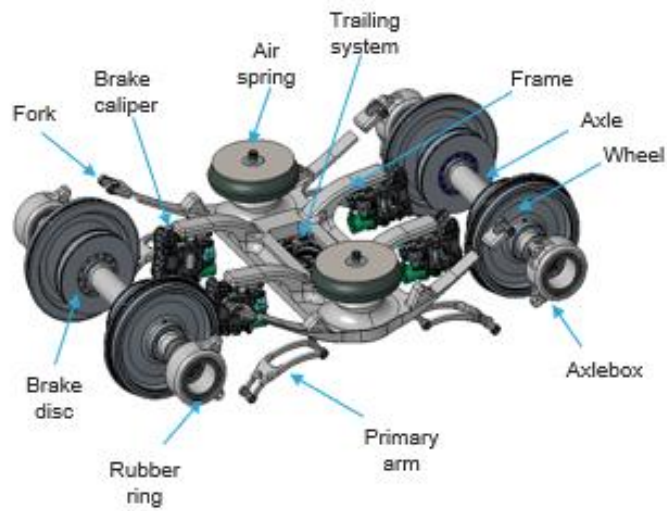


Figure 2: Bogie frame components

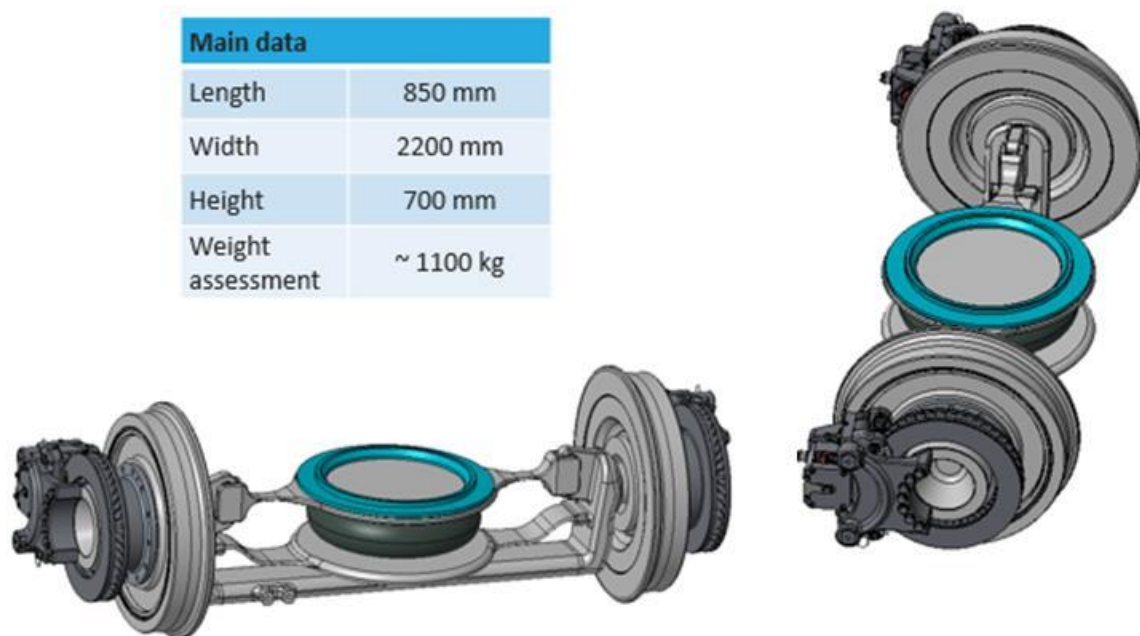


Figure 3: Single axle running gear: new architecture and main data

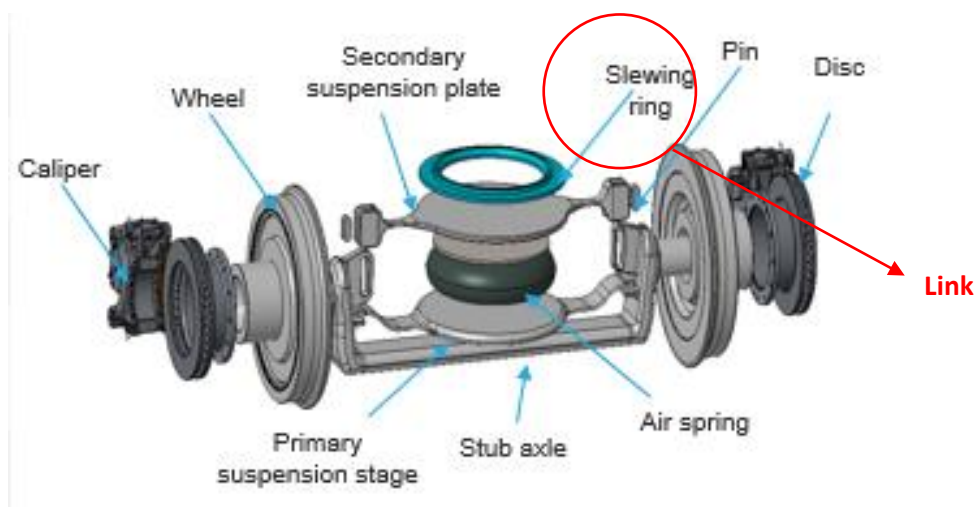


Figure 4: Single axle running gear components

Table 1: Bogie frame components: material, weight and manufacturing process

	Material	Weight [kg]	Manufacturing process
Wheel	Steel	350	Forging
Brake caliper	Steel/Aluminum/Titanium alloy	80	Additive manufacturing
Brake disc	Steel	130	Forging
Trailing system	Steel/rubber	150	Forging
Axle	Carbon fiber + Steel (interfaces)	120	Forging + filament winding
Frame	Carbon fiber + Steel (interfaces)	800	Closed molding + Additive manufacturing
Primary suspension stage	Steel/titanium alloy + rubber	200	Additive manufacturing
Secondary suspension plate	Carbon fiber + steel/titanium alloy (interfaces)	50	Closed molding + Additive manufacturing
Primary arm	Steel/Titanium alloy	35	Additive manufacturing
Fork	Steel/titanium alloy	5	Additive manufacturing

**Table 2: Single axle running gear components: material, weight and manufacturing process**

	Material	Weight [kg]	Manufacturing process
Wheel	Steel	220	Forging
Brake caliper	Steel/Aluminum/Titanium alloy	50	Additive manufacturing
Brake disc	Steel	50	Forging
Slewing ring	Steel	110	Forging
Stub Axle	Carbon fiber + Steel (interfaces)	100	Closed molding + additive manufacturing
Primary suspension stage	Carbon fiber + steel/titanium alloy	50	Closed molding + additive manufacturing
Secondary suspension plate	Carbon fiber + steel/titanium alloy (interfaces)	50	Closed molding + additive manufacturing
Pin	Steel/Titanium alloy	2	Additive manufacturing

Within the two configurations described above, two structural components have been identified: the axlebox for bogie and the link for the single axle running gear. These two components can be optimized to take advantages by additive manufacturing, such as:

- Very high design freedom
- Lightweight optimized structures
- Individualization
- Process efficiency.

## **COMPONENTS SELECTION FOR NEW MANUFACTURING SOLUTIONS**

Visual modelling and simulated manufacturing of selected components were carried out for the selected components:

- Axlebox,
- Link.

A lattice structure was chosen for the axlebox component. The dimension of the axle-box is larger than the printer plane, so a quarter of an axlebox was considered (Figure 5). The chosen material is AlSi10Mg powder, with a lattice structure that can reduce the weight by about 30%.

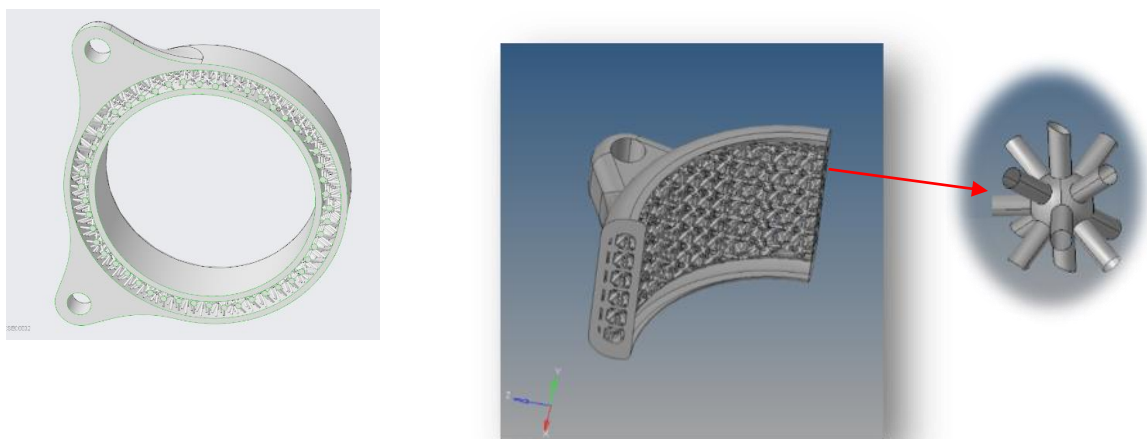


**Figure 5: Axlebox**

The link component was printed in the same material as the axle box. The link is divided into two parts and printed already assembled (Figure 6). This possibility allows a weight reduction in comparison with a traditional mechanical link (joints with bolts).

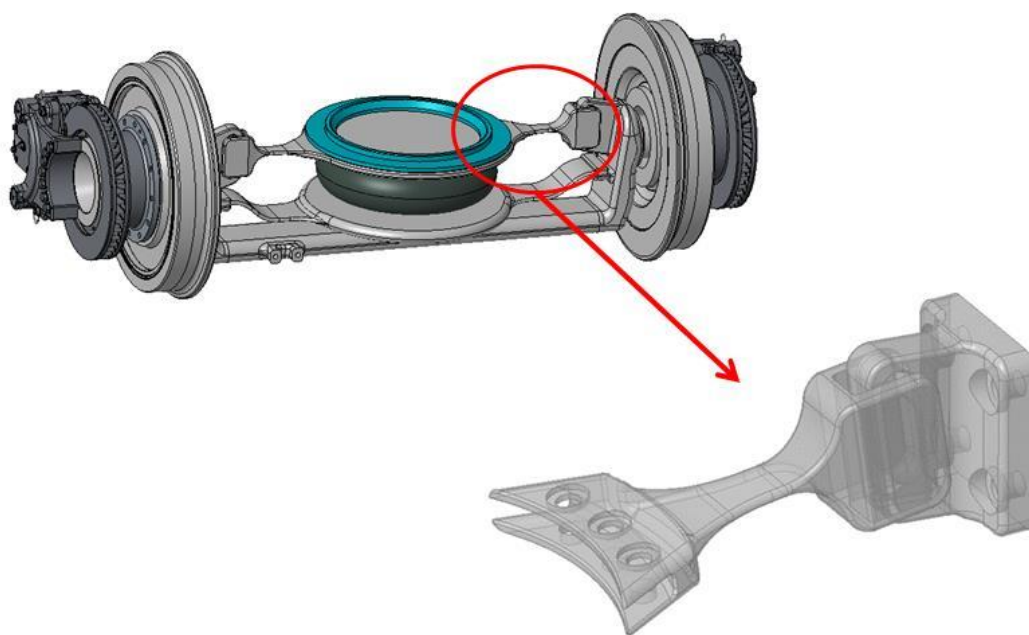


**Figure 6: Link**

The printer shown in Figure 7 uses SLM-Selective Laser Melting technology. Each printing machine needs to perform its own calibration. In this particular case, calibration was made on the Renishaw AM400.



**Figure 7: Renishaw AM 400**

Manufacturer	Renishaw
Model	AM400
Technology	SLS
Building volume [mm]	250x250x300

The calibration process is shown in Figure 8. The out-put of the calibration phase are inherent strains (dependent on the printing process). So, there is a need to print specimen and to analyse the mechanical parameters in order to better define the process parameters of the printing phase (reverse-engineering).



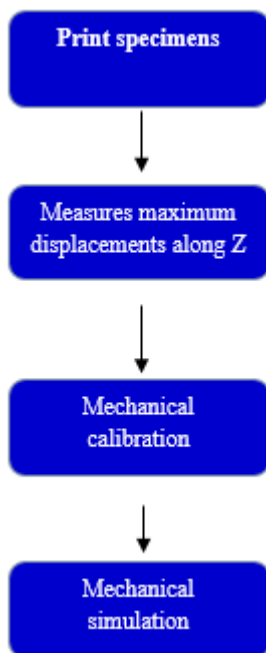


Figure 8: Calibration process

Print characteristics of specimen are: material, printing strategy, print parameters, direction of the specimens (0° and 90°).

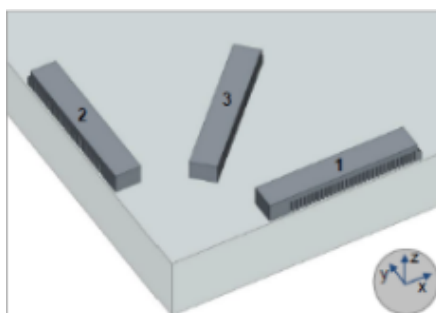


Figure 9: Specimens for calibration

Maximum displacement along Z of each single specimen was measured.

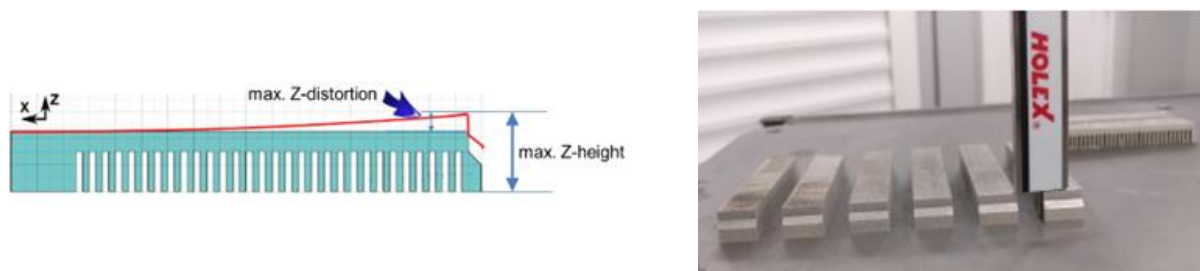


Figure 10: Displacement evaluation along Z

Simufact software starts a multi-step procedure, where it will generate in out-put the inherent-strains along x, y and z direction. Values obtained will be used in the simulation so as to have a precise compensation of the deformations that occur during the cutting phase.

In particular:

- Specimen 1: 3.09 [mm]
- Specimen 2: 2.01 [mm]

Software starts a multi-step procedure, where it generates in out-put the inherent strains along x, y and z direction.

$$\varepsilon_{xx} = -0.008$$

$$\varepsilon_{yy} = -0.008$$

$$\varepsilon_{zz} = -0.03$$

## SLM MODELLING

The following steps have been done for each component:

- *support design*: with the help of the orientation assistant tool, the component was optimally positioned on the printing,
- *support optimisation*: procedure characterized by a series of loops which defines the volume of supports according to the geometry of the component,
- *distortion compensation*: procedure characterized by a series of loops that defines the optimal position as a function of the component geometry, decreasing its deformations during the printing phase,
- *mechanical simulation*: total displacement and surface deviation simulations have been done for built, cutting and support removal phases.

In the following, the simulation results for both axelbox and link are reported.



## Axelbox

### Support design

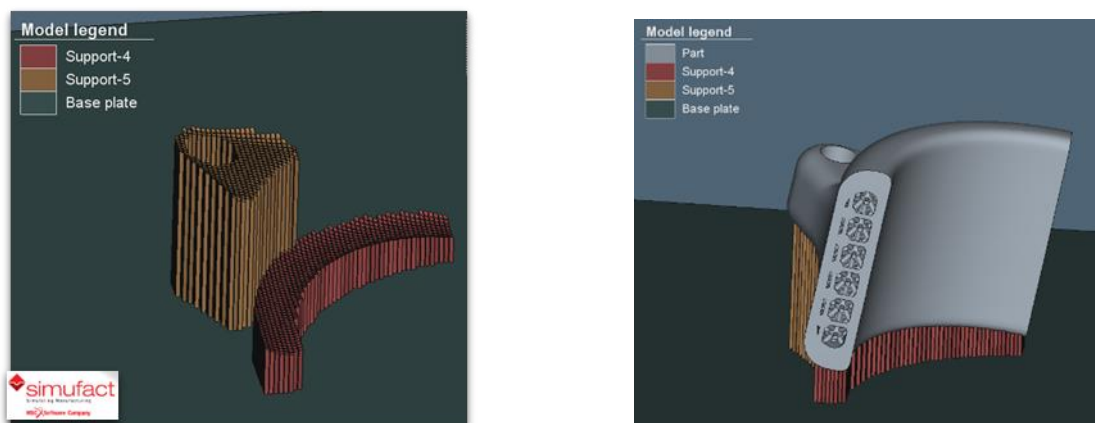


Figure 11: Support design

### Support Optimisation

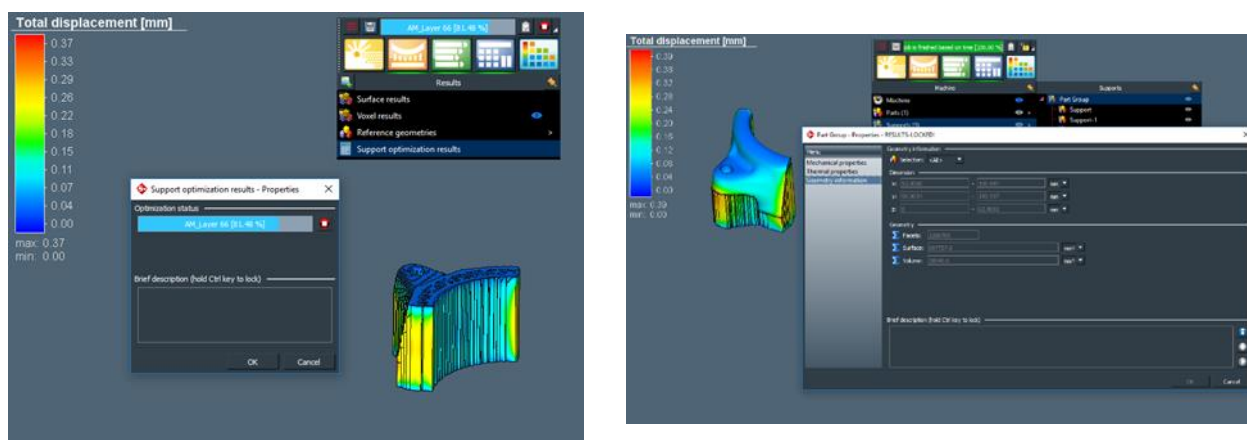


Figure 12: Support optimization

### Distortion compensation

A number of 20 runs has been carried out to obtain a deformation of less than 0.1 mm.

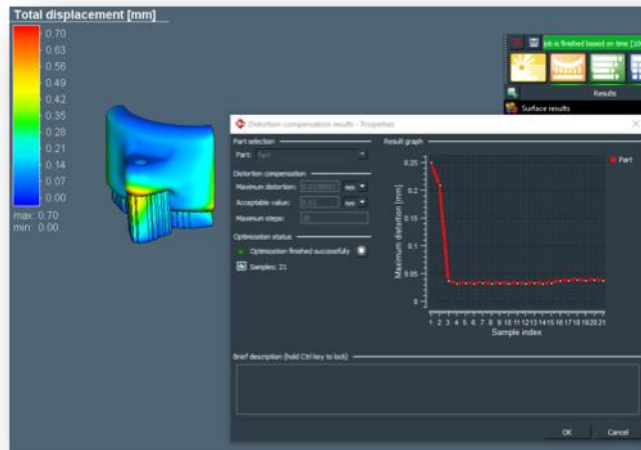


Figure 13: Distortion Compensation

Mechanical Simulation

*Build*

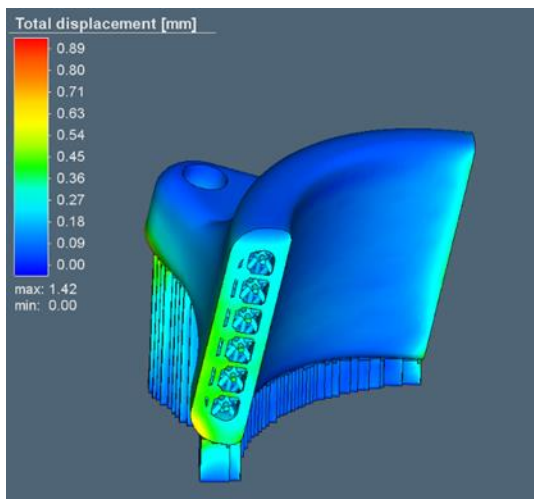


Figure 14: Total displacement

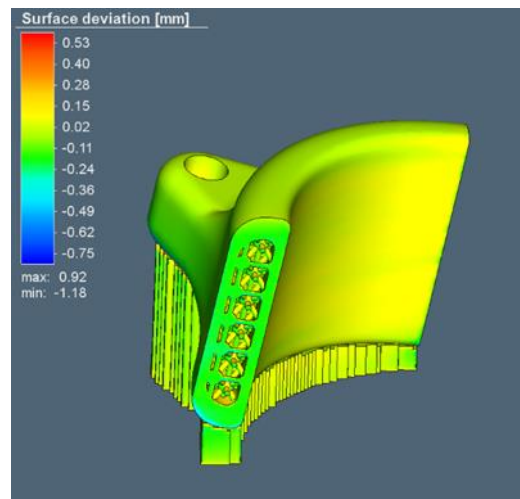


Figure 15: Surface deviation



Cutting

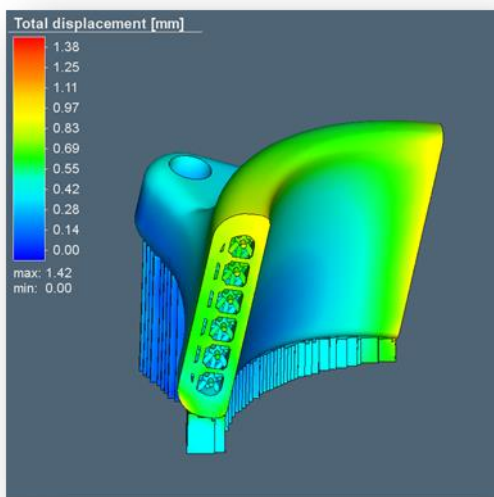


Figure 16: Total displacement

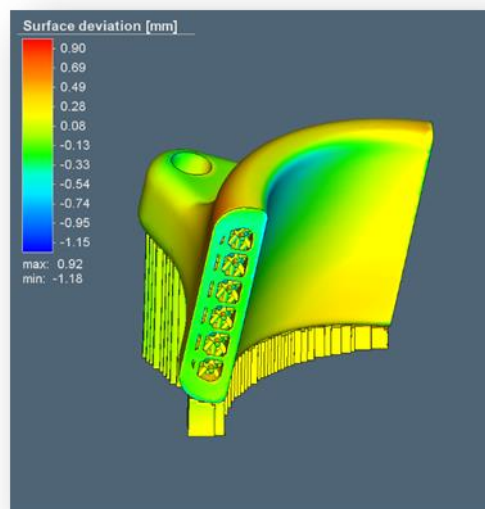


Figure 17: Surface deviation

Support removal

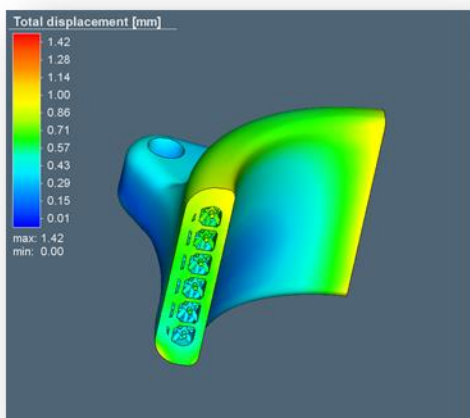


Figure 18: Total displacement

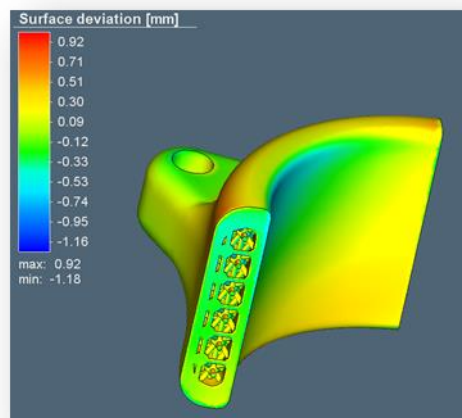


Figure 19: Surface deviation

SLM modelling of the axlebox has shown that:

- following the correct optimization procedure in the printing phase, not critical deformations or surface deviations are formed,
- the most critical part of the process is the cutting phase. However, there are only small surface deviations, that do not alter the final geometry of the component,
- it is necessary to design holes to free the parts occupied by the lattice cells that, after printing, are filled with aluminum powders.

Finally, BLUE realized a piece of axlebox by SLM process. The obtained prototype is shown in Figure 20.



Figure 20: A piece of axlebox

## Link

### Support design

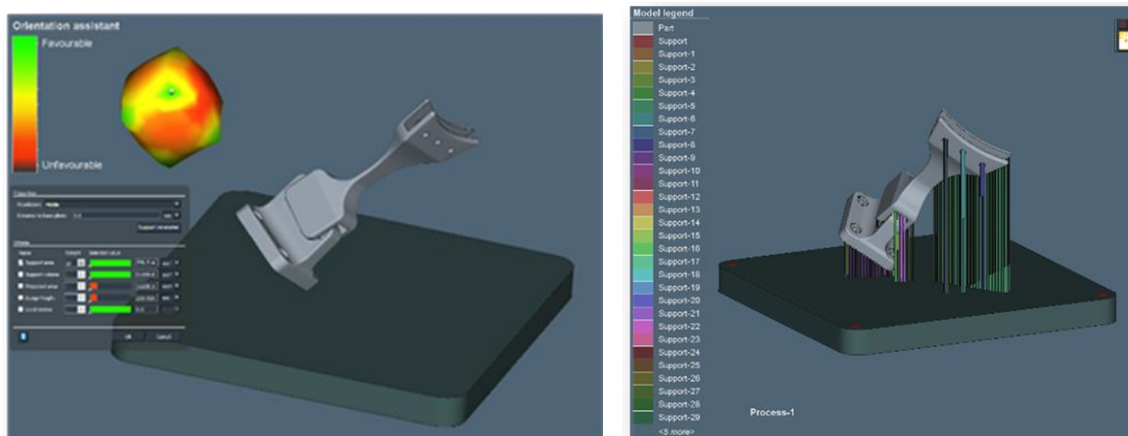


Figure 21: Support design: Link

Support Optimization

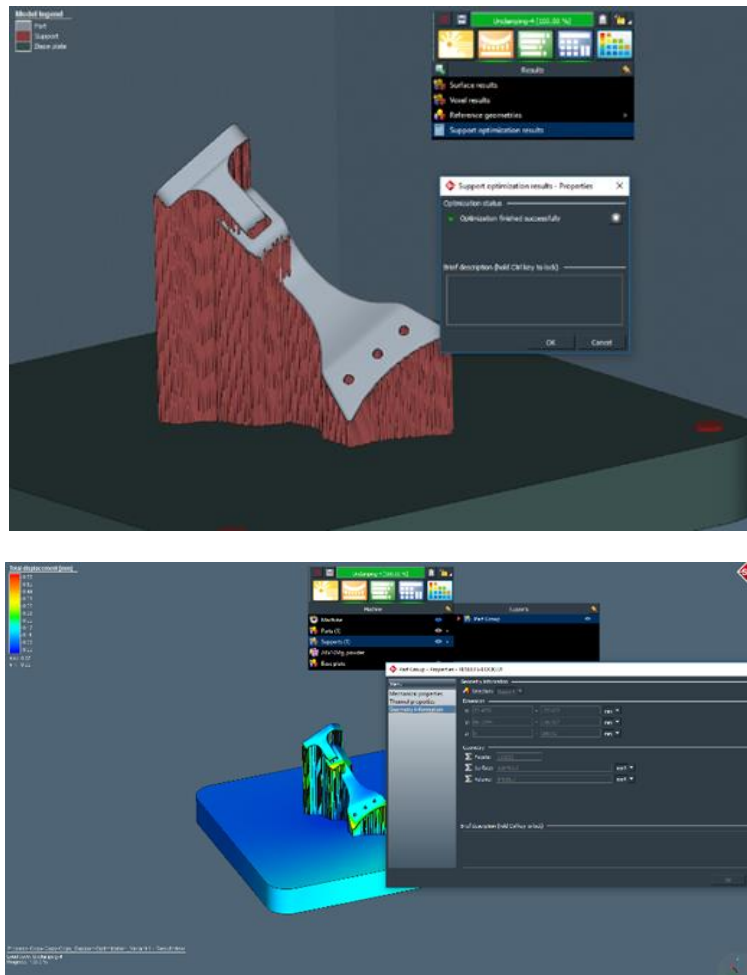
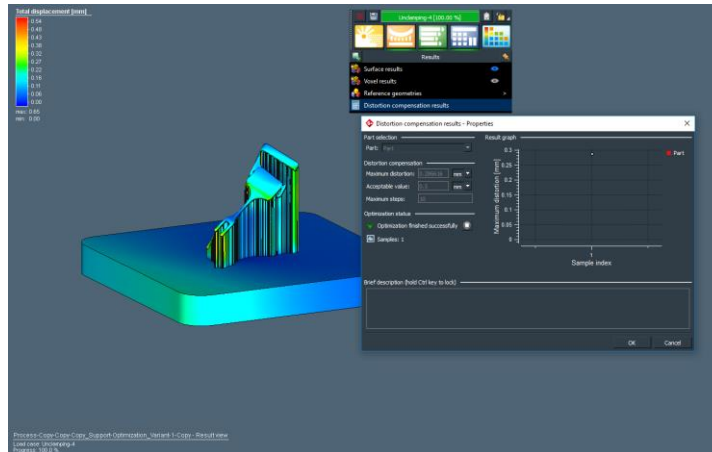


Figure 22: Support Optimization

Distortion compensation



**Figure 23: Number of runs performed during the optimization phase**

Also in this case, the idea was to perform a number of 10 runs to obtain a deformation of less than 0.5 mm. However, the desired maximum deformation value has been reached after one run.

Mechanical simulation

*Build*

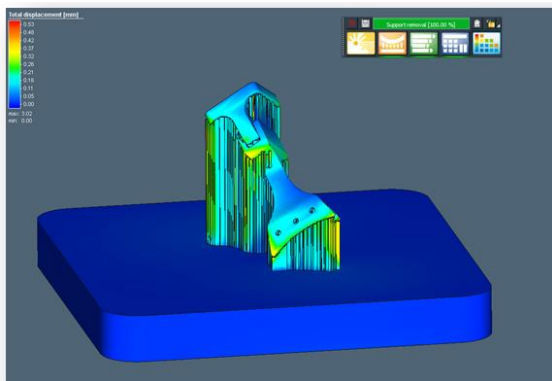


**Figure 24: Total displacement**

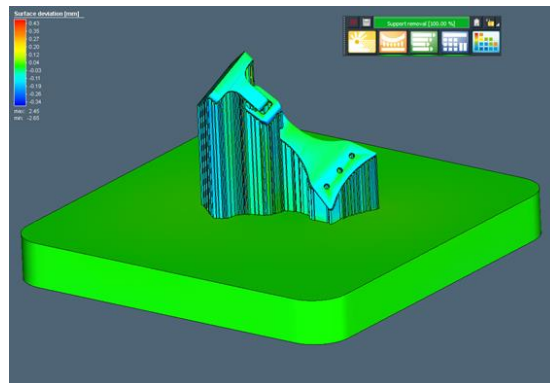


**Figure 25: Surface deviation**



*Cutting*

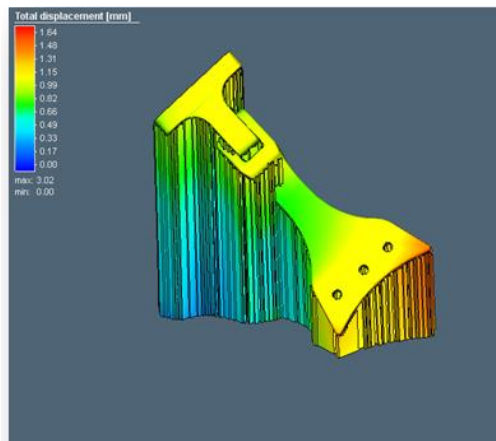


Figure 26: Total displacement

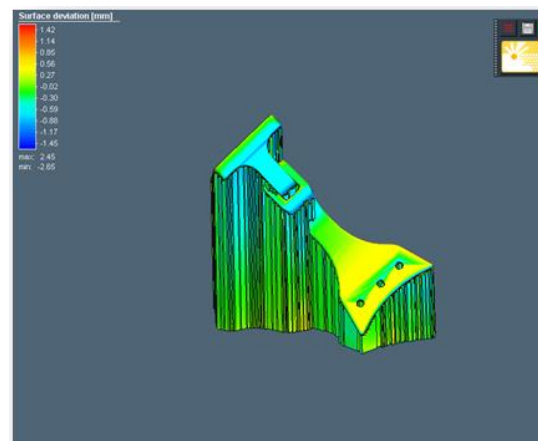


Figure 27: Surface-deviation

*Support-removal*

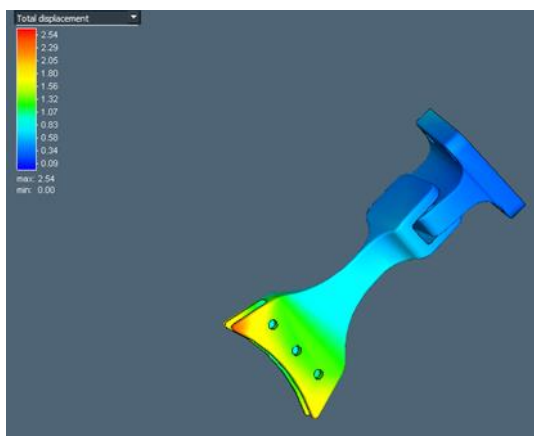


Figure 26a: Total displacement

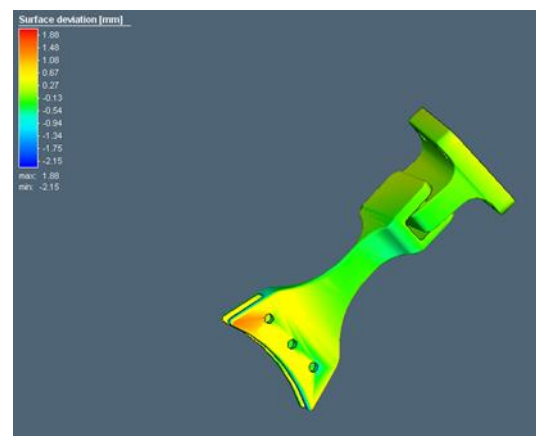


Figure 27a: Surface deviation

SLM modelling of the link has shown that:

- with the correct optimization procedure in the printing phase not critical deformations are formed,
- the cutting and support removal steps could be critical from the deformation point of view. It is possible to proceed with a further loop, modifying local geometry of the component.

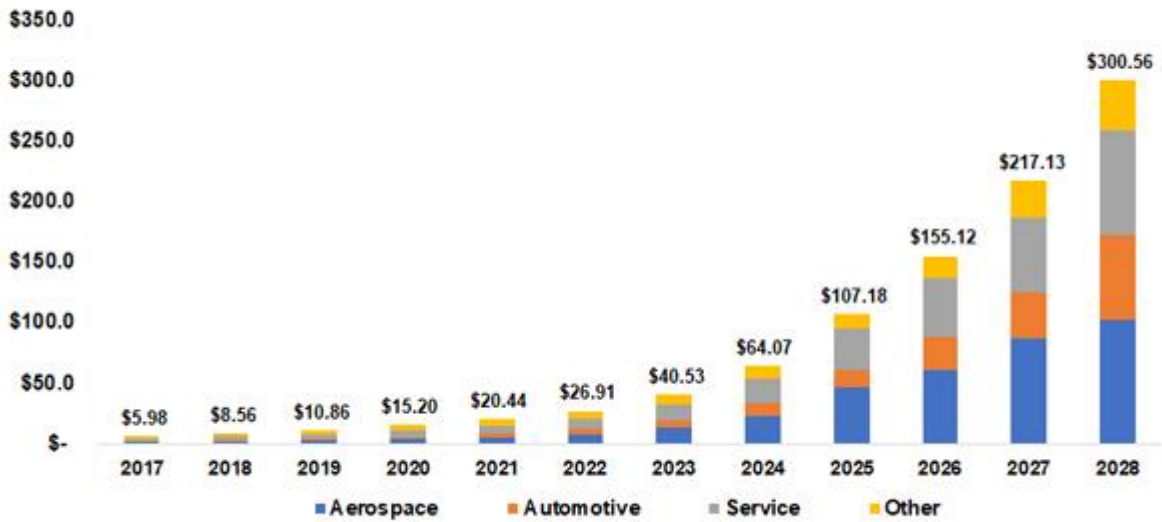


## **2. ADDITIVE MANUFACTURING**

Additive Manufacturing (AM) plays a pivotal role in changing the manufacturing paradigm and contributing to address the societal challenges of our time, such as global warming, energy transition, population ageing and decreasing resources. Metal Additive Manufacturing (MAM) shows great promise for optimized, customized and highly efficient products for several sectors. In 2017, the AM industry turnover, consisting of all AM products and services worldwide, grew 21% y/y to \$7.336 billion. It is expected to grow up to \$200 billions, where metals were the main drivers of the sector [1]. However, today MAM remains a niche technology with applications largely in the automotive, aerospace and medical sectors. A key limitation to the expansion of the MAM technologies is related to the scarcity of the material variety. The alloys processable by MAM technologies remain very limited. Al-alloys are well known to be difficult to be processed by lasers due to the high optical reflectivity, high affinity to oxygen and hydrogen, low melting and boiling points, as well as crack susceptibility. Such conditions limit the use of both MAM processes and Al-alloy in the industry. On the other hand, the demand for more efficient and lighter structures is continuously increasing, especially for the use of Al alloys. Aluminum is expected to be among the key materials in the shift towards larger batch production of mass goods. The market for aluminum alloys in AM is expected to become a major segment in metal 3D printing, with revenues topping \$300 million. The Al alloys suitable for MAM processes (mainly based on Al-Si systems), have limited mechanical resistance, lower than those obtained for conventional Al 7000 Series alloys. Therefore, options within these materials are usually limited to applications of models for form/fit testing, functional testing, presentation models, prototypes and non-load bearing products. To answer the market demand, the development of new Al based alloys with improved properties, constitutes a key factor both in terms of process and product performance. From this point of view, nanomaterials may provide the leap of quality required for a wider use of AM Al-alloys. Metal Matrix Nano Composites (MMNCs) exhibit outstanding properties overcoming MMCs, especially on ductility, fracture toughness and machinability. The use of nano-sized reinforcements can provide superior properties compared to the more conventionally used micrometric reinforcements. The incorporation of nanosized ceramic reinforcements less than 1% weight can lead to a much greater increase in the strength of conventional Al-based composites. Such potential improvements have great implications for instance for the automotive, aerospace and defense industry due to drastic weight savings and better tailored properties.



**Total Aluminum AM Powder Revenues by Application Segment  
\$ millions US 2017 - 2028**



Source: Smartertech Publishing 2018

**Figure 28: Total Aluminum AM Powder Revenues by Applicant Segment \$ millions US 2017 -2028 [1]**

The greatest challenge facing the development of MMNCs for wide application, using current methods, is the complexity of synthesis and processing nanocomposites. As for MMC, the mechanical properties of MMNC are strongly dependent on type, distribution and volume fraction of the reinforcement, as well as on interfacial energy between the particle and the matrix. Due to the high surface area, nano-sized powders will naturally tend to agglomerate to reduce their overall surface energy, making it difficult to obtain a uniform dispersion by most conventional processing methods. In addition, due to their high surface area, these materials may also be highly reactive in metal matrices. To overcome these concerns, processing methods are being developed to produce MMNCs with uniform dispersion of nanomaterials and reduced deleterious interfacial reaction. A variety of processes has been explored and studied over the years, including powder metallurgy, deformation, vapor phase and solidification. However, none of them resulted as the optimum-processing route, being expensive and difficult to scale up, to manufacture in bulk large and complex shapes. The extremely high solidification and cooling rates associated to laser-based AM technologies open the possibility to prevent nanometric particles from coarsening after their precipitation. Therefore, it could be claimed that AM can provide the means for optimal production route for MMNCs.

The synergy between AM and MMNCs shows a high potential for enabling new multimaterials products with tailored properties. The combination of metallic powder and nano-ceramic powder materials to be processed within a single process, namely AM, could enable the creation of completely new composites with improved functionalised properties, leading to a great expansion of application areas of AM. By leveraging the tunable properties of nanostructures (i.e by varying the nanostructure fractions during a part’s synthesis), the applications of printed components to create objects with graded material properties can be widely expanded. However, an integrated approach encompassing product



specifications, alloy design, process knowledge, in-process monitoring and material qualification has to be employed for a successful combination of process and new material. This has to be done taking into account the high reactivity of both Al-alloys and nanoparticles that call for safety best practices.

## **METAL POWDER**

Metal powder plays a very important role in the additive manufacturing processes and its properties influence the final quality of AM products. For example, an excessive variation on the powder characteristics may lead to a non-uniform layering with a consequent increase in defects and an important impact on the mechanical properties and the surface finishing. Hence, it is necessary to know and to evaluate the influence of the powder characteristics on the processability in the AM machines.

In particular:

- morphology;
- particle size distribution;
- density;
- porosity;
- thermal properties;
- surface properties;
- impurities.

The block diagram reported below (Figure 29) resumes several cause-and-effect relations between powder properties and powder performances.

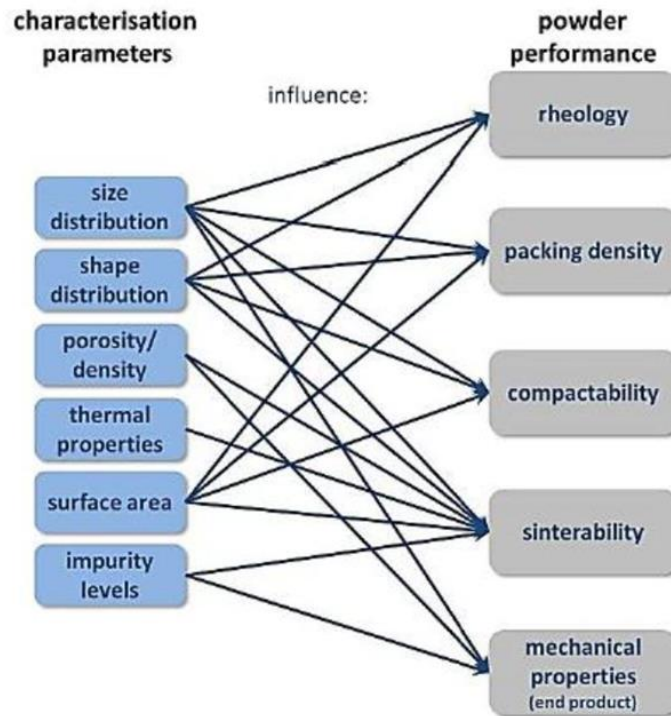


Figure 29: Impact of metal powder properties [2]

In general, different production methods lead to extremely different morphologies and particle sizes. Metal powders for additive manufacturing are usually produced by the gas atomization process, in order to obtain a spherical shape, underlining that only this morphology guarantees the right quality for AM processes.

In fact, it ensures:

- a spherical powder shape;
- a good powder packing density
- a good reproducibility of particle size distribution.

Figure 30 shows several morphologies in accordance with several production methods.

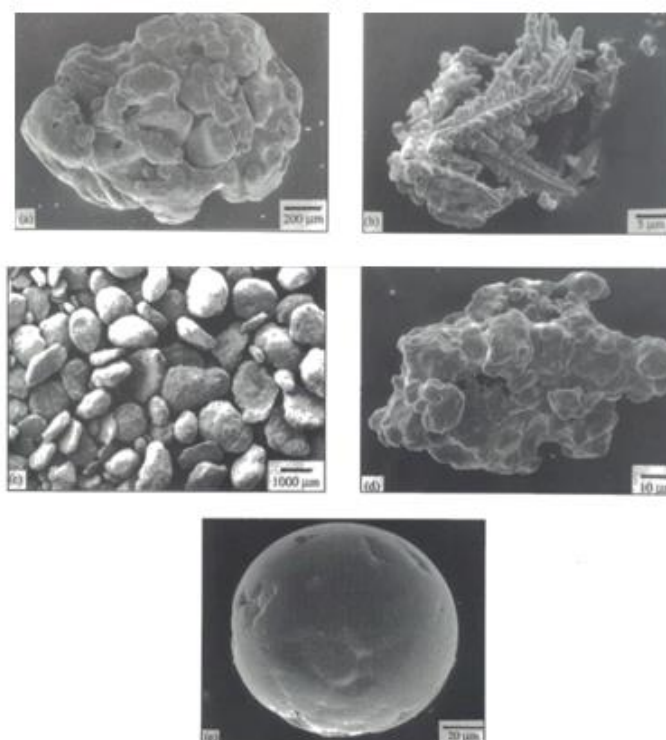


**Figure 30: Powder morphology due to different production process**  
 a) Iron - reducing chemically, b) Copper -electrolytic reduction, c) Aluminum - grinding, d) Iron - Water atomization, e) Nickel base - Gas atomization [3]

A very wide range of alloys is used on additive manufacturing machines thanks to the availability of metal powders. In Table 3 the main alloys used in AM's field are given:

**Table 3: Materials processed by AM [4]**

Material	Renishaw	EOS	SLM Solutions	3DS	Sisma	Concept Laser	Applications
Stainless steel	316L	316L, CX, GP1, PH1	316L, 15-5, 17-4PH	316L, 17-4 PH	316L	316L, 17-4 PH,91RW	Food, biomedical, consumer
Ni-alloys	In625, In718	In625, In718	In625, In718, In939, Hastelloy X	In718	Type not specified	In625, In718	Energy, motorsport
Al-alloy	AlSi10Mg	AlSi10Mg	AlSi12, AlSi10Mg, AlSi7Mg0.6, AlSi9Cu3, AlMg4.5Mn0.4	AlSi12	AlSi12, AlSi10Mg	AlSi12, AlSi10Mg	Lightweight, aerospace, aviation
CoCr-alloy	CoCrMo	CoCrMo	CoCrMo	CoCrMo	CoCrMo	CoCrW	Dental, biomedical
Ti-alloys	Ti6Al4V	Ti6Al4V, CP Ti	Ti6Al4V, Ti6Al7Nb, CP Ti	Ti6Al4V, CP Ti	Ti6Al4V	Ti6Al4V, CP Ti	Biomedical, lightweight, aerospace
Tool steel	Maraging 18Ni300	Maraging 18Ni300	H13, Maraging 18Ni300	Maraging 18Ni300	Maraging 18Ni300	Maraging 18Ni300	Tooling, aerospace, automotive
Cu-alloys					Bronze	Bronze	Energy, heat exchange
Precious					Type not specified	Au, Pt, Ag	Jewellery, design

But many other metals have been developed, such as:

- magnesium alloys;
- precious metals such as gold, silver, platinum;
- refractory metals such as Mo alloys, W and WC;
- metal matrix composites.

In the next chapter, the state of the art for MMC (Metal Matrix Composites) alloys is presented. The purpose is to understand how the lightness of the metal materials can be connected with the high mechanical performance allowed by dispersoids.

## STATE OF THE ART: OXIDE DISPERSION STRENGTHENED POWDER

In accordance with the current evolution of ODS (Oxide Dispersion Strengthened) powders for SML applications, several studies were taken in account by varying several process parameters, such as:

- dispersoid percentage
- mixing time
- mixer angular speed

The results obtained in the different studies are presented in the following sections.

### AISI10Mg + 5%wt TiC

Table 4: AISI10Mg + 5%wt TiC [5]

Ball Milling	Title	Selective laser melting additive manufacturing of TiC/AISI10Mg bulk-form nanocomposites with tailored microstructures and properties		
	Authors	Dongdong Gu, Hongqiao Wang, Fei Chang, Donghua Dai, Pengpeng Yuan, Yves-Christian Hagedorn, Wilhelm Meiners		
	Country	Cina		
	Year	2014		
	Alloy	AISI10Mg	Dispersoid	TiC
	Ratio B/P	1:1		
	Angular Speed [rpm]	200		
	Mixing Time [h]	4		

In this case study, the optimization of SLM parameters brought to a uniform distribution of TiC particles in the samples structure. Moreover, microhardness, density level (>98%), friction coefficient and wettability were improved.



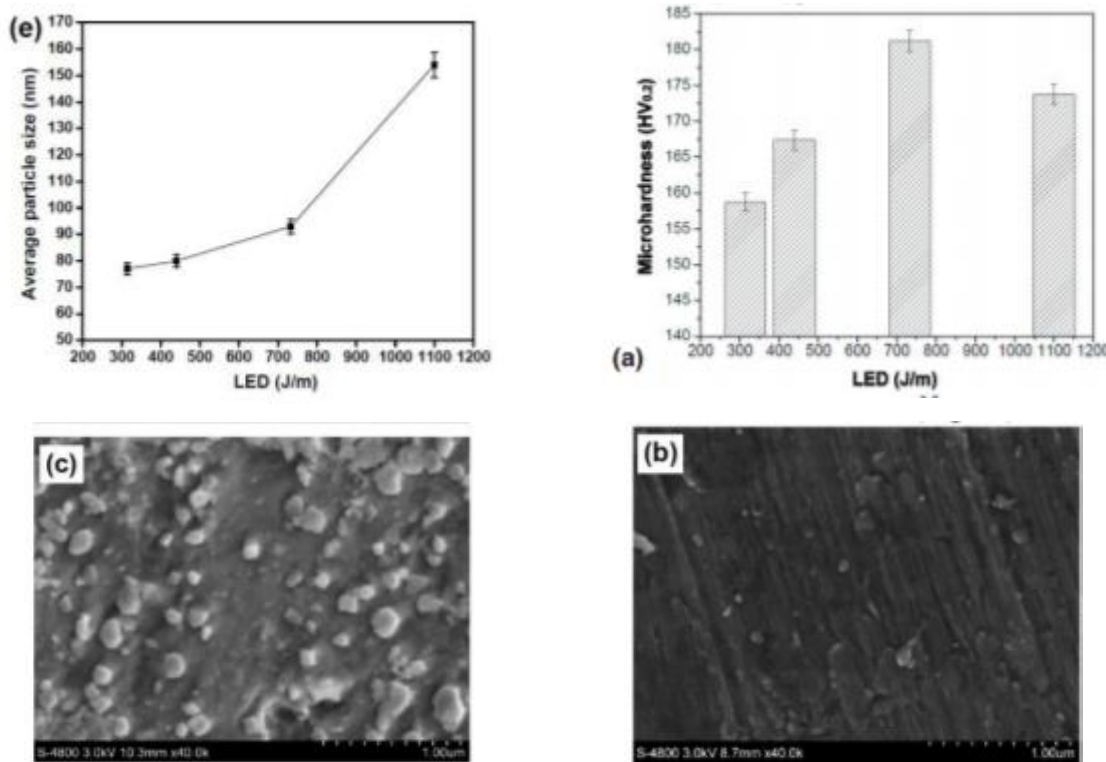


Figure 31: AlSi10Mg + 5%wt TiC [5]

Pure Al + Al<sub>2</sub>O<sub>3</sub>

Table 5: Pure Al + Al<sub>2</sub>O<sub>3</sub> [6]

Ball Milling	Title	Selective laser melting of advanced Al-Al <sub>2</sub> O <sub>3</sub> nanocomposites: Simulation, microstructure and mechanical properties		
	Authors	Quanquan Han, Rossitza Setchi, Franck Lacan, Dongdong Gu, Sam L. Evans		
	Country	UK		
	Year	2017		
	Alloy	Pure Al	Dispersoid	Al <sub>2</sub> O <sub>3</sub>
	Ratio B/P	-		
	Angular Speed [rpm]	-		
	Mixing Time[h]	20		

Ball milling was used to make the ODS powder and to keep it suitable for the SLM process. The base alloy was mixed with alumina dispersoids by varying the mixing time (Figure 32).

At the end of the milling phase the powder, mixed for 20 hours, has been considered suitable for selective laser melting. The powder lost sphericity but maintained a good flowability (Figure 33).



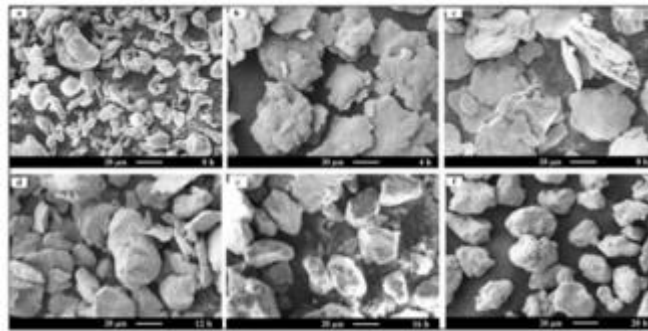


Figure 32: The morphology of Al powder after milling for a) 0h b) 4h c) 8h d) 12h e) 16h f) 20h [6]

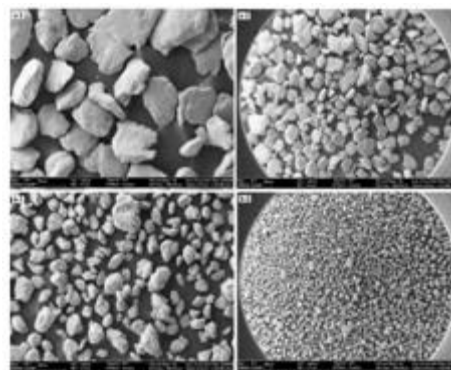


Figure 33: SEM images showing the morphology of ball-milled composite [6]

Compared to pure Al alloy, increases of 36.3% and 17.5% in yield strength and microhardness were achieved for ODS samples made by the SLM process.

### Pure Al + Al<sub>2</sub>O<sub>3</sub>

Table 6: Pure Al + Al<sub>2</sub>O<sub>3</sub> [7]

Ball Milling	Title	Microstructure evolution and mechanical properties of Al-Al <sub>2</sub> O <sub>3</sub> composites fabricated by selective laser melting		
	Authors	Jiubin Jue, Dongdong Gu, Kun Chang, Donghua Dai		
	Country	Cina		
	Year	2017		
	Alloy	Pure Al	Dispersoid	Al <sub>2</sub> O <sub>3</sub>
	Ratio B/P	-		
	Angular Speed [rpm]	-		
	Mixing Time [h]	-		

This research paper reports residual density, microstructure, microhardness and wear performance on composite parts of Al-Al<sub>2</sub>O<sub>3</sub> treated with the SLM process. In general, the defects have been significantly reduced or completely removed.



The morphology and distribution of  $Al_2O_3$  reinforcements in the alloy matrix depend on the interaction between the oxide particles and the solid-liquid interface. An optimization study of the laser speed brought to homogeneity in the dispersion of the  $Al_2O_3$  particles. The composite samples showed an excellent hardness with an average value of 175 HV0.1 and superior wear performance (Figure 34).

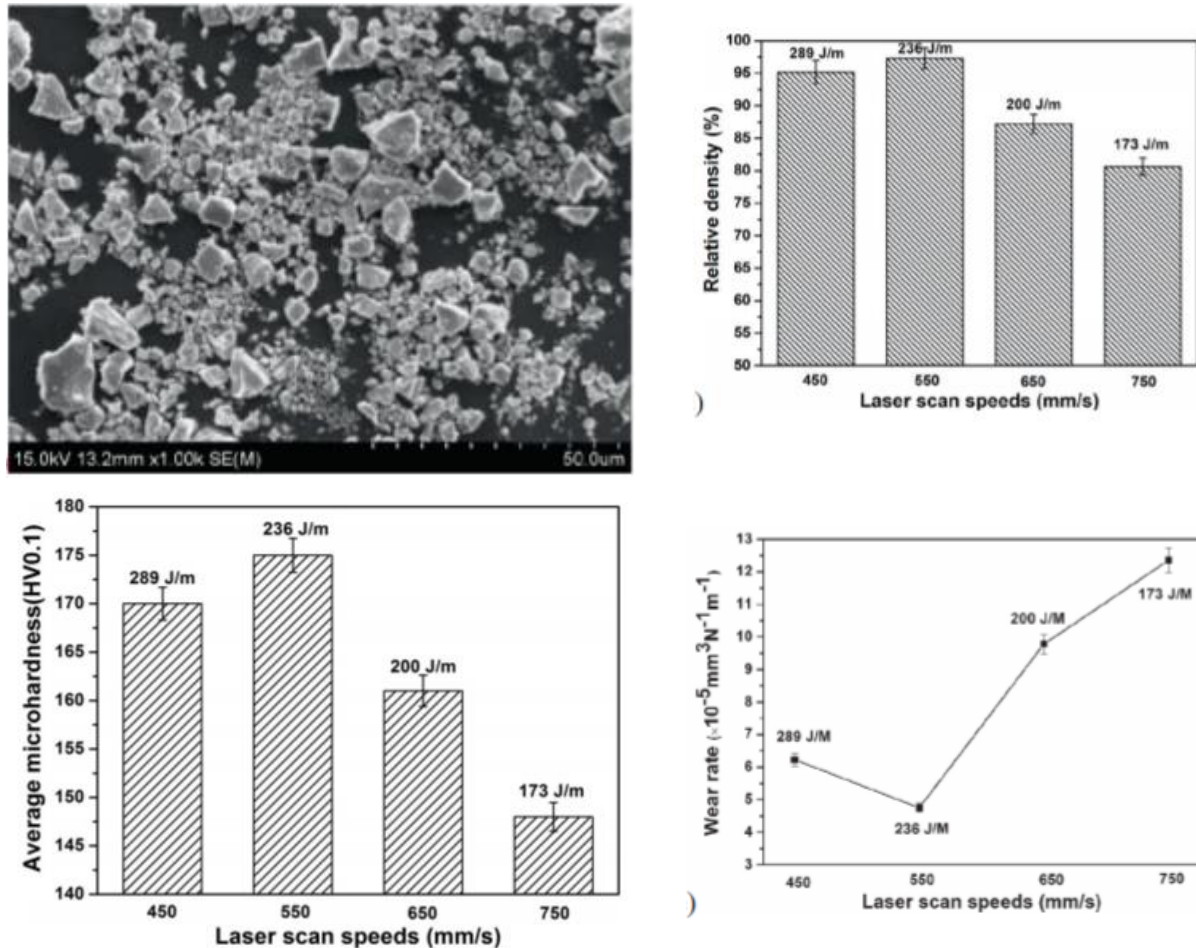


Figure 34: Pure Al +  $Al_2O_3$  results [7]

## COMPOSITE FIBRES

In this work a 3D printing process was developed by using a composite filament composed by a thermoplastic resin and a continuous reinforcing carbon fibers. It is therefore convenient to introduce the behavior of the composite material by highlighting the behavior of the main kinds of materials: isotropic and anisotropic ones. Once the main characteristics will be reported, a description of the main components and structures of composite materials will be made, focusing the attention on the reinforcing fibers and matrix materials. Most of the materials commonly used in mechanical industry, such as metal alloy and materials with a well-defined crystalline structure, have the property of being considered as

isotropic materials. This is a fundamental feature because it allows to consider all the physical and mechanical properties as constant in any direction of space. In opposition to the isotropic materials there are the anisotropic ones, in the latter case the mechanical and physical properties depend on the direction in which the material is observed; the strain-stress matrix in this case requires the estimate of 21 elastic constants for the material characterization. These characteristics are typically found at the microscopic level in material that does not have a well-defined crystalline structure or macroscopically in components subjected to technological processes that operate in different way along the space directions. Speaking of AM it is convenient to introduce the orthotropic materials; in fact, depending on the filament arrangement during the print, an object can be described by an orthotropic model (if all the layers have the same deposition direction of the filament, this case will be used for specimens printed during the project).

$$\begin{bmatrix} \epsilon_1 \\ \epsilon_2 \\ \epsilon_3 \\ \epsilon_4 \\ \epsilon_5 \\ \epsilon_6 \end{bmatrix} = \begin{bmatrix} \frac{1}{E_1} & -\frac{\nu_{21}}{E_2} & -\frac{\nu_{31}}{E_3} & 0 & 0 & 0 \\ -\frac{\nu_{12}}{E_1} & \frac{1}{E_2} & -\frac{\nu_{32}}{E_3} & 0 & 0 & 0 \\ \frac{\nu_{13}}{E_1} & -\frac{\nu_{23}}{E_2} & \frac{1}{E_3} & 0 & 0 & 0 \\ 0 & 0 & 0 & \frac{1}{G_{23}} & 0 & 0 \\ 0 & 0 & 0 & 0 & \frac{1}{G_{13}} & 0 \\ 0 & 0 & 0 & 0 & 0 & \frac{1}{G_{12}} \end{bmatrix} \begin{bmatrix} \sigma_1 \\ \sigma_2 \\ \sigma_3 \\ \sigma_4 \\ \sigma_5 \\ \sigma_6 \end{bmatrix}$$

$$\frac{\nu_{12}}{E_1} = \frac{\nu_{21}}{E_2}; \quad \frac{\nu_{13}}{E_1} = \frac{\nu_{31}}{E_3}; \quad \frac{\nu_{23}}{E_2} = \frac{\nu_{32}}{E_3}$$

**Figure 35: Strain-stress matrix**

For an orthotropic material the 9 elastic constants are:

$$E_1, E_2, E_3, G_{12}, G_{13}, G_{23}, \nu_{13}, \nu_{13}, \nu_{23}$$

For isotropic materials the 3 elastic constants are:

$$E = E_1 = E_2 = E_3, \nu = \nu_{13} = \nu_{13} = \nu_{23}, G = G_{12} = G_{13} = G_{23} = .E/2(1 + \nu)$$

They have three orthogonal symmetry planes on which the properties behave in an isotropic way; in this last case the strain-stress matrix can be defined by introducing 9 elastic constants.

These three planes are orthogonal to the axes 1,2 and 3 called principal directions of the material; in Figure 37 the difference in behavior of isotropic and anisotropic materials when they are subject to a tension or cut state (in relation to the principal directions with respect to the direction of the imposed forces) is shown. The last part of the figure is particularly interesting because it is evident the role played by the principal directions in coupling the different nature deformations (extensional-shear coupling).

The greatest resistance along the filament direction is due to the intrinsic capability of these to hold high loads while at the same time the low resistance capacity along the direction 3 is due to the filament



bonding and to successive layers adhesion. Without any doubt it is possible to impose a relative angular orientation between each layer so to increase the in-plane isotropic behavior (Figure 38), in this case a transverse isotropic model can be used. Therefore, the material shows a lower tensile strength in direction 3 (this direction is the one that is related to the layer-layer adhesion), as opposite it shows a high tensile strength in directions 1 and 2.

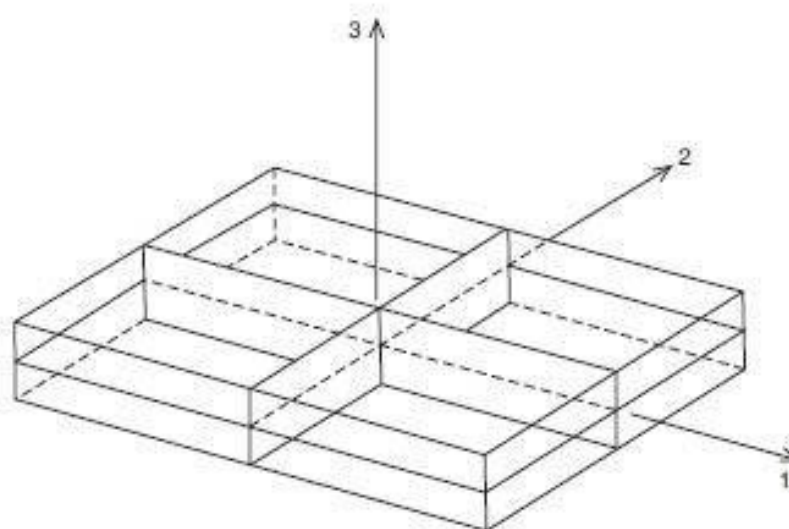


Figure 36: Planes of symmetry in an orthotropic material [8]

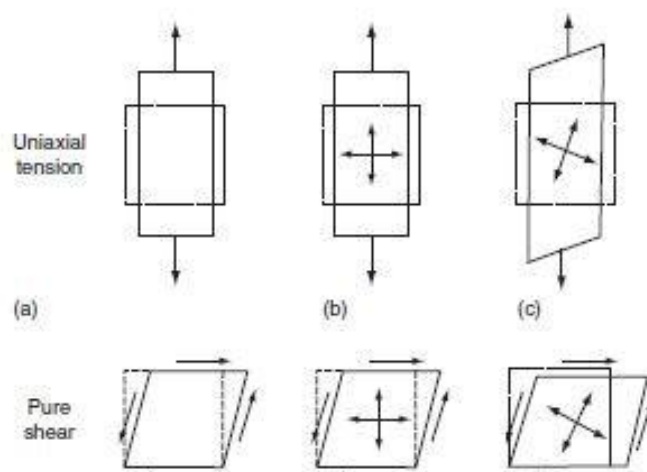
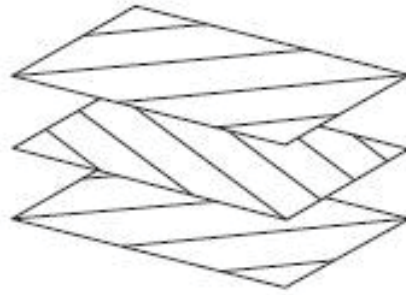


Figure 37: Difference in deformations of isotropic (a), orthotropic (b) and anisotropic (c) materials subjected to uniaxial tension and pure shear stresses (b) and anisotropic (c) materials subjected to uniaxial tension and pure shear stresses [8]



**Figure 38: Angle-ply laminate [8]**

Over the last few years, strategies have been developed, in order to use composite material in the AM field. Composite materials are formed by two different elements: a matrix and reinforcing fibers (glass, carbon, aramid, natural). The necessity was born due to the fact that the use of these materials in the military, automotive, aerospace industries (each year the demand rises by 5% [9]) makes it possible to obtain components with a very high strength-to-weight ratio and at the same time to eliminate other technological process with high waste percentages; the demand for composite material in these sectors reached almost 22 billion dollars in 2015 and the trend is exponentially growing. In the aerospace field, in particular, it is required a weight-to-volume ratio of the component as low as possible without any compromise on the strength; the AM thus appears as an ideal solution in order to observe both the constraints. The main advantages of the composite materials are:

- high strength-to-weight ratio
- resistance to surrounding environment
- high fatigue life
- easy handling thanks to reduced weight
- not influenced by magnetic fields
- low electrical and heat conductivity (it depends on reinforcing elements)
- possibly to be locally reinforced

The main used composite structures are the reinforced sheets and filaments (RF); the first ones are used in manual processes in which workers deposit manually the sheets inside a mold, the sheets are formed by many fibers arranged in a reticular pattern (Figure 39), the fibers are kept together by a thermosetting resin ("prepreg sheets").

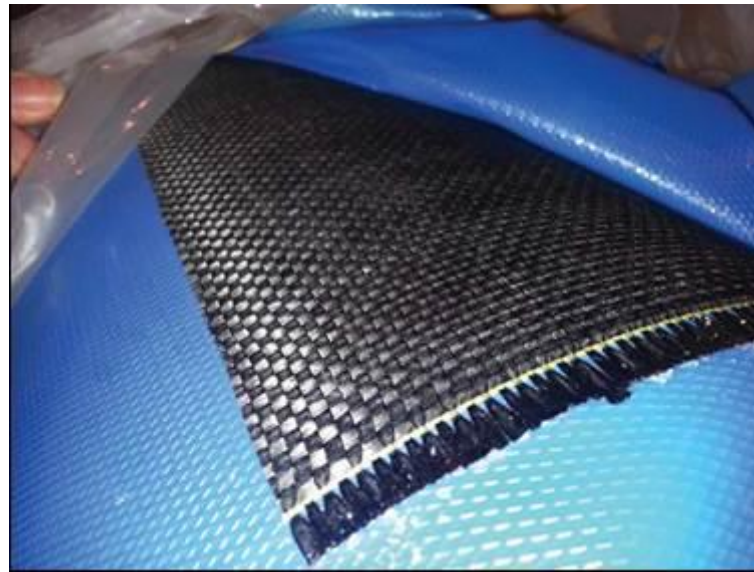


**Figure 39: Prepreg carbon reinforced sheet for had lay-up process**

The filaments can be reinforced with short, long or continuous fibers. A widely used category of composites is the one with short reinforcing fiber whose dimensions are between  $0.1\mu\text{m}$  and  $10\mu\text{m}$  [10], these particles are kept together by the matrix element. Their use is mainly conveyed by the low costs of production processes in which they are used, such as:

- low pressure injection molding
- extrusion processes
- hand-spray impregnation processes (in particular with glass fibers)

With short reinforced fiber it is not possible to assume the same deformation between reinforced particles and matrix that will elongate much more. This solution allows to increase mechanical properties, but it is not possible to have components with a high fatigue resistance; the small particles, with sharp angles, act as notch factors producing, during the working condition, an increase of the stress level at the matrix-fibers interface. Moreover, there is a discontinuity in the strain field at the interface and so a progressive detachment between particles and matrix appears. However, one of the biggest advantages over the long fiber composites is a smaller percentage of micro-voids thanks to the reduced contact surface between matrix and fibers. In order to increase the fatigue life, long reinforcing fibers of some *mm* have been used in composites. The last family of reinforcing fibers are the continuous one that in particular are used for the "commingled yarns"; they are structures formed by reinforcing fibers and a polymeric matrix (the matrix acts as binder on the fibers). In this work it will be used a continuous reinforcing carbon fiber filament whose characteristics will be presented in Chapter 2.5.2. However, in the following will be described the main reinforcing fibers that are commonly used in industry. The process used to obtain this kind of filament is called "commingling" and it is schematized in Figure 40.

The process involves the use of two or more spools that are joined together by a collimation system that leads to a cross section shown in Figure 41, in the cross section it is possible to distinguish areas of matrix and areas of reinforcing elements; the result is a composite with high strength along reinforced fiber direction.

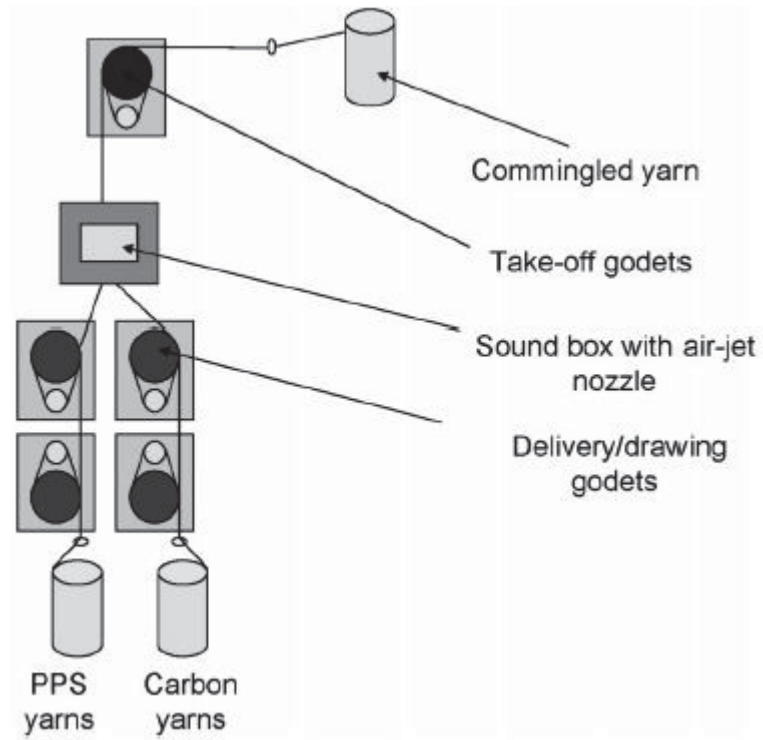


Figure 40: Manufacturing process of commingled carbon-PPS yarn [11]

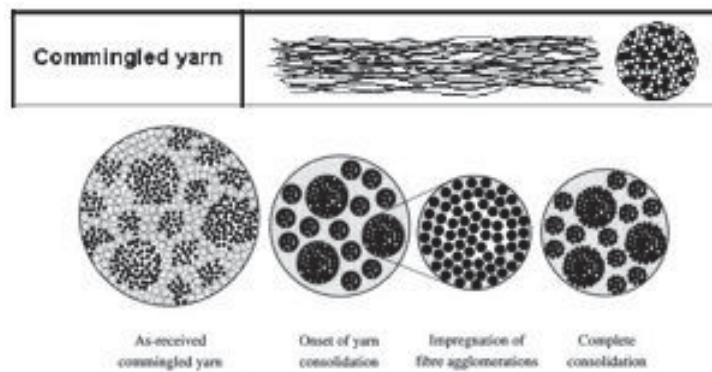


Figure 41: Commingled yarn cross section during consolidation process [12]

$$v_f = \frac{V_f}{V} = \frac{w_f/\rho_f}{w_f/\rho_f + w_m/\rho_m}$$

$$v_m = 1 - v_f$$

$$\rho_c = \rho_f v_f + \rho_m v_m$$

$$\sigma_c = \sigma_f v_f + \sigma_m v_m$$

$$\nu_{12} = \nu_f v_f + \nu_m v_m$$

**Figure 42: Mechanical properties of a composite [11]**

The reinforcing fiber materials used are in particular glass and carbon while the most used matrix elements are Polyphenylene sulfide (PPS), Polyamide (PA), Polypropylene (PP). The level of strength of the composite depends on both the fiber type and the fiber volume percentage. The matrix allows to keep the fibers in position and to transmit them the load to be held in axial direction. As first approximation when a composite is placed under tensile state (along the fiber direction) the fibers and the matrix have the same level of deformation; as soon as a critical stress level is reached, the breaking at the fiber-matrix interface appear. Considering a specimen subjected to traction condition (same direction of each reinforcing elements), it is possible to use the hypothesis of iso-deformability between fibers and matrix and then it is possible to calculate the stress generate as result of the deformation. The density and other mechanical properties of a composite can be evaluated once they are known the volume fraction of the reinforcing fibers and the single properties of both fibers itself and matrix (Figure 42).  $\sigma_c$  is evaluated considering the tensile stress of a single filament with reinforcing fibers.

$$E_{11} = E_f v_f + E_m v_m$$

$$E_{22} = \frac{E_f E_m}{E_f v_m + E_m v_f}$$

**Figure 43: Longitudinal and transversal elastic modulus**

It may be intuitive to increase the reinforcing part in order to obtain a more performance composite but this is not possible, in fact by adding more and more fibers it is no longer possible to have a homogeneous cross section and the fibers cannot be embedded completely in the matrix. It may therefore be interesting to note the trend of the longitudinal and transversal elastic modulus (with respect to the fiber orientation) as function of the fiber volume fraction; as would be expected, the fibers give a larger contribute to the longitudinal modulus while the matrix to the transversal one. The formulae defined in Figure 43 describes the trend in a quantitative way.

It would be easy think to increase the fiber percentage as much as possible, but as highlighted by the Charpy test, reported in Figure 45 an excessive fiber fraction within the cross section would cause a decrease in toughness and a brittle behavior appears; for this reason, in real application is very unusual to find composite with a fiber percentage larger than 50%. An additional factor to keep in mind, once that composite materials and volume percentages are chosen, is the angle between the fiber and the stress direction during the working phase of the component; in fact, based on the type of application and the working condition it is needed to choose the right arrangement in order to obtain the proper spatial "distribution" of Young and shear moduli.

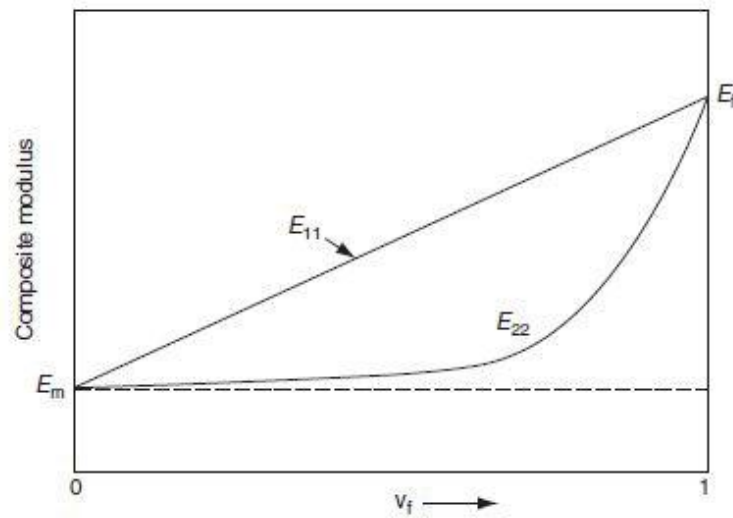


Figure 44: Composite moduli along orthogonal directions as function of the reinforcing fiber volume fraction

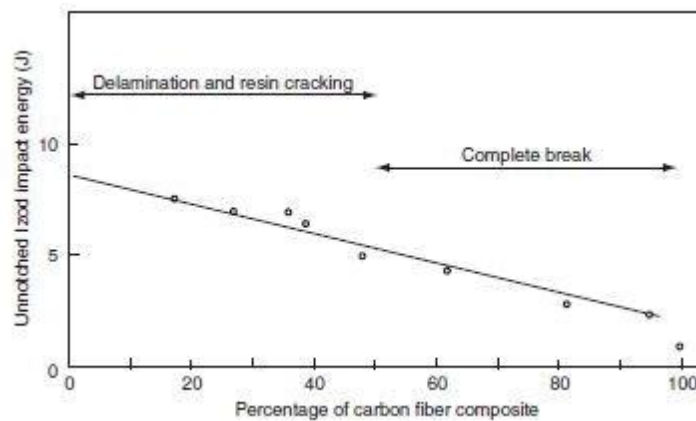


Figure 45: Effect of carbon fiber content on the unnotched Charpy impact test of 0° carbon-E-glass epoxy interply hybrid laminates

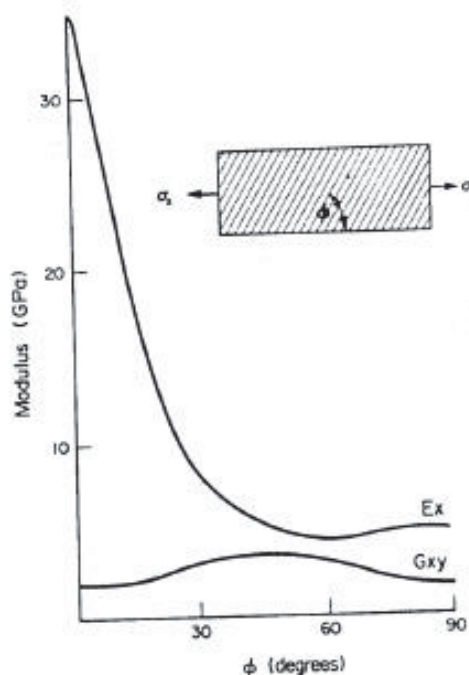


Figure 46: Young modulus and shear modulus oblique to the fibre direction in a glass-epoxy lamina with  $\nu_f=0.5$

### STATE OF THE ART: COMPOSITE FIBERS

The more common materials of reinforcing fibers are glass, carbon, kevlar and natural.

Figure 47 shows the interpolating curves of the experimental tensile test data. The characteristics of the most common commercial fibers are listed in Figure 48. In the following sections, the main qualities and defects will be described.



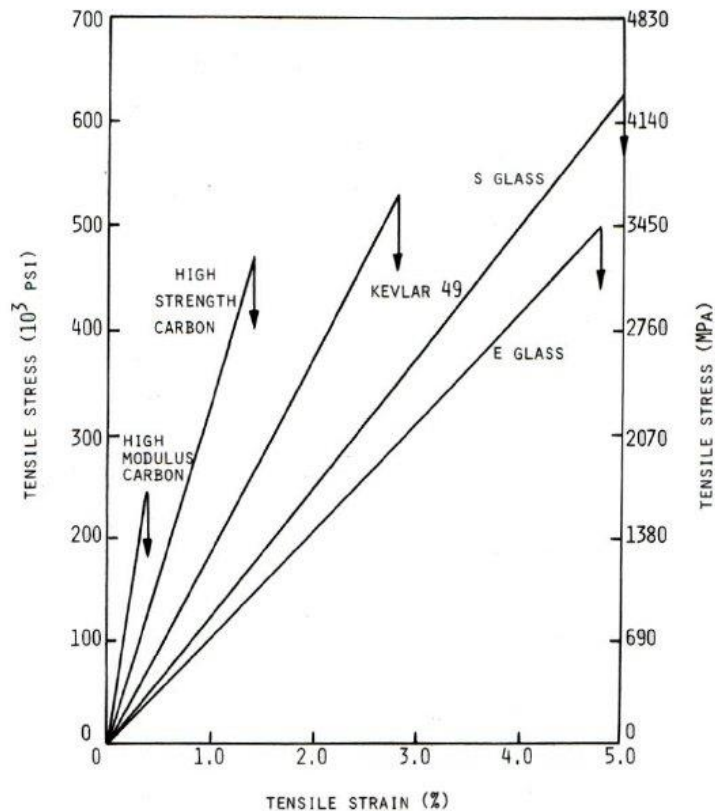


Figure 47: Tensile stress-strain diagrams for various reinforcing fibers [8]

Fiber	Typical Diameter ( $\mu\text{m}$ ) <sup>a</sup>	Density ( $\text{g}/\text{cm}^3$ )	Tensile Modulus GPa (Msi)	Tensile Strength GPa (ksi)	Strain-to-Failure (%)	Coefficient of Thermal Expansion ( $10^{-6}/^\circ\text{C}$ ) <sup>b</sup>	Poisson's Ratio
<i>Glass</i>							
E-glass	10 (round)	2.54	72.4 (10.5)	3.45 (500)	4.8	5	0.2
S-glass	10 (round)	2.49	86.9 (12.6)	4.30 (625)	5.0	2.9	0.22
<i>PAN carbon</i>							
T-300 <sup>c</sup>	7 (round)	1.76	231 (33.5)	3.65 (530)	1.4	-0.6 (longitudinal) 7-12 (radial)	0.2
AS-1 <sup>d</sup>	8 (round)	1.80	228 (33)	3.10 (450)	1.32		
AS-4 <sup>d</sup>	7 (round)	1.80	248 (36)	4.07 (590)	1.65		
T-40 <sup>e</sup>	5.1 (round)	1.81	290 (42)	5.65 (820)	1.8	-0.75 (longitudinal)	
IM-7 <sup>d</sup>	5 (round)	1.78	301 (43.6)	5.31 (770)	1.81		
HMS-4 <sup>d</sup>	8 (round)	1.80	345 (50)	2.48 (360)	0.7		
GY-70 <sup>e</sup>	8.4 (bilobal)	1.96	483 (70)	1.52 (220)	0.38		
<i>Pitch carbon</i>							
P-55 <sup>e</sup>	10	2.0	380 (55)	1.90 (275)	0.5	-1.3 (longitudinal)	
P-100 <sup>e</sup>	10	2.15	758 (110)	2.41 (350)	0.32	-1.45 (longitudinal)	
<i>Aramid</i>							
Kevlar 49 <sup>f</sup>	11.9 (round)	1.45	131 (19)	3.62 (525)	2.8	-2 (longitudinal) 59 (radial)	0.35
Kevlar 149 <sup>f</sup>		1.47	179 (26)	3.45 (500)	1.9		
Technora <sup>g</sup>		1.39	70 (10.1)	3.0 (435)	4.6	-6 (longitudinal)	

Figure 48: Properties of the main commercial reinforcing fibers [8]



## Glass Fibers

The glass fiber is, today, one of the more used solutions in the automotive and aeronautical field since it has the greatest tensile strength compared to all the other fibers. Other glass fiber advantages are the low cost, chemical stability and an excellent insulating capacity. There are, however, some drawbacks that lead, in some cases, to prefer different materials, among them there are a lower elastic modulus, a higher density, low fatigue resistance and finally the hardness of the fiber that causes a rapid wear phenomenon to the tools used in the processes (molds, cutting tools, etc ). Figure 49 **Error! Reference source not found.** shows the chemical composition of the two more common glass fiber families: E-glass and S-glass. The former has a more commercial use and is widespread, the latter has better performances and a higher cost so it is adopted prevalently in the military and aerospace industry.

Type	SiO <sub>2</sub>	Al <sub>2</sub> O <sub>3</sub>	CaO	MgO	B <sub>2</sub> O <sub>3</sub>	Na <sub>2</sub> O
E-glass	54.5	14.5	17	4.5	8.5	0.5
S-Glass	64	26	-	10	-	-

Figure 49: Typical composition of glass fibers (in weight %) [8]

## Carbon Fibers

The currently available carbon fibers have an elastic modulus with a fairly wide range, from 207 GPa up to 1035GPa; among the advantages there are a very low density, that therefore leads to a very high strength-to-weight and elastic modulus-to-weight ratios, a low linear expansion coefficient, a long fatigue life, a high thermal conductivity (useful in some applications). The disadvantages include a low static failure strain value, a high fragility (low impact resistance) and a high electrical conductivity that could generate a short circuit in electromechanical machineries; the high cost is a feature that leads to choose this material only in a certain amount of sectors. The crystalline structure shows how atoms are arranged in hexagonal shape on parallel planes; this particular arrangement is the primarily responsible for the anisotropic nature of carbon fibers (Figure 50).

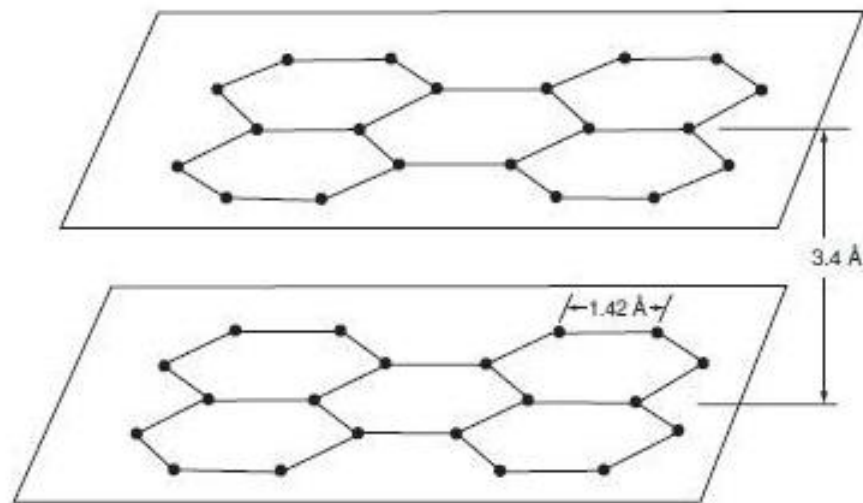


Figure 50: Arrangement of carbon atoms in a graphite crystal [8]

## Aramid Fibers

The aramid fibers are obtained from the processing of aromatic polyamides, among them the most famous is Kevlar that was patented by DuPont company in 1971. Kevlar is certainly one of the fibers that arouses more interest because it has a static failure strength about 10 times higher than that of iron and 3 times higher than that of alloy steel; it is the material with the larger strength-to-weight ratio among those known and it also has a good impact resistance. On the other hand, the aramidic fibers exhibit low compressive strength and are difficult to be machined with traditional methods. Kevlar in particular has a further drawback, it is sensitive to the humidity that causes the formation of micro-voids that can lead to early failures in the component. Used mainly together with epoxy resins, this family of fibers is used for consolidation and to repair pre-existing structures.

## Natural Fibers

A last family of fibers includes natural ones: jute, flax, hemp, coconut and banana fibers; these fibers are mentioned for completeness, in fact they are not used in the industrial sectors of interest for this work. However natural fibers are widely used in the textile industry for the manufacture of carpet, bags and ropes.

## STATE OF THE ART: RESINS

The matrix element, in a composite material, is a resin. Two possible families of resins can be identified: the thermosetting and thermoplastic ones. This element allows to maintain the reinforcing fibers in the right position during a fabrication process and, at the same time, it allow to transmit them the stresses. Moreover, the plastic matrix is the component that is responsible for the composite toughness. In order to obtain a homogeneous composite structure, it is important to select a resin with a proper viscosity.

## Thermosetting resins

The thermosetting resins harden permanently once heated up above a specific temperature (it depends on the resin) and they degrade at higher temperatures; they are often used in prepreg sheets for the manual fabrication of components. The main benefits of this resin family are:

- low price
- high operating temperature
- low viscosity

Possible drawbacks are:

- toxicity
- storage in a cold place
- complex and expansive post-processing

The last point is due to the fact that, in order to obtain the finished object with the desired mechanical properties, it is necessary to perform a "curing process"; during this phase molecular bonds are formed between two adjacent plastic chains ("cross-linked", Figure 51). This step can be performed "in-situ", for example during the AFP process [13], by applying on the working zone both pressure and heat, or it can be performed in an autoclave that is able to apply a pressure in a controlled hot environment. This last method is used in particular for large objects manufactured by applying composite sheets in a mold. The most used thermosetting resins are the epoxy and the polyester ones.

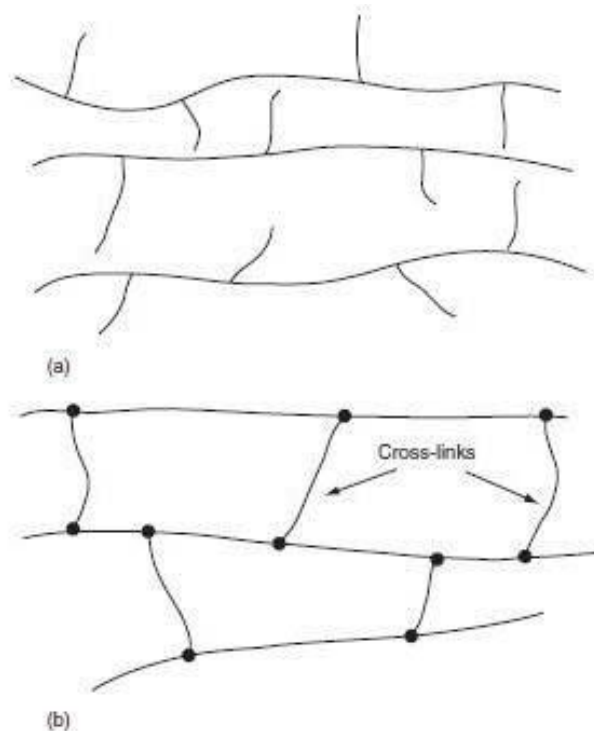


Figure 51: Difference between thermoplastic (a) and thermosetting (b) resins [8]

## Thermoplastic resins

The second family of matrix materials is composed by thermoplastic resins whose main characteristic is that they gradually lose stiffness if the temperature rises. Despite the thermosetting resins that can be used only one time, the thermoplastic materials can be used as many times as you want. The best known thermoplastic resins are: polyethylene (PE), polypropylene (PP), polyamide (PA).

Thanks to this property, thermoplastic resins are easy to use as they can be melted and formed simply providing heat and pressure. Thermoplastic polymers are composed of small molecules, these particles if bond together form a polymer chain; the result can be a crystalline or amorphous solid, the two kinds of solid have a different behavior when heated up. In fact, in order to be used and to perform a 3D printing process, the polymers must be brought to the solid-liquid state. As it can be seen from Figure 52, that describes the trend of the heat capacity as function of temperature, a crystalline solid has a well-defined melting temperature, it is required a certain amount of heat to destroy the bonding. In an amorphous solid there is the glass transition temperature (GTT), at this temperature there is a quite sudden change in physical and mechanical properties. In particular, as shown in Figure 53 the elastic modulus has a first decreasing and the material behaves as a rubber. Therefore, the GTT knowledge is important once the component is created because depending on the environment in which it will be used, the object can lose its stiffness. Thermoplastic polymers are widely used for their multiple advantages:

- processable by fusion (curing process is not required)
- great ductility and impact resistance
- chemically stable
- non-toxic
- recyclability
- easy storage
- GTT quite stable
- fatigue resistance
- low friction coefficient
- high abrasion resistance

Despite the great number of benefits that would immediately suggest the use of thermoplastic polymers, there are also some drawbacks, among these there are:

- high viscosity (larger molecular weight than thermosetting materials)
- low operating temperature



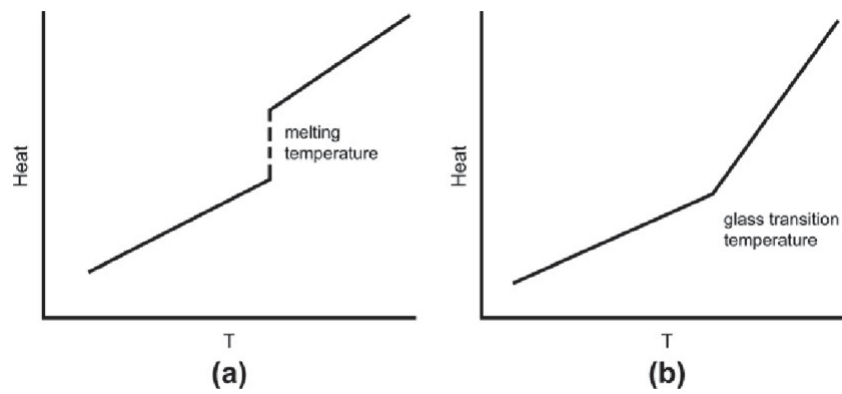


Figure 52: Melting temperature and heat capacity of crystalline (a) and amorphous (b) solids

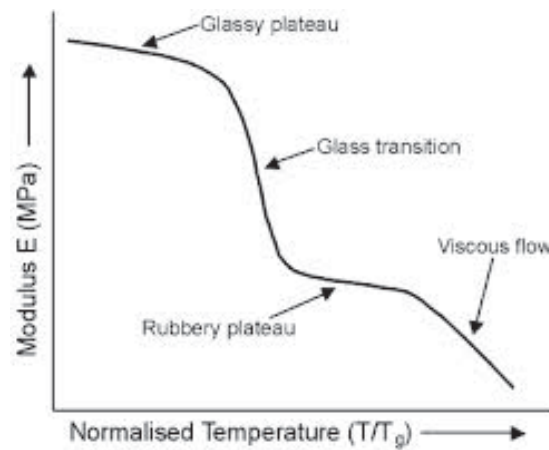


Figure 53: Elastic modulus of amorphous solid as function of temperature

### **3. MANUFACTURING TECHNOLOGIES**

The term Additive Manufacturing refers to the new generation technologies developed between the 70s and 80s in opposition to the traditional technologies of "Subtractive Manufacturing".

Initially, their utilization was limited to the production of conceptual prototypes (i.e. representing only the geometry of the component). Subsequently, thanks to technological development, it was possible to extend their application to the production of functional prototypes which reproduce the mechanical characteristics and assembly possibilities of the component.

Nowadays, Additive Manufacturing can be considered the key technology of the fourth industrial revolution, known as "Industry 4.0", which aims to improve the production methods and business models currently used in industrialized countries.

These technologies are changing completely the concept of production, which is obtained by adding material, as opposed to traditional systems of subtractive production.

It allows more degrees of freedom for designing and manufacturing components with complex shapes that are impossible to produce with traditional methods. Furthermore, it also allows to obtain lighter structures and to join components, avoiding their assembling.

Currently, these technologies allow to make components starting from several kind of materials, such as metal, polymer, ceramic or composite, for medical, aerospace, energy and automotive applications. In particular, additive manufacturing for processing metallic materials has been progressively attracting the attention of researchers and industrialists for its enormous potential.

#### **ADDITIVE MANUFACTURING TECHNOLOGIES**

Currently, there are different classifications of Additive Manufacturing processes, based on the particular production characteristics, including the method of making the layers, raw materials and the energy source used. The ASTM F2792 - 12 standard divides AM technologies into 7 classes:

- Binder Jetting: where a liquid, acting as a binder, is selectively deposited to join powders of another material;
- Directed Energy Deposition: where a heat source is used to melt a material simultaneously with its deposition;
- Material Extrusion: where the material is selectively distributed through a nozzle or orifice;
- Material Jetting: where droplets of liquid material are selectively deposited;
- Powder Bed Fusion: where a laser source melts selected portions of the powder bed;
- Sheet Lamination: where sheets of material are joined together to create an object;
- Vat Photopolimerization: where a liquid photo-polymer is selectively cross-linked, using a radiation source.



## Binder Jetting

The Binder Jetting technique (Figure 54) consists on the hardening of the powder by using a binder. In particular, a layer of powder is deposited on the working surface while an inkjet print head moves on it, releasing droplets of binder, in order to define the desired geometry.

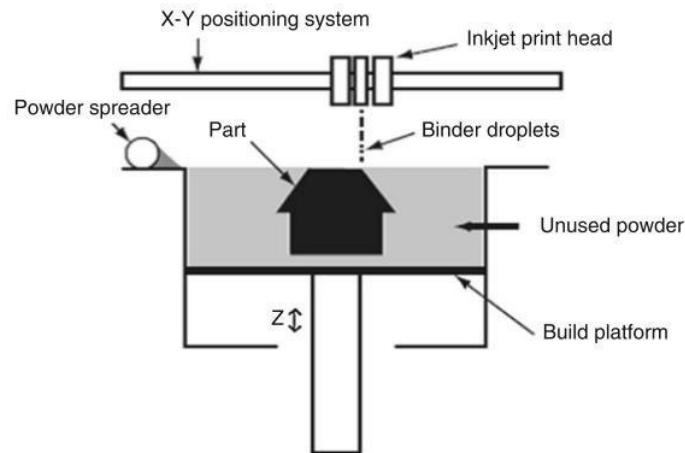


Figure 54: Binder jetting process [14]

Once the layer was printed, the working area is shifted down to process a new layer of powder as defined above. At the end, the printed component may undergo an additional hardening phase by cross-linking, sintering or infiltration.

This technology is quite economical, in comparison with the other AM process, characterised by high process speeds and the possibility of obtaining models of different colours.

The high roughness that can be obtained by the process requires a post-surface finishing treatments; moreover, the components have poor dimensional tolerances and low mechanical properties.

Generally, it is used for rapid prototyping and rapid tooling, it allows to obtain components in polymeric material (acrylate polymers), metal (tool steels, stainless steels, bronze, Inconel and tungsten), ceramic, composite and sand (moulds). The maximum dimensions of the working volume are 4000 x 2000 x 1000 mm<sup>3</sup>.

## Directed Energy Deposition

Directed Energy Deposition (DED) technology (Figure 55) consists in using a heat source that melts material during its deposition.

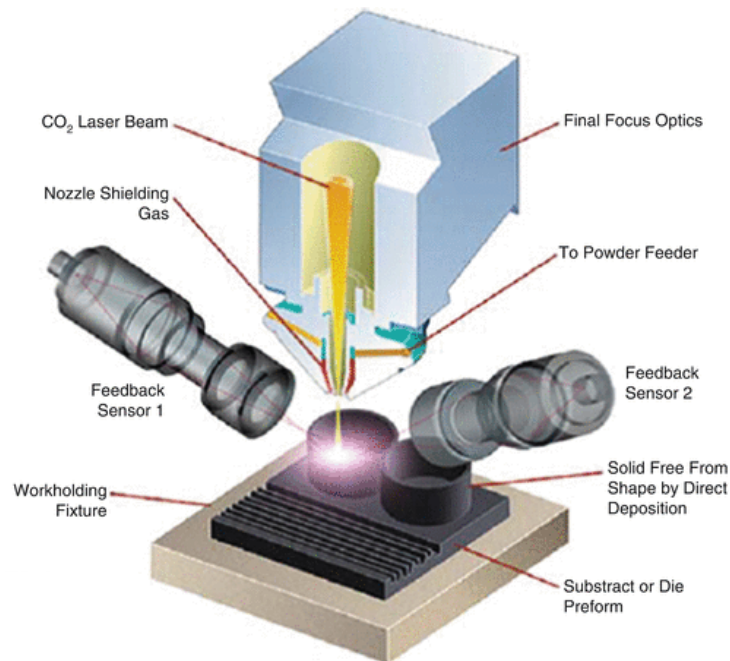


Figure 55: Directed Energy Deposition process [15]

The heat source can be a laser beam, an electronic beam or a plasma source, while the raw material can be powder or wires.

There are two several technologies:

- Laser Engineered Net Shape (LENS)
- Electron Beam Additive Manufacturing (EBAM)

The first one uses a deposition system made up by a laser, a nozzle for the distribution of power and a system for the dispersion of inert gases.

The head allows in the same time the deposition and melting of the powders on the substrate. In particular, the laser partially melts the material already deposited, creating a small area in the liquid state called melting pool.

The second one follows the same procedure described above but in this case the heat source is an electron beam that works in vacuum.

DED techniques allow to obtain components characterized by high mechanical and thermal performance and to process a large number of metallic materials (tool steels, stainless steels, aluminium and its alloys, Inconel, chromium-cobalt alloys, nickel-based alloys, copper and its alloys, tin, tantalum, titanium and its alloys, Waspaloy) and carbides.

Furthermore, the process is characterized by high efficiency and; in addition, it allows the repair of large parts. However, it is underlined that the high costs are required for initial investments and operations.

The roughness of the components is not optimal and they can undergo a considerable contraction during the solidification phase. The maximum dimensions of the working volume are 4000 x 1200 x 1200 mm<sup>3</sup>.

## Material Extrusion

Material extrusion technology (Figure 56) consists on the extrusion of a low viscosity material.

Wires, which are used in this process, are generally made of thermoplastic polymer and they are forced to pass through a heated nozzle that allows their softening.

According to the component shape that it has to be manufactured, the nozzle is moved on the horizontal plane xy, depositing the material which, instantly, cools and solidifies.

When a layer is completed, the working plane moves along the z-axis to process the next one.

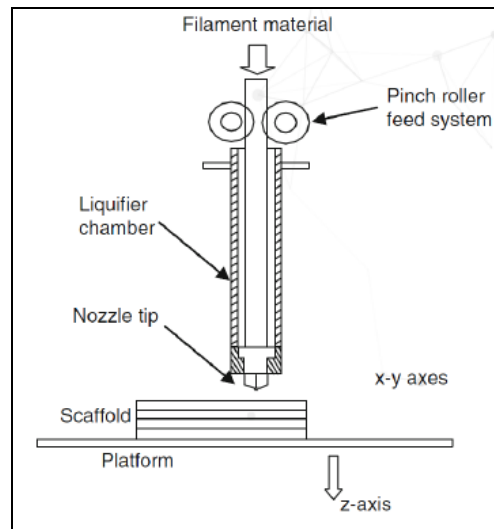


**Figure 56: Material Extrusion process [15]**

This process, which is used mainly for rapid prototyping, is characterized by high cost-effectiveness. It does not require the use of lasers, and it needs of extremely simple post-printing operations.

However, the process speeds are limited because it depends on the heating speed of the nozzle and the viscosity of the raw material.

The roughness and the porosity level of the components are high; moreover, several kinds of thermoplastic polymers can be processed such as waxes, nylon, PLA, PVA, PP, technopolymers, styrene polymers, thermoplastic elastomers and some blends.

## Material jetting

Material jetting (Figure 57) consists of the distribution of photopolymer droplets, through a series of nozzles, that will make the several layers of the component. In this way the material can be deposited quickly and linearly and hardened by an UV source.

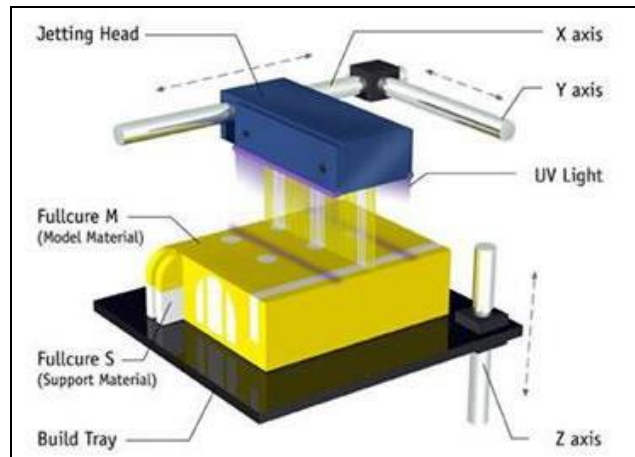


Figure 57: Material Jetting process [15]

This process, which is mainly used for rapid prototyping and rapid tooling, is characterised by ease of use, high process speed and economy. Furthermore, it allows to choose several materials and colours. The materials range is limited to polymers. In particular, acrylates, waxes, elastomers, PCs and advanced nano-ceramic composites. The maximum dimensions of the working volume are 1000 x 800 x 500 mm<sup>3</sup>.

## Powder Bed Fusion

Powder Bed Fusion technologies involve the melting of selected portions of powder, which is arranged on a working platform, using a heat source (Figure 58).

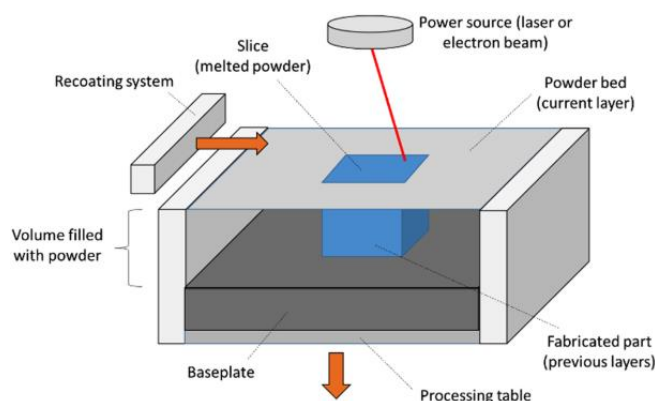


Figure 58: Powder Bed Fusion [16]

PBF technologies can be classified according to the heat source that is used:

- *Selective Laser Sintering (SLS)* uses a laser source for sintering a layer of polymer powders. The process begins with the distribution of a layer of powder and a laser beam, which draws on the powder bed the desired geometry, induces its sintering. Also in this case the work platform is then shifted downwards to process a new layer of powder.
- *Selective Laser Melting (SLM)* or *Direct Metal Laser Sintering (DMLS)* are two processes similar to SLS process but in this case it is used metal powder. However, in SLM process the powder is completely melted, while in DMLS it is consolidated through a sintering process.
- *Electron Beam Melting (EBM)* uses a high-energy electron beam as heat source to induce the fusion/sintering of metal powders. In general, EBM makes components with lower residual stresses than the others defined above, generating less part distortion and reducing the number of supports. However, it requires to work in high vacuum and can only be used on conductive materials.

These technologies allow to obtain components which are defined by high mechanical and thermal performance, in spite of that they are characterized by high costs (initial investment, maintenance, machine operation, plant requirements that must be met to operate).

These techniques, which can be used for rapid prototyping and for direct production, allow the use of a wide range of polymeric materials (Nylon/PA, PU, PP, PS, ABS/PP, TPU, PMMA, PEEK, Alumide), metallic materials (aluminium and its alloys, bronze, chromium-cobalt alloys, copper, various types of steel, Inconel, precious metals, titanium and its alloys, iridium, magnesium, nickel and its alloys, refractory metals) and composites (PA reinforced with glass, carbon or mineral fibres).

These techniques are the most performing in the field of additive manufacturing: they allow good geometric tolerances, excellent mechanical properties, and good thermal and process properties. The maximum dimensions achievable for metals components are 800 x 400 x 500 mm<sup>3</sup>, while for polymer components are 1400 x 700 x 500 mm<sup>3</sup>.

## Sheet lamination

The sheet Lamination process (Figure 59) is based on the overlapping of sheets of shaped material that can be joined together by different methods (glue, ultrasound, thermal, mechanical).

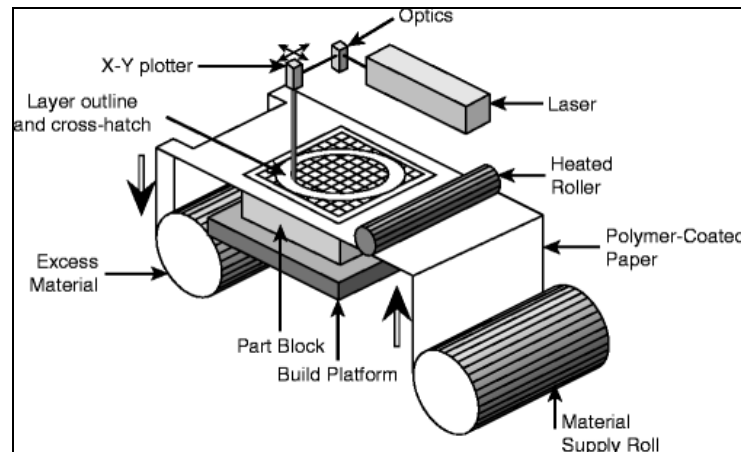


Figure 59: Sheet Lamination process [15]

There are two types of processes in accordance with the timing with which the forming of the sheets is generated:

- bond - then - form: sheets are glued together and then they are cut to create the desired shape;
- form - then - bond: sheets are cut to obtain the desired shape and, subsequently, they are arranged and glued to form the component

The main benefits of this technique are: the low cost, the speed of the process, the possibility of making large objects by combining several materials.

However, as opposed the drawbacks are: the high amount of waste and the need for support structures. Moreover, it can process a limited number of materials.

These technologies make it possible to produce components in metallic materials (stainless steel, aluminium and its alloys, copper and its alloys, titanium and its alloys) and composite materials (polymer matrix reinforced with glass, carbon or aramid fibre). The maximum dimensions of the working volume are 1830 x 1830 x 950 mm<sup>3</sup>.

### Vat Photopolymerization

Vat Photopolymerization technology (Figure 60) is a process in which a polymeric material, in its liquid state, is selectively cross-linked, using a radiation source.

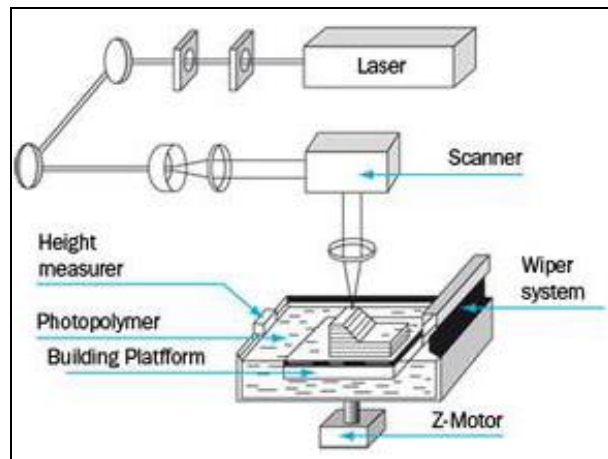


Figure 60: Vat Photopolymerization process [15]

Hereafter, it will be described the several methods of production:

- Stereolithography works by using a high-powered laser to harden liquid resin that is contained in a reservoir to create the desired 3D shape. In a nutshell, this process converts photosensitive liquid into 3D solid plastics in a layer-by-layer fashion using a low-power laser and photopolymerization.
- Direct Light Processing (DLP), which is very similar to SLA, differs in the method of cross-linking of the layer: while SLA uses a point laser that moves on the working area, DLP uses a digital light projector. It allows to define the geometry of the layer in a single step.

This technology enables to have a good roughness and geometrical tolerances, a high level of detail also for complex geometries and an optimal process speed.

However, the cost of the materials is very high and it is necessary to lead the process in a controlled environment. It is used for rapid prototyping and also for direct production. These technologies make it possible to produce components in photopolymers (acrylates and epoxy resins), "green" ceramics (alumina, zirconia, silicon nitride, tri-calcium phosphate) and composites. The maximum dimensions of the working volume are 500 x 760 x 560 mm<sup>3</sup>.

## SYSTEM FOR THE LAYING OF COMPOSITE FIBRES

With the spread of composites with reinforcing fibers in the industry, new technological processes, more and more automated and efficient, have been developed in order to increase productivity and minimize processing waste. In this way the companies sustain large initial investment costs but at the same time there is a decrease of worker costs. The first used production process such as the hand lay-up was manual and needed post-processing operations; later, almost fully automated processes such as pultrusion, filament winding, automated tape laying (ATL) and automated fiber placement (AFP) were developed. These technologies will be described in the following sections.

## Hand lay-up

The hand lay-up was the first process in which composite materials are used; prepreg sheets composed by crossed reinforcing fibers and a thermosetting resin, are laid one on the other inside a mold. After the part creation, a polymerization in autoclave is required in order to harden the object (pressure and temperature are respectively in the range of 1-10 *bar* and 24-180°C); in order to promote the trapped air bubble disappearance, that could decrease the mechanical properties of the final component, a manual pressure is applied or a cylinder is rolled on the surface before applying a new sheet. Finally, before the polymerization phase in autoclave, the component is placed in a membrane in which vacuum is obtained to favor the compaction and the formation of bonds between the prepreg sheets. A post-processing stage is often required to remove the excess of material coming out of the mold edges. The main parameters of hand lay-up process are the degree of polymerization, the sequence and orientation of sheet deposition, the level of porosity and the compaction pressure imparted to the layers. For economic reasons, an in-depth check on all the parameters is not carried out and, therefore, the fabricated products have often different mechanical and geometrical characteristics, this aspect is mainly due to the fact that all the operation of layer deposition and compaction are performed manually [17-18]. To overcome these problems, automated deposition systems have been developed. In this way the processed objects are more homogeneous and there is a significantly low amount of labor. The most used types of materials with this technology are the Glass Fiber Reinforced Plastic (GFRP) and the Carbon Fiber Reinforced Plastic (CFRP), they are both used for example for the manufacture of automotive parts, boat hulls and fuselages and wings of ultralight aircrafts.

## Pultrusion

Pultrusion is a continuous production process in which the fibers and the matrix pass through a mold to obtain objects with a constant cross section such as beams, cables, pipes and flat sheets. The entire technological process is sketched in Figure 61, where it is possible to appreciate the stage in which the fibers of reinforcing material flow through a resin bath before forming the cross section; at the exit of the machine there is a diamond saw that allows to cut the piece to the established length once the material has cooled down by means of an air or water flow. The most important phase of the whole process is the resin bath, in fact the final mechanical properties of the composite and therefore of the object, depends on the resin viscosity and temperature and the bath time of the fibers. The simplest way to improve composite strength is to slow down the speed of the entire line so as to maximize the fiber-resin interaction time and thus increase the amount of matrix material among the fibers. Usually the resins used in pultrusion have a viscosity range of 0.4-5  $Pa \cdot s$ ; this value range is namely related to the fact that it is not possible to adopt low viscous resins as it would result in a rapid draining of same from the fibers once it come out of the tank where the bath takes place. Very often it is common to find intermediate steps within the manufacturing sequence in order to improve the matrix-fiber adhesion and to give to particular chemical-physical properties such as resistance to ultraviolet rays and fireproofing ability. In commercial applications, thermosetting plastic are largely used (in particular polyester), in few case thermoplastic material such as PEEK are used [8].



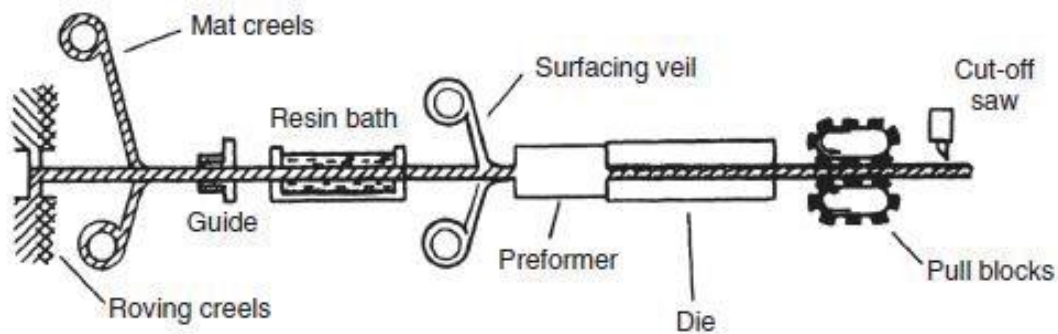


Figure 61: Pultrusion process [8]

### Filament Winding

In a Filament Winding process as the one in Figure 62, a series of parallel fibers passes into a resin bath and then it is wound onto a body that acts as a mold. The relative motion of the bodies is given by a spindle which rotates the mold and by a slider which moves the impregnated filaments parallel to the spindle rotation axis. The components that can be easily processed with filament winding are the axisymmetric ones or with a polygonal cross section with concave sides, such as shown in Figure 63 (a) and (b). This technology is used for automotive drive shafts, helicopter blades, pressurized vessels, pipes, missiles and storage containers. One important parameter to be taken into consideration is the fiber tension which is continuously tuned by means of a force control system that moves a series of mobile rollers. The filament tension ensures that the wires remain parallel to each other so as not to leave unfilled mold spaces and it also allows to generate a sufficient contact pressure between two layers in order to have a proper adhesion. The process is quite fast if compared to other AM processes, in fact it is possible to guarantee a linear covering of the mold with a linear speed of  $110\text{ m/min}$ ; of course in case of low dimensional tolerances, smaller speeds are used. The filament is wrapped following a helical path forming an angle between  $0^\circ$  and  $90^\circ$  with respect to the axis of rotation; since the slider moves alternately from right to left, a crisscross pattern that influences the mechanical characteristics of final component is created. The filament winding is not the most suitable process for mechanical parts subject to large axial stresses, but, nevertheless, using helical angle low ( $\approx 0^\circ$ ) it is possible to improve the axial strength; angles high ( $\approx 90^\circ$ ) are used in particular for pressurized containers in which the largest stress is the tangential one with respect the axial one.



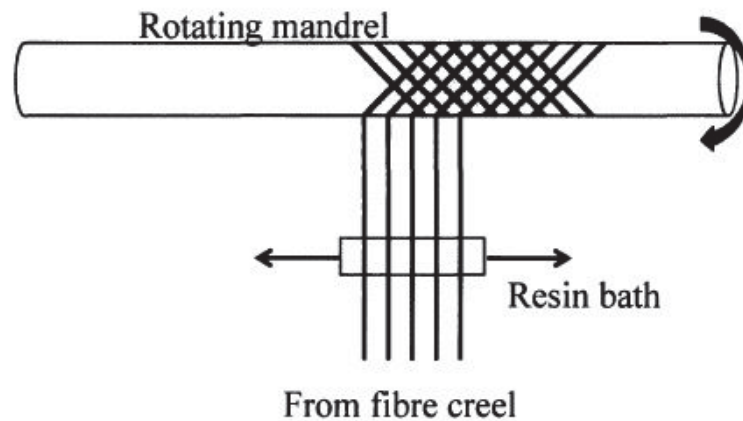


Figure 62: Filament winding process [19]

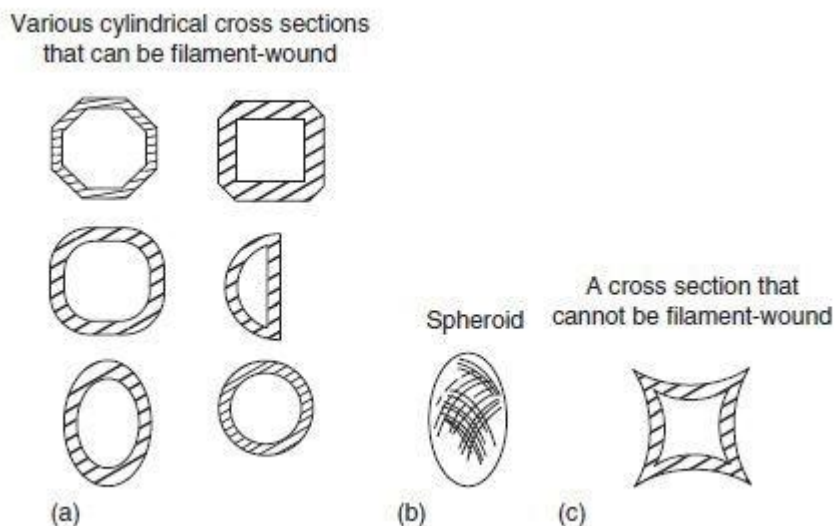


Figure 63: Cross section of possible filament-wound parts (a and b), example of a cross section that cannot be filament-wound (c) [19]

### Automated Tape Layering

The introduction of composites in the aerospace industry, allowed designers to reduce the weight of structural parts without compromising their strength; however, the hand lay-up process described above does not permit to produce large components at low production cost and so new strategies have been developed. The automated tape layers (ATP) is an automatized process that allows the deposition of thermosetting prepreg composite materials in order to create the object through layer adhesion; Figure 64 shows that the bond between two layers is facilitated by the pressure exerted by a consolidation roller. The first patent related to this system is due to Chitwood and Howeth in 1971 [20]; the two inventors used a CNC machine to (depositing material on a rotating plate) create parts with very simple shapes.



Over the years, more general material deposition methods were developed, they allowed for an increase in production speed and, at the same time, allowed the creation of objects with a greater geometrical complexity.

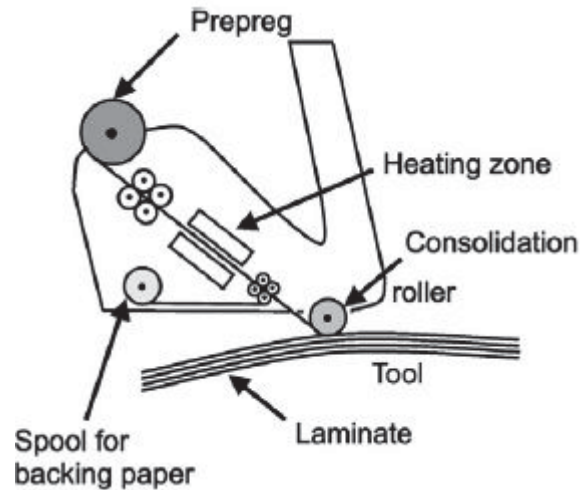


Figure 64: ATL printing head [21]

In the 80s, Eaton and Saveriano introduced a deposition system composed by a light tool that allows to increase the deposition speed, always on a rotating platform, from 20 *m/min* to 60 *m/min*. Only starting from 1985 it has been possible to develop processes that allow to deposit the prepeg tape into a curved molds, thanks to the introduction of laser measurement system, ultrasound devices and force controls (perpendicular to motion direction). In 1995, Olsen and Craig studied in a more quantitative way the process parameters, in particular the influence of deposition rate and compression roller geometry and material on the layer adhesion phenomenon. They verify that the force needed to compact the layers must be higher than during the vacuum de-bulking due to the fact that the force is applied over a shorter time period. However, despite the pressure exerted by the compaction roller, it was not always possible to obtain a satisfactory adhesion between the layers; so in the 90s for the first time it was decided to introduce a heating system in order to heat up the layer-layer interface and therefore allowing stronger bonds between thermoplastic layer matrix, facilitating the molecular diffusion. In this way it has been possible to reduce delamination problems. In case of use of matrices with thermosetting properties, the common heat sources induce a partial hardening and it is therefore necessary to either rise up the local temperature (increasing the heating flux) or introduce a curing stage in autoclave. The main advantages of this ATL process are:

- higher deposition rate
- possibility to manufacture larger components
- possibility to use many kinds of matrices

However, ATL is not without limits, including:

- high initial investment for machineries
- production wastes higher than those of other technologies, such as automated fiber placement (described in the next section)

- limitations in the geometrical complexity of the components that can be realized.

These last two points deserve a deepening, both are related to the steering radius that the roller can perform and to the tape width. Figure 65 shows three possible choices on how to deposit the material in order to minimize the material to be added or removed to obtain the desired profile. In the first case there is a material missing so the final geometry is not the desired one and could be useful to add a production step in order to recover the right object profile; in the second case the material is more than the necessary and the wanted geometry can be met by removing the excess of material. In both cases further production steps are required. Regarding the second problem, it is possible to identify three main cases, shown in Figure 66, which are the main source of resistance reduction and delamination of a component. Automated fiber placement allows to reduce almost completely this problems because of a lower filament width, on the contrary the building object time increases.

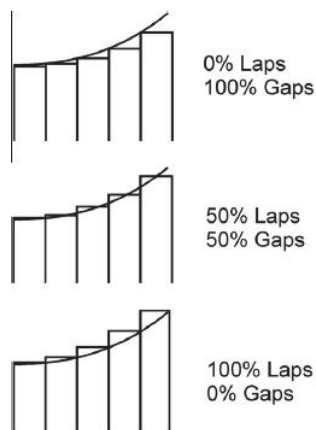


Figure 65: Laps and gaps during ATL process [20]

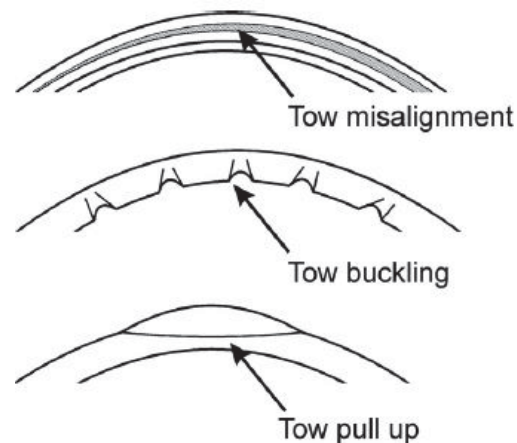


Figure 66: Tow steering defects [20]

Contrary to what happens in hand lay-up, the ATL, being an automatized process, allows to eliminate human errors and therefore it is possible to minimize the scraps and so reduce time and costs. An example of machine used in ATL process is shown in Figure 67, the machine is composed by 10 axis, 5 of them are used for moving the building platform, other 5 are used for positioning the deposition system. The complexity of this machine has a large impact on initial plant costs both for robots itself and control systems but there is, at the same time, a decrease in labor hours of workers up to 85% thus allowing a significant saving on operative costs.

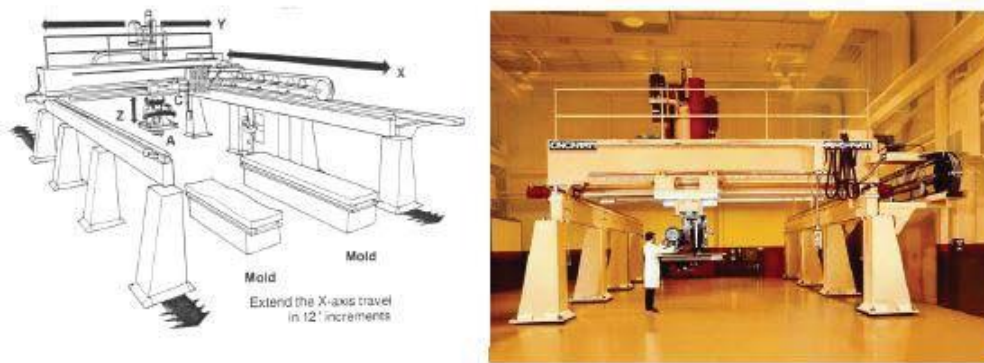


Figure 67: ATL deposition and motion systems [22]

### Automated Fiber Placement

The automated fiber placement, or AFP, differs from ATL for the width of the used material (composite with thermosetting matrix), in fact in this case a filament with a round cross section (diameter is typically 3.2 mm, 6.4 mm or 14.7 mm) is used [23]. As Figure 68 shows, there are single filaments wound on independent spools integrated in a feeding system mounted on a robot manipulator. With this configuration it is possible to choose the number of wires to be used and therefore the final diameter of the filament to be deposited on the mold. The current systems can integrate and manage with up to 32 independent wires controlling their tension and feeding speed. The number of used wires depends on the characteristics of the wire material and geometric complexity of the object to fabricate; in particular, as seen for the ATL, it is necessary to keep under control, during the generation of the working path, the steering radius that the robot head performs. Since each wire can be cut and supplied independently from the others (the final filament diameter can be modified at any given moment during the printing operation), the previously mentioned problem can be partially eliminated by decreasing the numbers of wires and then the diameter of the filament to be deposit. Therefore, when the steering radius is too small, the filament will have a smaller diameter. In the same way it is possible to reduce the problem of waste material by following in a more accurate manner the object profile sides. The AFP productivity is lower than the ATL, therefore AFP is used only for small components with complex geometry. The printing head system is similar to that of ATL and it is composed by two counter-rotating rollers that allow to feed the filament, a system that locks and cuts single wire or the overall filament and a heated compaction roller (Figure 69) that partially cures the thermosetting resin. Also in this case, due to the limited contact time between the roller and the layer adhesion zone, it is not always possible to obtain a satisfactory bonding between the different layers and in-situ curing stage so that it is therefore necessary to introduce an external thermal source; the most common ones are laser, ultrasound and radiating sources [13].



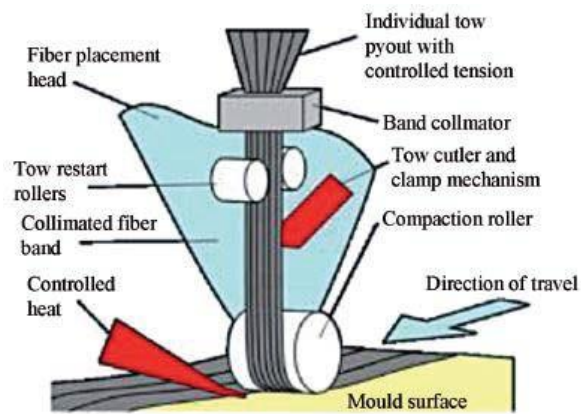


Figure 68: AFP printing head [24]

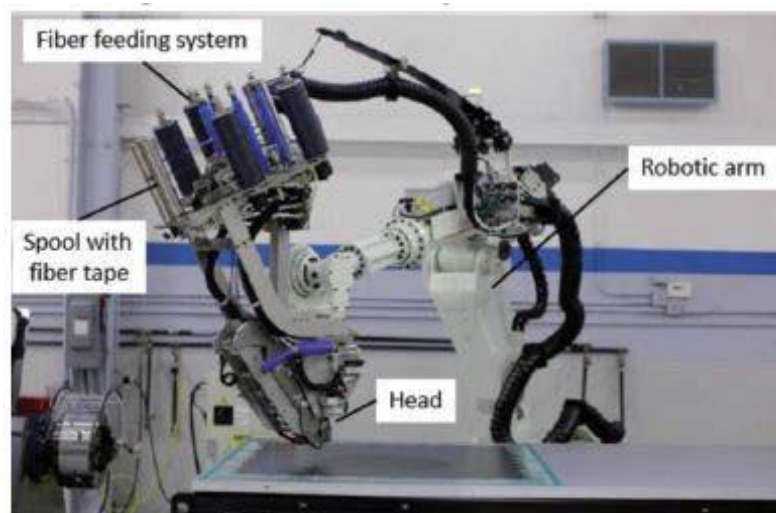


Figure 69: Robot manipulator used for motion during an AFP process [24]

## **4. POWDER MANUFACTURING**

---

Additive manufacturing is a novel method of manufacturing parts directly from digital model by using layer by layer material build-up approach. This tool-less manufacturing method can produce fully dense metallic parts in short time, with high precision. Features of additive manufacturing, likes freedom of part design, part complexity, light weighting, part consolidation and design for function, are garnering particular interests in several engineering fields.

The bibliographical analysis has shown that sectors such as automotive, aerospace, automation are focusing on ODS technology (oxide-dispersion-strengthened) to join together lightness and superior mechanical properties.

Aluminium alloy powders strengthened with alumina dispersoids suitable for the additive SLM (Selective-Laser-Melting) process were produced to obtain specimens necessary for mechanical and tribological characterization.

The main objective is to combine the intrinsic lightness of the material, considering a further lightening granted by a topological development, with an increase of the mechanical performance allowed by an oxide dispersion.

Master alloys were produced in the VIM (Vacuum-Induction-Melting) plant and subsequently processed in the VIGA (Vacuum-Induction-Gas-Atomization) plant, in order to obtain metal powders in the granulometric range of interest (15-65  $\mu\text{m}$ ).

In order to evaluate statistical data, such as the main equivalent diameters and the particle size distribution, necessary to define the quality of the powder in terms of size, granulometric analysis were performed in a laser diffraction granulometer. This instrument is able to analyse a wide granulometric range, which can vary from hundreds of nanometres to several millimetres. The measurement is based on the physical principle that particles radiated by a laser beam spread the light with an angle related to their size.

The aluminium powder and alumina particles were subsequently mixed in a miller to obtain ODS powders. The main purpose is to obtain, through the Ball Milling process, particles of aluminium embedded by nanometric dispersoids of alumina in order to have, at the end of the SLM (Selective Laser Melting) process, samples characterised by a homogenous oxide dispersion.

The analysis was focused on the search of process parameters (dispersoid percentage, mixing time, B2P weight ratio) that optimize simultaneously the powder processability in SLM and the mechanical characteristics of the final product.

### **VACUUM INDUCTION MELTING PROCESS**

---

Vacuum induction melting (VIM) is the most versatile melting process for the production of several alloys based on Fe, Ni and Co. Moreover, this process is also the only one allowed for many applications in the energy, aerospace and nuclear sectors.



The VIM process is carried out by a copper coil cooled by water and supplied by AC, which wraps a crucible in refractory material (alumina, zirconia or graphite). The magnetic induction makes eddy current into the charge which melts for Joule's effect. The features of the VIM can be summarised as follows:

- production flexibility;
- isolation of the molten alloy from atmospheric contamination: the working atmosphere can be controlled in order to prevent the loss of reactive elements due to oxidation;
- possibility to control the melting chamber pressure in order to manage the chemical reactions depending on it;
- accurate temperature control;
- excellent level of homogeneity thanks to the magnetic stirring;
- removal of undesirable trace elements with high vapour pressure;
- removal of dissolved gases such as hydrogen and nitrogen.

Through the VIM process, one AlSi<sub>7</sub>Mg ingot was produced. This ingot was required to carry out the planned atomization.



**Figure 70: Steps of VIM process**

In order to meet the specific requirements for AlSi<sub>7</sub>Mg, an first on-line chemical analysis, before casting, and a second chemical analysis on the ingot produced were accomplished. In particular, FRX + LECO analysis were done during the VIM process and ICP-OES + LECO analysis were done on ingot samples.

Chemical results are reported below.

**Table 7: Chemical results**

AlSi7Mg	Values (%)
Al	Bal
Si	7
Fe	0,35
Cu	0,10
Mn	0,30
Mg	0,4

## GAS ATOMIZATION PROCESS

In the gas atomisation process, utilised for powder manufacturing, generally the metal charge is melted in inert atmosphere. When the desired temperature of the molten bath is reached, the liquid is tapped into a tundish having a nozzle at its base. Therefore, the liquid alloy flows through the nozzle as a continuous stream into the atomizing chamber below. The principle of gas atomization is simple: a continuous stream of liquid metal is broken down into droplets by a subsonic or supersonic gas stream or jet, the atomization occurs by kinetic energy transfer from the atomizing medium to the metal.

The number and geometry of gas/metal configurations are unlimited. Typical arrangements involving multiple jets or an annular ring are schematically illustrated in Figure 71 (details on jet configurations and design of atomizing units are available in the literature).

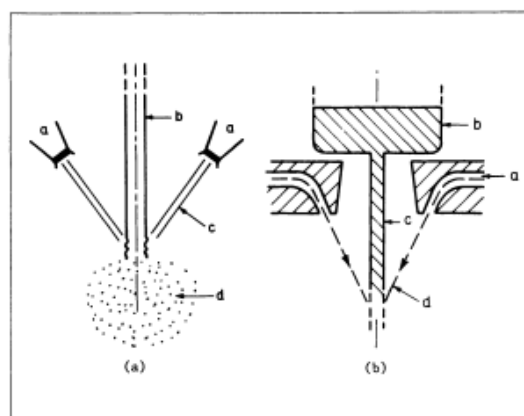


**Figure 71: Representative gas-atomization configurations [4]:**

- (a) Two-jet configuration:** a = jets, b = liquid metal stream, c = gas stream, d = atomized powder;
- (b) Annular-ring configuration:** a = ring orifice, b = liquid metal reservoir, c = liquid metal streams, d = gas stream

There are several interrelated processing and material variables involved in gas atomization (Table 8). As a consequence, numerous empirical relationships have been documented or proposed for predicting particle size and shape of several kind of alloys.

**Table 8: Variables in gas atomization**

Variables in gas atomization
Gas jet distance
Gas pressure
Gas velocity
Mass flow rate
Metal velocity
Mass flow rate
Angle of impingement
Superheat
Melting range
Surface tension

Air and nitrogen are commonly used to disintegrate the stream of molten metal in gas atomization. To minimize contamination of reactive molten alloys, argon is the preferred choice. Alternatively, helium provides an inert environment and increases also the cooling rate of the atomized droplets. Mixtures of gases can be selected to achieve desired powder characteristics at lowest cost. In particular, RINA CSM's VIGA plant (Figure 72) allows to obtain powders with very low oxygen content. It is also equipped with a "glove box" and a cyclone that allows both the handling and sieving of powders in inert atmosphere, in order to obtain the desired granulometric range.





**Figure 72: RINA CSM's VIGA plant**

In the first phase of powder production process, the master alloy, produced in the RINA CSM's VIM plant, is remelted in an induction furnace that is located in the upper part of the RINA CSM's VIGA plant (Figure 73). In this case, a crucible, which has a hole in its base, is used. During the remelting phase, the hole is closed by an alumina rod, that guarantees the seal of the crucible. When the metal charge is completely melted and it is characterized by the right atomization temperature, the rod is raised mechanically in order to obtain a fluid vein of metal that is constantly processed by an annular nozzle, using inert gas (in this case study it was used argon as process gas). As a result, micro-drops are obtained (Figure 74).


**Figure 73: Induction furnace of RINA CSM's VIGA**

**Figure 74: Atomization phase**

The powder obtained was sieved in the range 15 - 65  $\mu\text{m}$  and it was analyzed to extrapolate the data of interest. Process parameters, used for the gas atomization process, are shown in the following table.

**Table 9: Process parameters**

Alloy	Charge [kg]	T <sub>liquidus</sub> (°C)	T <sub>atom</sub> (°C)	Guide tube tip (mm)	P <sub>atom</sub> (bar)
AlSi <sub>7</sub> Mg	6,8	615	750	3	45

## POWDER CHARACTERIZATION

Powder characterization results, obtained with the defined process parameters, are shown below.

**Table 10: Powder characterization results**

Alloy	Atom.	G/M	Yield [15-65 $\mu\text{m}$ ]	D10 [ $\mu\text{m}$ ]	D50 [ $\mu\text{m}$ ]	D90 [ $\mu\text{m}$ ]
AlSi <sub>7</sub> Mg	Atom1	2,93	65	10,3	32,5	90,7

where: D(10), D(50), D(90) are the equivalent characteristic diameters, the yield is in AM range and G/M is the ratio obtained in atomization phase.

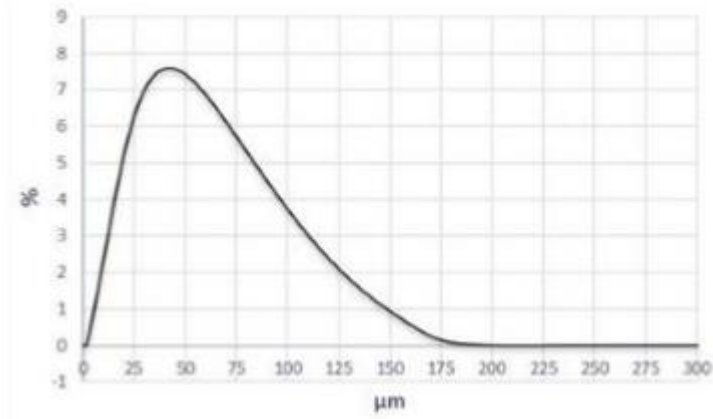


Figure 75: Particle Size Distribution

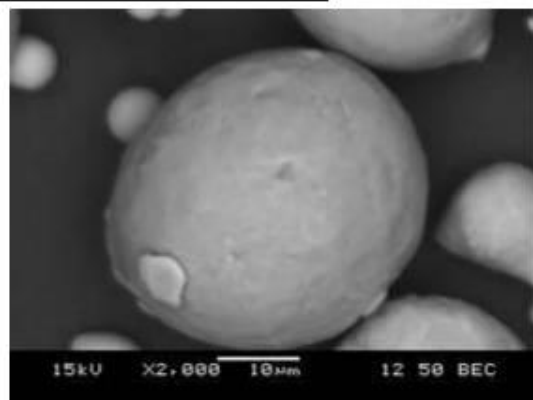
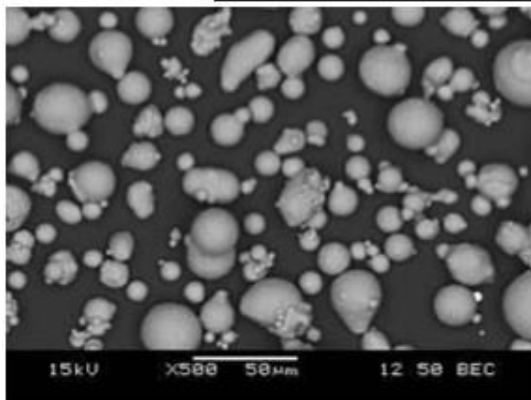
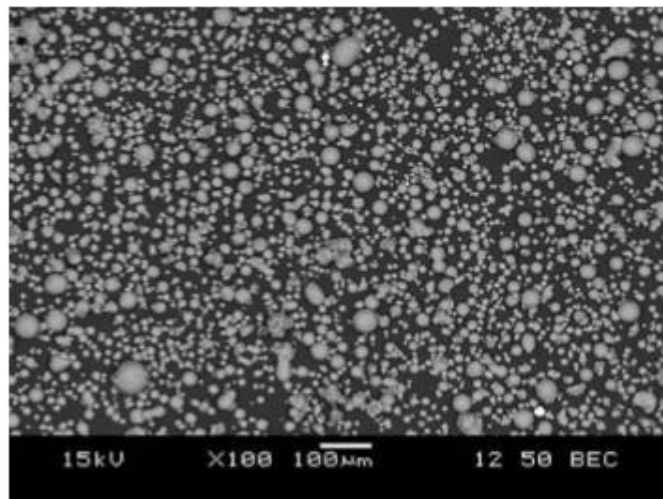


Figure 76: SEM images

## ODS POWDERS - DESIGN OF EXPERIMENT

In this phase of the project, definition of the ball milling parameters, ODS powder characterization and the evaluation of results have been performed.

### Ball milling parameters

After a bibliographic study it was decided to mix the  $AlSi_7Mg$  powder, with nanometer alumina particles characterized by a D(50) of 100 nm, using alumina spheres for imprinting them on it (Figure 77).



**Figure 77: Alumina sphere**

Eight different tests were performed, modulating only some of the process parameters and keeping the others fixed.

The process parameters analysed are reported below:

- Percentage by weight of dispersoids
- Process time
- Sphere/powder weight ratio

In Table 11 the process parameters used for the several tests are shown.

**Table 11: Ball Milling Process Parameters**

	Dispersoids (%wt)	Process time (min.)	Sphere/powder weight ratio
Test 1	0,5	30	1:1
Test 2	0,5	60	1:1
Test3	0,5	90	1:1
Test 4	1	30	1:1
Test 5	1	60	1:1
Test 6	1	90	1:1
Test 7	1	60	2:1
Test 8	1	60	5:1

### Mixing powder

The powders were mixed by keeping the angular speed of the miller constant at 120 rpm, with alumina balls characterized by a diameter of about 20 mm, in an inert control volume of about 10 L.

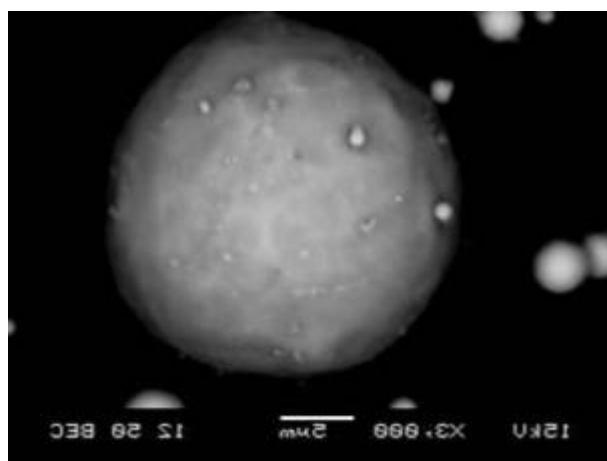
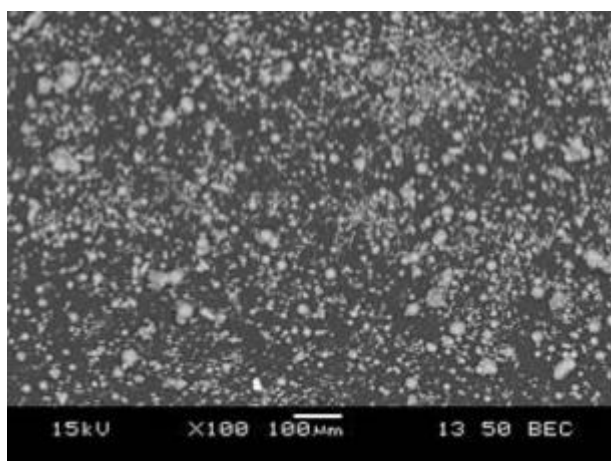


Figure 78: RINA CSM Miller

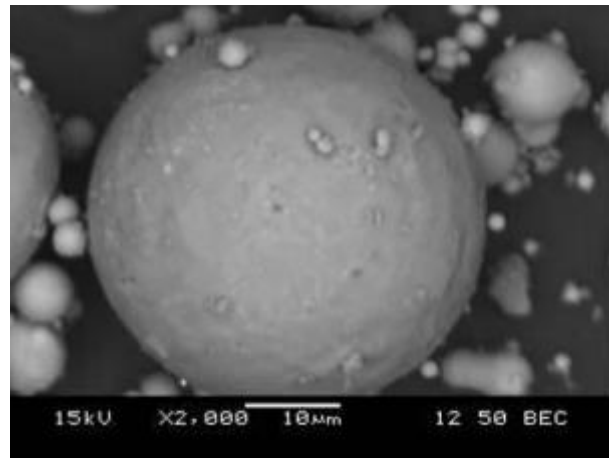
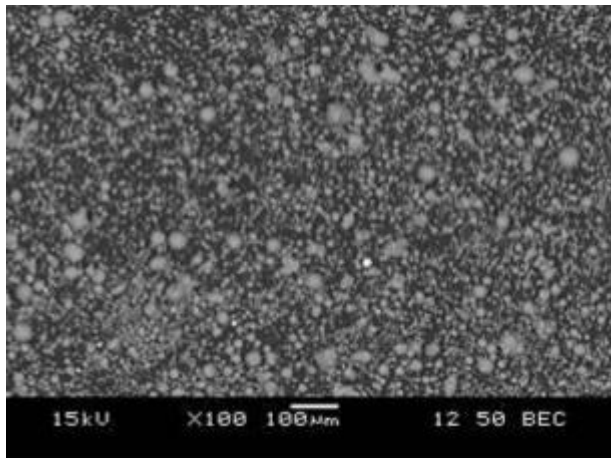
In the first three tests, which were carried out by modulating the process time, no satisfactory results were obtained in terms of imprinting. In addition, in the third test some aluminium particles are deformed.

SEM images are reported below.

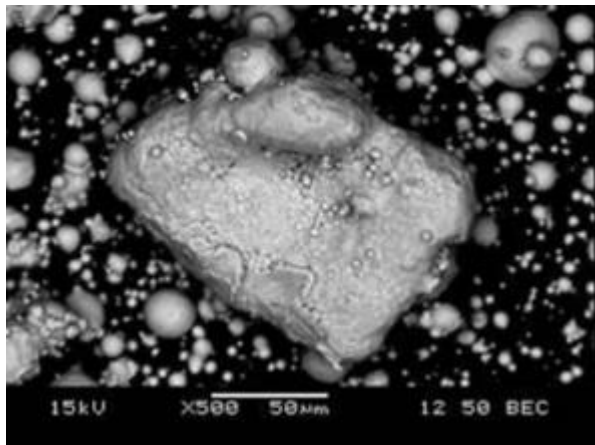
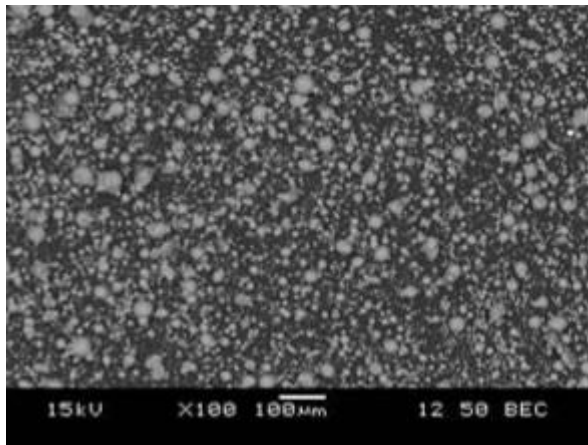
#### Test 1



Test 2

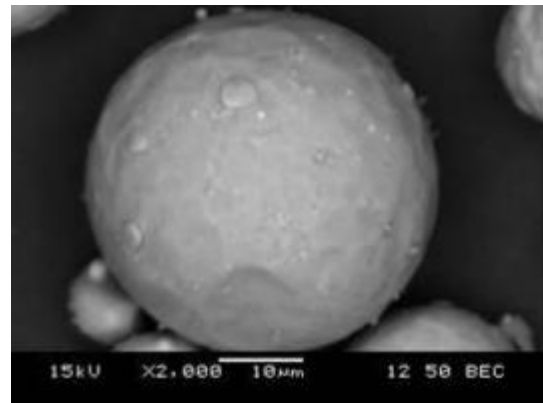
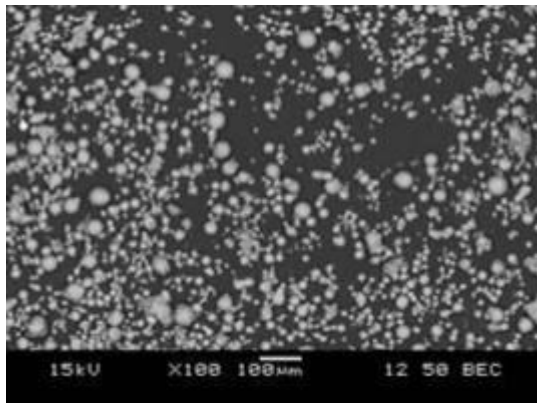


Test 3

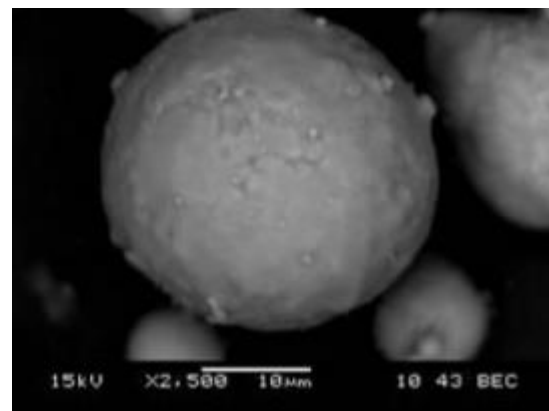
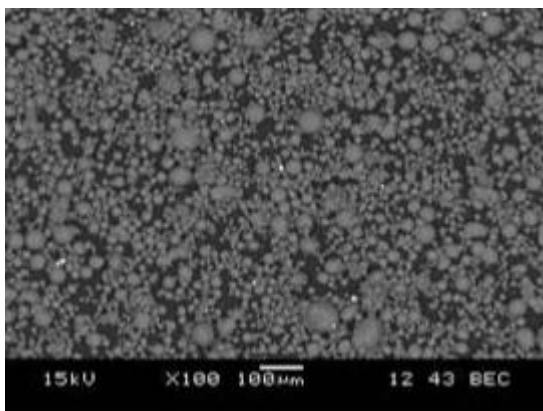


In the 4<sup>th</sup>, 5<sup>th</sup>, 6<sup>th</sup> tests the percentage by weight of dispersoids was increased to 1% and the process time was modulated as in the three previous trials. In this case a slight coating of the aluminium particles can be seen. In addition, in the 6<sup>th</sup> test, which is characterized by a process time of 90 mins, deformed particles are obtained again.

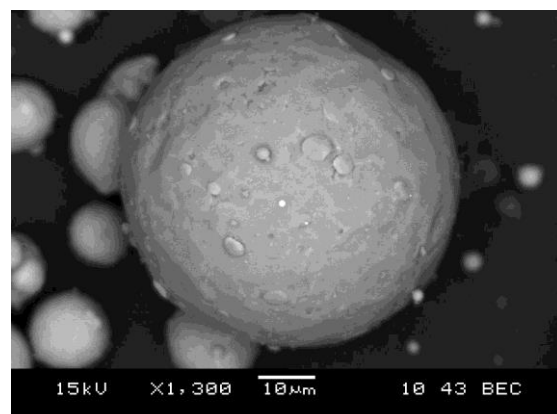
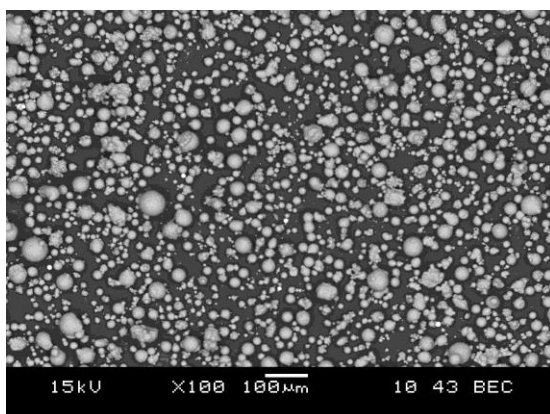
Test 4



Test 5

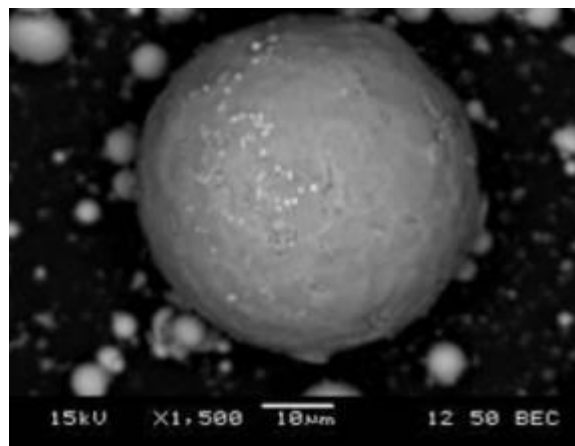
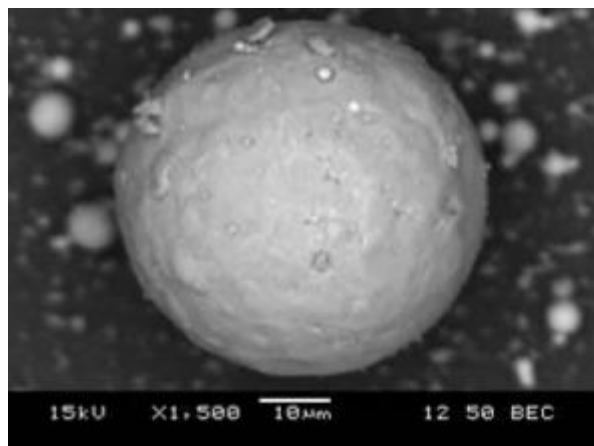


Test 6



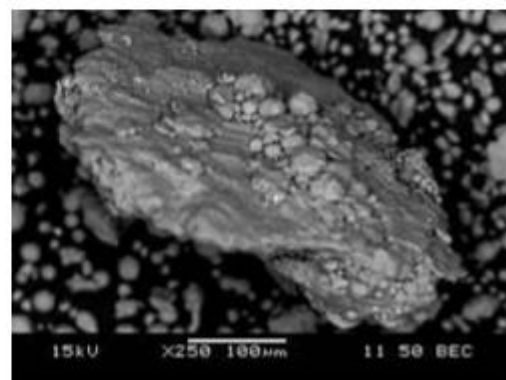
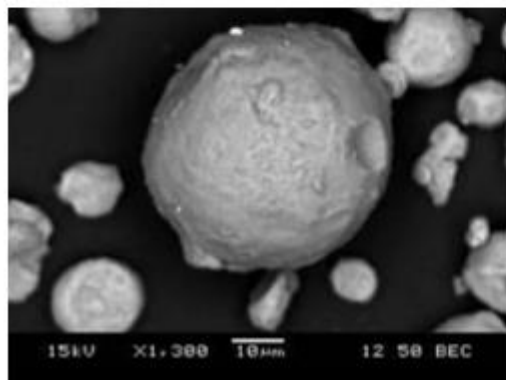
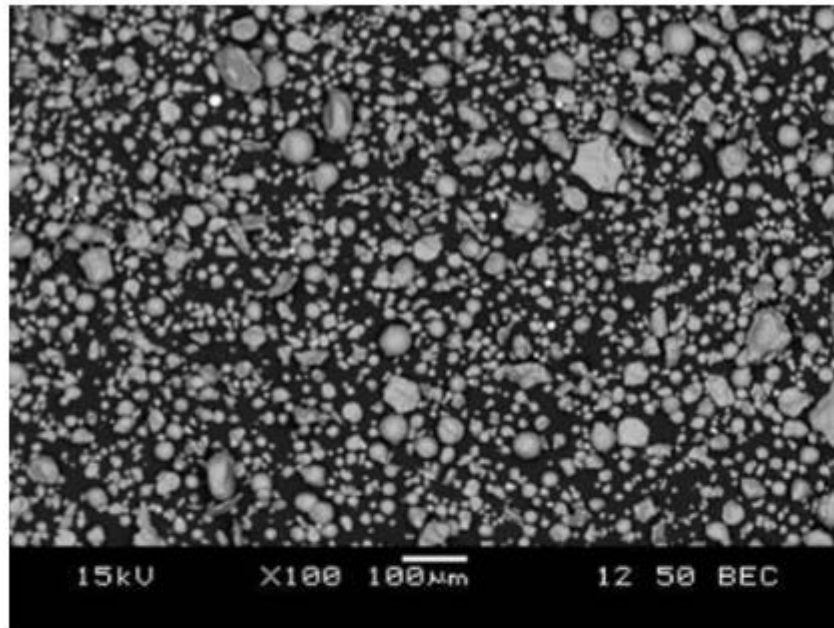
Considering the previous results, the 7<sup>th</sup> test was performed by fixing the process time to 60 minutes with a dispersoid percentage by weight of 1%. Furthermore, Sphere/Powder weight ratio was increased up to 2:1. In this case a considerable increase in the alumina particles embedded on the aluminium powder has been obtained.

**Test 7**



In the last test, the Ball/Powder weight ratio was increased in comparison to the previous tests. However, in this case a large percentage of particles lost their sphericity condition.

Test 8



From the image analyses, the best result, in terms of alumina particle coating, was obtained in the 7<sup>th</sup> test. Such ODS powder was selected to be processed in SLM, in order to make samples for microstructural analyses, hardness and tribological tests.

## 5. SELECTIVE LASER MELTING SAMPLES PRODUCTION

Novel materials for use in SLM require the study of process parameters in order to ensure desirable material properties. One of the key material properties is the part density achieved during the process. SLM relies on the melting of metallic powders by the fast scanning of a high-brilliance laser beam. During the melting process the energetic conditions should be adequate to avoid pore formation. Commonly pore formation occurs due to lack of fusion at low energy density conditions and keyhole formation and vapour entrapment at excessive energy densities.

Concerning ODS materials, the pore formation can be due to the lack of wettability between the melt pool and the oxides. Accordingly, a parameter study has been carried out to assess the processability of the novel material.

The powder used in the experiment is the AlSi7Mg0,6 + Al<sub>2</sub>O<sub>3</sub> (Figure79).

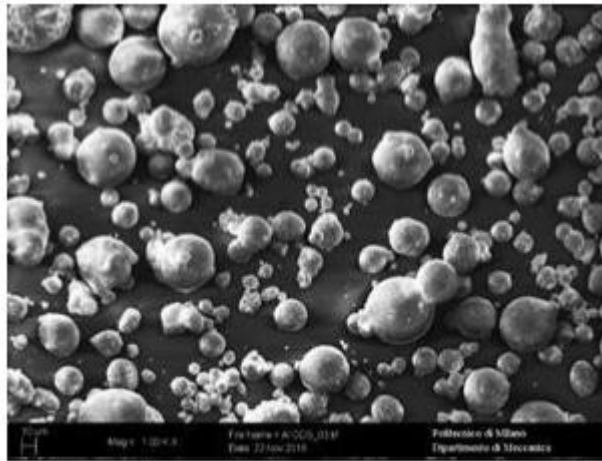


Figure 79. The powder used in the experiment are observed with SEM

### SLM system

Renishaw AM250 was used throughout the experimental work (Stone, UK). The system implemented a 200 W active fiber laser (R4 from SPI, Southampton, UK). The optical chain was composed of a galvanometric scanner with integrated z-axis positioner, which enabled to control the focal position of the beam. In this configuration the estimated beam diameter is 75  $\mu\text{m}$ . The build space was 250x250x300 mm<sup>3</sup> (WxDxH). Prior to processing, vacuum is applied to the processing chamber down to -950 mbar pressure and then it is flooded with Ar reaching 15 mbar overpressure. Throughout the process, a circulation pump maintains the gas flow parallel to the powder bed and the oxygen content of the process chamber is maintained below 1000 ppm. For material development, the system is fitted with a reduced build volume (RBV) kit that allows for operating in a smaller volume with a limited amount of powder.



Figure 80 : Reinshaw AM250 SLM Machine

### Reduced Build Volume System

The Reduced Build Volume (RBV) is designed for users who wish to easily change between materials for the purpose of materials development and experimentation. RBV enables rapid real time testing of the parameters, speeding up material development iterations. After the initial configuration of the RBV, it is quick and easy to install and remove by the user. It is completely self-contained and can be used with as little as 0.25 L of material. Once the RBV is removed the machine functions as a normal full size additive manufacturing system. RBV allows operating with lesser volumes of powder thus saving time and sample.

Table 12. RBV platform dimensions

Maximum Build Dimensions(HxWxD)	55mmx78mmx78mm
Build Volume Dimensions(HxWxD)	64mmx80mmx80mm





Figure 81 :RBV parts details and SLM of samples on RBV platform

### Process parameters involved in SLM

The SLM system employed the PW emission. In particular, the laser is positioned on a certain spot to emit with a given peak power ( $P_{peak}$ ) for a fixed exposure time ( $t_{on}$ ) in  $\mu s$  range. The laser jumps onto the consecutive spot on the scanned line and applies the exposure. At the end of each scanned line, the laser jumps to the adjacent one. The operation is continued until the layer is scanned completely. For a given layer, the system applies different hatch lines for the part volume and part external border, which use different parameter sets. Beam compensation can be applied by placing the external border inward with respect to the design geometry defined by the STL border.

Five principal process parameters have been identified for the study. The laser power ( $P$ ) controls the pulse peak power ( $P_{peak}$ ). Pulses are generated by power modulation with a shape very close to a square wave. Hence, the emission profile does not vary throughout the pulse duration, i.e.  $P(t)=P_{peak}$ . Exposure time controls the duration of the laser pulse applied to each spot on the scanned line and corresponds to  $t_{on}$ . The minimum exposure time that can be employed is  $20 \mu s$ . The focal position ( $f$ ) controls the position of the beam focal point with respect to the powder bed surface. For the present system, negative focal position values refer to a laser spot focused above the powder bed surface, and positive values refer to the focal point below the powder bed surface. The focal position controls the spot size ( $d_s$ ) on the powder surface and in either case the beam size enlarges moving away from the focal position. Point distance ( $d_p$ ) and hatch distance ( $d_h$ ) are the other parameters that were varied.

Energy density is an aggregate parameter, which is commonly used in the literature to compare the processing conditions between different materials and machines. Energy density for PW emission can be calculated using the following expression.

$$E = \frac{Pt_{on}}{d_p d_h z}$$

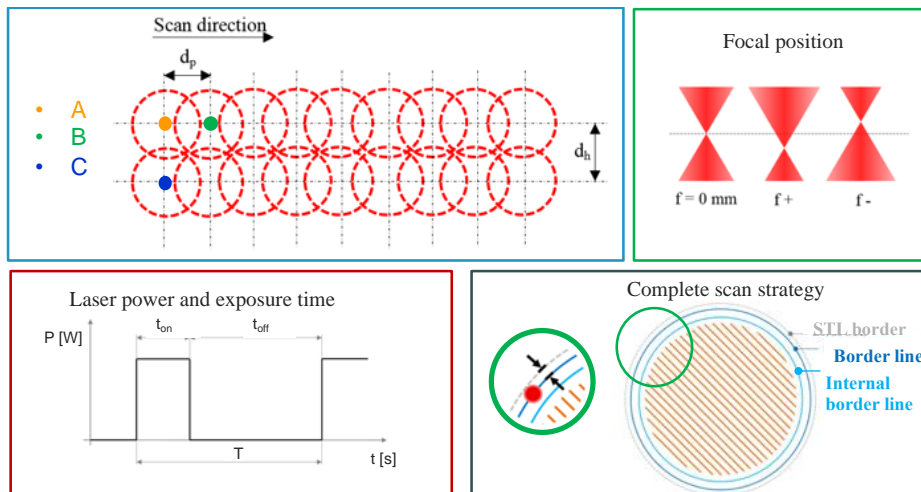


Figure 82: Process parameters involved in SLM.

### Mitutoyo Quick-Vision Active 202-Pro5f Microscope

The samples are placed on the platform of the microscope for taking surface photos. After adjusting the magnification and light, the photos are taken by indicating reference points around each cube sample by using a software. Then the cube surfaces on the pictures are constrained by drawing lines on its circumference as to not count defects caused by SLM or polishing into account for porosity measurement.

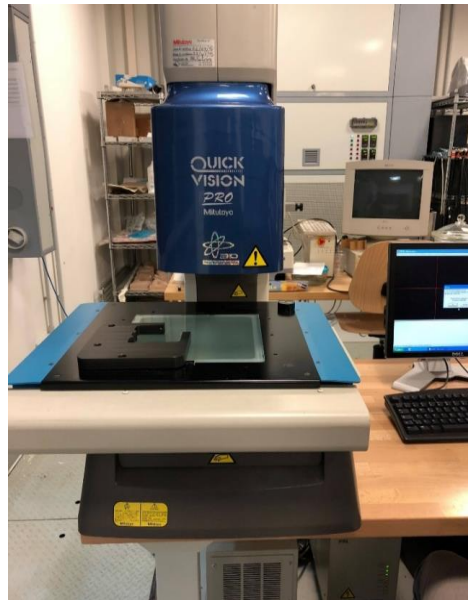


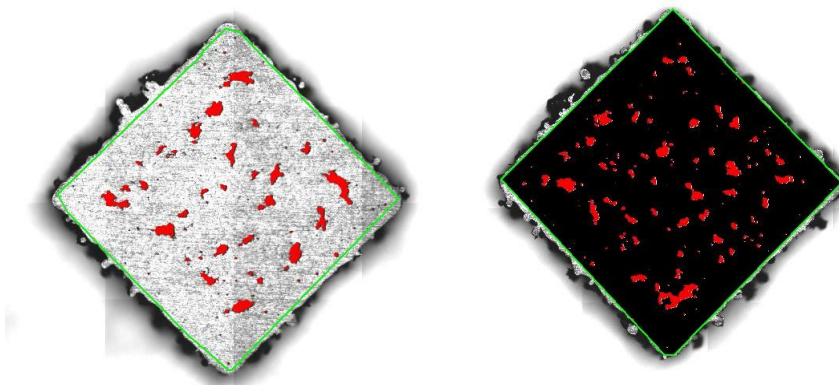
Figure 83: Mitutoyo Quick-Vision Active 202-Pro5f Microscope



### Experimental design

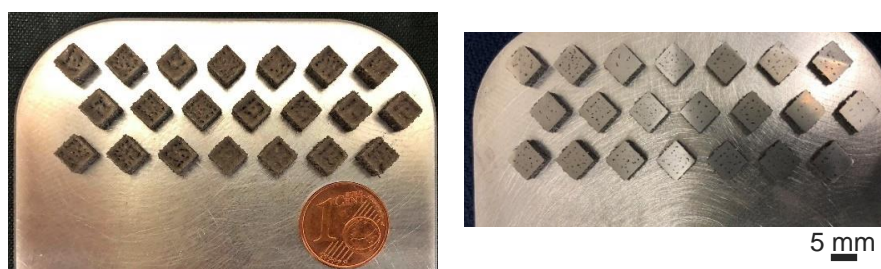
After SLM, samples are cleaned and polished, changing the polishing papers (from 180 to 320, 600, 800 and finally 1200 roughness value - a higher number meaning a smaller roughness). A cooling water is kept on during polishing in order to prevent unwanted defects. Cross-section images were taken over the whole specimen. The density was measured employing image processing software with the following expression:

$$D = \frac{A_{tot} - A_{pore}}{A_{tot}}$$



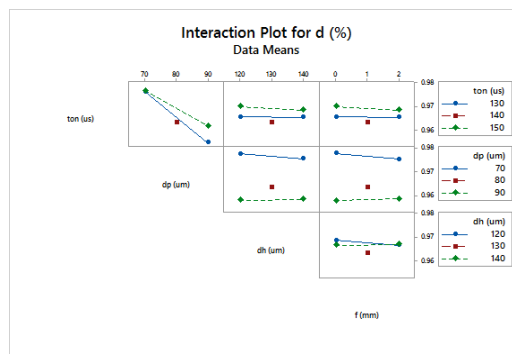
**Figure 84: Examples of porosity as contrasting colour ranges in the indicated area, the porosity is then measured using the software as ratio to the indicated area**

Figure 85 shows the produced specimens for mechanical characterisation. It can be seen that the novel material could be successfully used for producing freestanding samples. The main effects and interaction plots as a function of the employed process parameters are shown in Figure 86. It can be noticed that the overall density results are between 95 and 98%. Although the results confirm a first feasibility of the employed material, the density conditions should be improved for adequate mechanical properties.



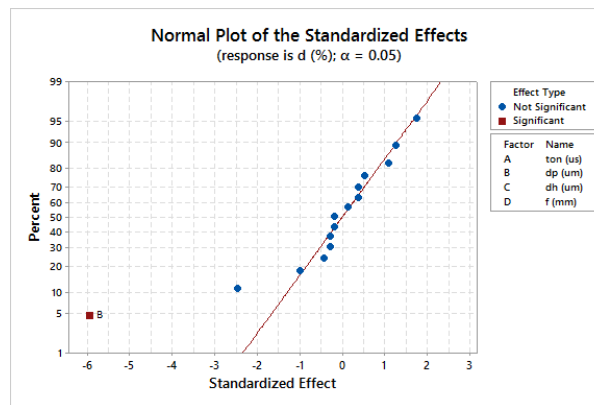
**Figure 85: Macro images of the samples after SLM and after polishing**





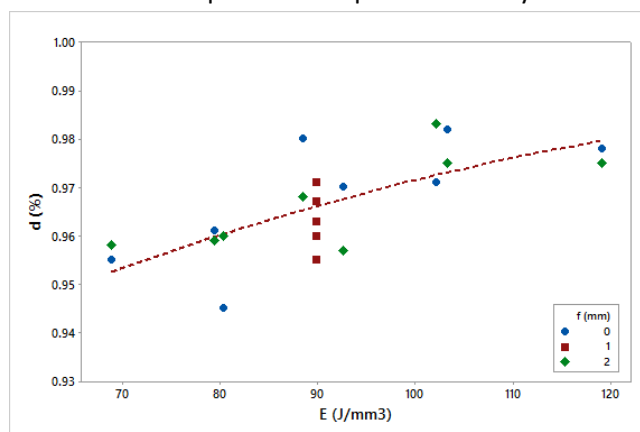
**Figure 86 : Main effects and interaction plots for part density**

Figure 87 shows the normal plot of the standardized effects. The plot shows that the only statistically significant parameter, in the tested conditions, is the point distance. Evidently, a shorter point distance can be advantageous for improving the density.



**Figure 87 : Normal plot of the standardized effects.**

Figure 88 shows the density behaviour as a function of energy density parameter. It can be seen that an asymptotic increase is present. The behaviour is comparable to what is observed with conventional SLM materials. However, further studies are required for improved density.



**Figure 88 :Part density as a function of energy density.**



Besides samples for mechanical characterisation, cylindrical samples were produced for pin-on-disc tests by SLM. The samples were oversized with respect to the final pin dimensions with machining allowance. The samples had 6.5 mm diameter and 44 mm length (the final pin dimensions are 5mm for the diameter 32 mm for the length). The samples were built placing the cylindrical axis along the build direction and hence avoiding the use of support structures. Pins were produced using AlSi7Mg0.6 + 1wt% Al<sub>2</sub>O<sub>3</sub> powder as well as AlSi7Mg0.6 for a comparative analysis.

Samples were produced using the process parameters as expressed in Table 13. Energy density was varied in order to assess the influence of process parameters on the part density and wear performance. Six replications were executed for each condition.

Figure 89 shows the produced samples and the powder bed during the SLM process. It can be seen that macro defects could be avoided with AlSi7Mg0.6 and the powder bed remained highly stable during the process. During the production of AlSi7Mg0.6 + 1wt% Al<sub>2</sub>O<sub>3</sub> samples, 2 replications of Set 2 and Set 3 were aborted due to bad powder flow. A minimum of 4 replications could be produced for each condition. The experiments indicated that the powder grain size can be further improved for the SLM process to ensure better flowability. Once flowability is improved, the processability of AlSi7Mg0.6 + 1wt% Al<sub>2</sub>O<sub>3</sub> is expected to be also enhanced.

**Table 13: Process parameters used to produce pins**

Set	P (W)	z (um)	t (us)	dp (um)	dh (um)	E (J/mm <sup>3</sup> )
1	200	30	150	70	120	119
2	200	30	150	70	105	136
3	200	30	150	55	120	152

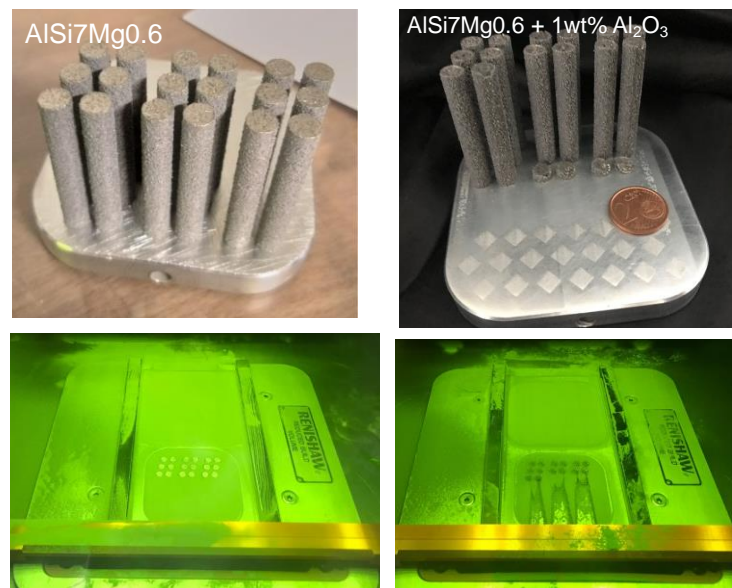
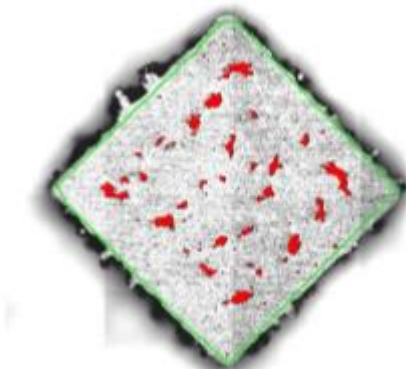


**Figure 89: Production of pins for tribological tests**

## Mechanical Characterization

After the 3D printing process, specimens, which are built up step by step, are welded to the aluminium working plate. They were removed by wire EDM.

The first analysis was the measurement of the surface porosity. It has been carried out by means of an image analysis software, which measures the voids as a percentage of the ideal surface. The obtained porosity is a frequent defect for samples made by SLM. One of the analysed specimens is shown below whereas the several results are reported in the table.



Sample no	Dmean
1	0,971
2	0,945
3	0,978
4	0,958
5	0,968
6	0,967
7	0,970
8	0,975
9	0,955
10	0,955
11	0,975
12	0,960
13	0,983
14	0,982
15	0,960
16	0,961
17	0,963
18	0,959
19	0,957
20	0,980
21	0,971

About 2% of porosity was achieved in the worst condition. The analysis made it possible to select samples at different density conditions (such as samples characterized by maximum, minimum or intermediate density were chosen). Hereafter, the samples were chosen as:

Sample no	Density
1	0,971
2	0,945
13	0,983
17	0,963
18	0,959

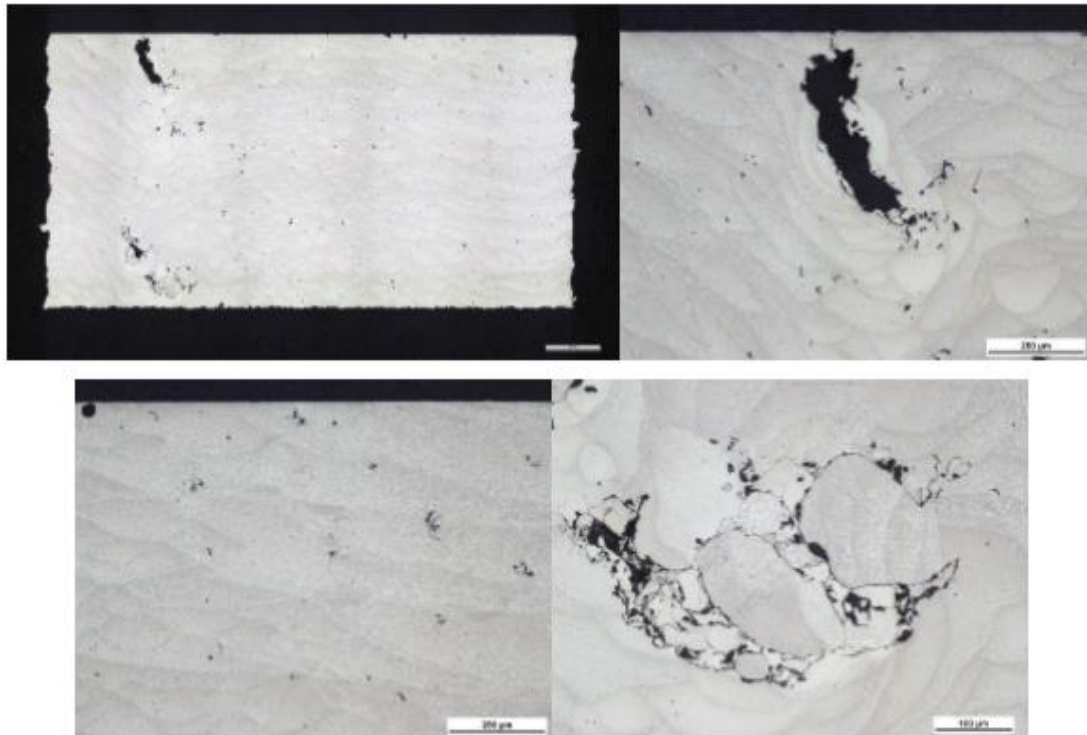
The results of the indentation tests on SLM samples are shown below.

	HV_5		D1		D2	
	Media	Dev.St	Media	Dev.St	Media	Dev.St
<b>1</b>	94,7	7,0	309,3	11,2	314,3	12,0
<b>2</b>	101,0	1,0	298,7	2,1	305,0	1,7
<b>13</b>	96,3	6,0	305,0	9,2	313,3	9,5
<b>17</b>	102,7	5,5	297,3	7,5	301,3	8,1
<b>18</b>	96,7	4,9	307,7	9,0	309,3	9,3

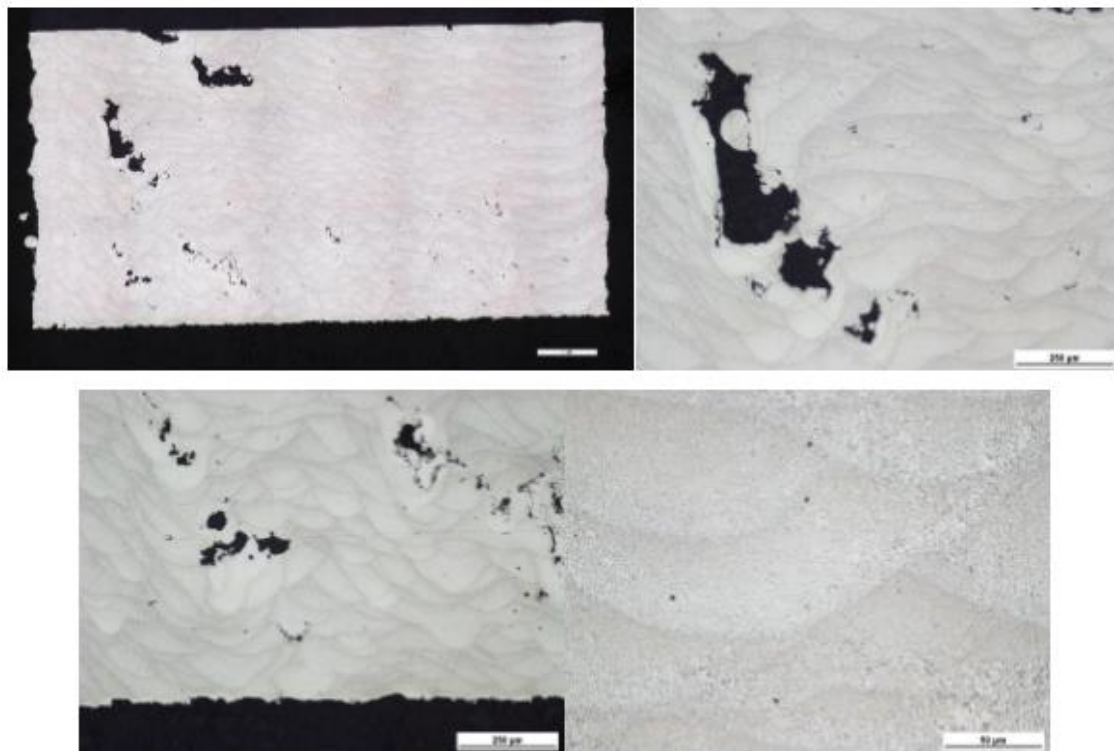
Hardness is about HV=98: this result is comparable with past characterizations performed on SLM samples of AlSi7Mg alloy without dispersoids ( $102 \pm 2$ ). Probably this result was due to a large number of porosities of the samples rather than the lack of reinforcement.

Moreover, the samples were cut perpendicularly to the printing direction for metallographic characterizations (porosity and cracks). Below, the images acquired during this analysis.

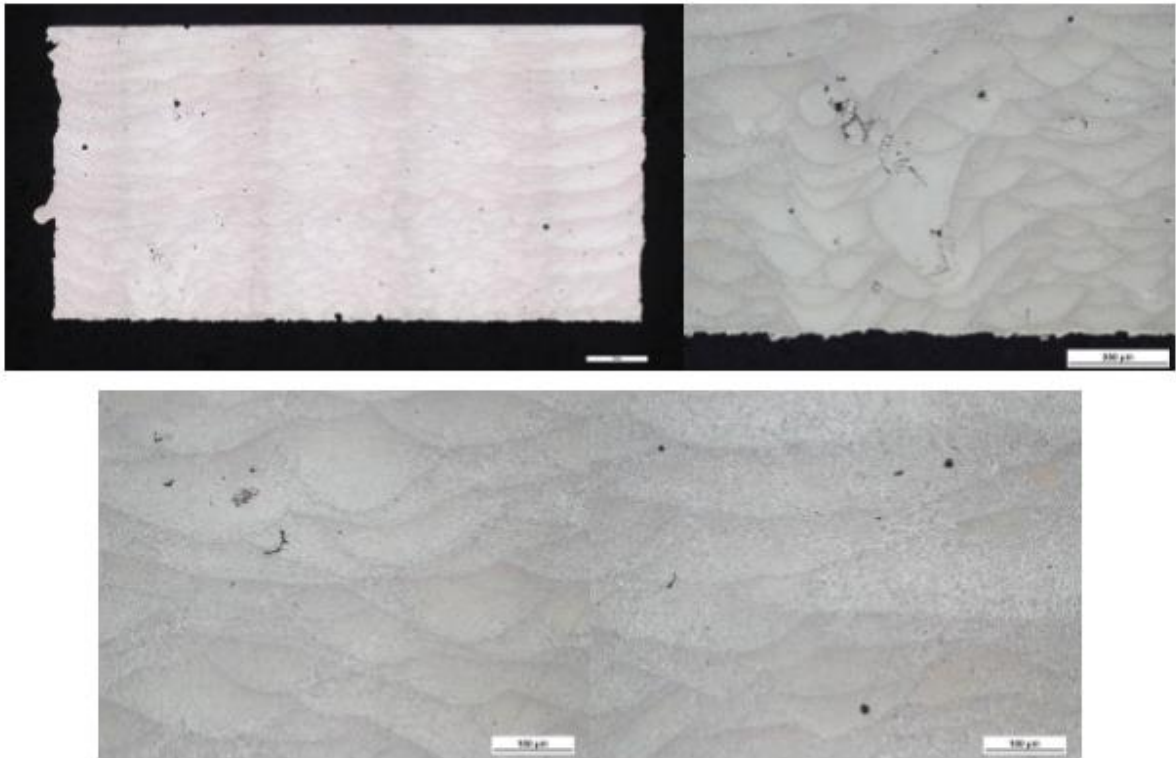
Sample 1



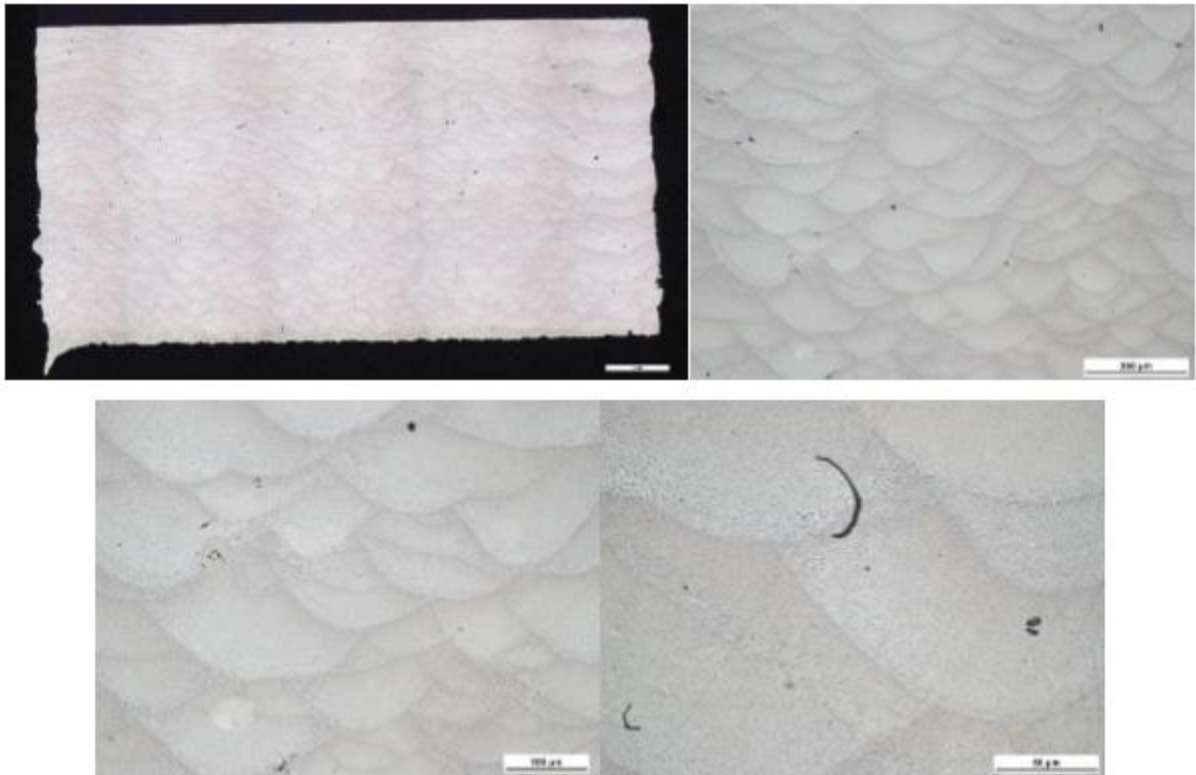
Sample 2



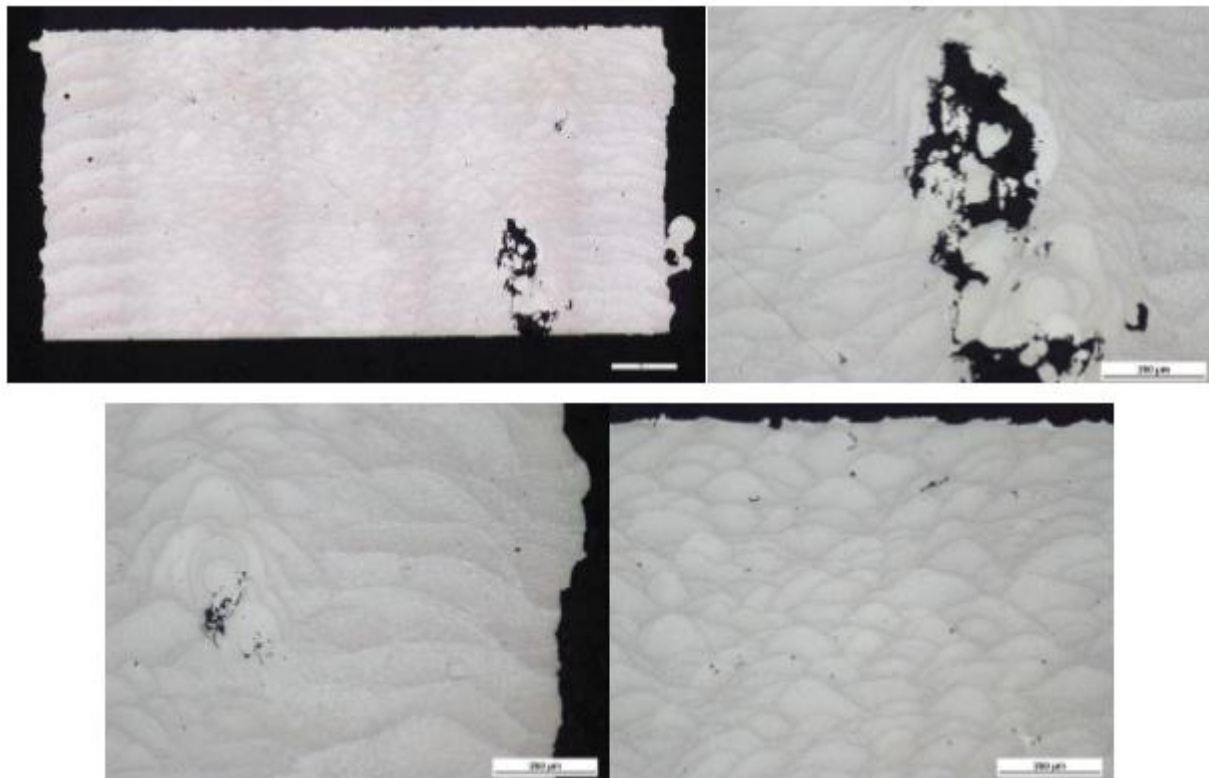
Sample 13



Sample 17



Sample 18



The optical microscope image analysis showed that the process parameters, used for samples 13 and 17, are the most suitable. Even if no cracks caused by mechanical stress have been observed, a large number of defects were detected: these defects were caused by unmelted particles.

As well known, the presence of oxides on the powder surface can cause weldability problems and gas porosity. Therefore, it was necessary to understand if this effect was caused by oxides for making the ODS alloy. SEM - EDS analyses were accomplished (see below the photos of the EDS results).

Photo 1

Spectrum	In stats.	O	Al	Si	Total
Spectrum 1	Yes	49.97	50.03		100.00
Spectrum 2	Yes	13.74	77.78	8.48	100.00

Photo 2

Spectrum	In stats.	O	Al	Si	Total
Spectrum 1	Yes	1.59	94.74	3.67	100.00
Spectrum 2	Yes	1.71	89.84	8.45	100.00
Spectrum 3	Yes	1.61	90.82	7.57	100.00
Spectrum 4	Yes	2.51	93.42	4.07	100.00
Spectrum 5	Yes	1.69	88.50	9.81	100.00

Photo 3

Spectrum	In stats.	O	Al	Total
Spectrum 1	Yes	50.62	49.38	100.00
Spectrum 2	Yes	50.43	49.57	100.00
Spectrum 3	Yes	50.12	49.88	100.00

Photo 4

Spectrum	In stats.	O	Mg	Al	Si	Total
Spectrum 1	Yes	49.06	0.78	50.16		100.00
Spectrum 2	Yes	49.65		50.35		100.00
Spectrum 3	Yes	49.77	2.31	47.92		100.00
Spectrum 4	Yes	6.07		84.14	9.79	100.00

Photo 5

Spectrum	In stats.	O	Al	Si	Total
Spectrum 1	Yes	50.05	49.95		100.00
Spectrum 2	Yes	43.47	55.24	1.28	100.00

EDS investigations showed a high percentage of aluminum and oxygen inside the porosity, while the rest of the metal matrix was composed by aluminum, silicon and magnesium.

Probably, the observed porosity was caused by aggregation of nano-dispersoids of alumina during the ball milling process.

### Tribological characterization

Pin-on-Disc tests were carried out to investigate the tribological properties of the ODS specimens (ODS S1). The results were compared with the specimens made by AlSi<sub>7</sub>Mg powder without dispersoids (A357). All the specimens were realized using the same technology (SLM).

Pin-on-Disc tests were carried out in accordance with the ASTM G99-04 "Standard Test Method for Wear Testing with a Pin-On-Disk Apparatus" using the parameters reported in Table 14.

**Table 14: Pin-On-Disk Parameters**

Sample Geometry	Cylindrical pin
Dimensions	Diameter = 5 mm, Length = 32 mm
Counterparts	Ti64 Disk WC-Co Coated, Diameter = 40 mm
Wear track radius (mm)	16
Relative sliding speed (m/s)	4
Distance (m)	5000
Load (N)	6

Archimede method was used to evaluate the density for every sample in a Mettler Toledo AX504DR balances: results are listed in Table 15 and Table 16.

**Table 15: A357 S1 Density**

Samples	$\rho$ material
	g/cm <sup>3</sup>
A357 S1 (A)	2.70
A357 S1 (B)	2.69
Average value	2.70

**Table 16: ODS S1 Density**

Samples	$\rho$ material
	g/cm <sup>3</sup>
ODS S1 (A)	2.58
ODS S1 (B)	2.52
Average value	2.55

Results of the Pin-on-Disk tests are listed in Table 17, Table 18 and in Figure 90, Figure 91, Figure 92, Figure 93, Figure 94 and Figure 95.

**Table 17: A357 S1 PoD test results**

A357 S1	Test 1	Test 2	Test 3	Test 4	Average	Standard Deviation
Mass Loss (g)	-0.0042	-0.0017	-0.0040	-0.0036	-0.0034	0.0010
$\Delta L$ (mm)	-0.09	-0.03	-0.16	-0.08	-0.09	0.05
CoF	0.25	0.23	0.26	0.25	0.25	0.01



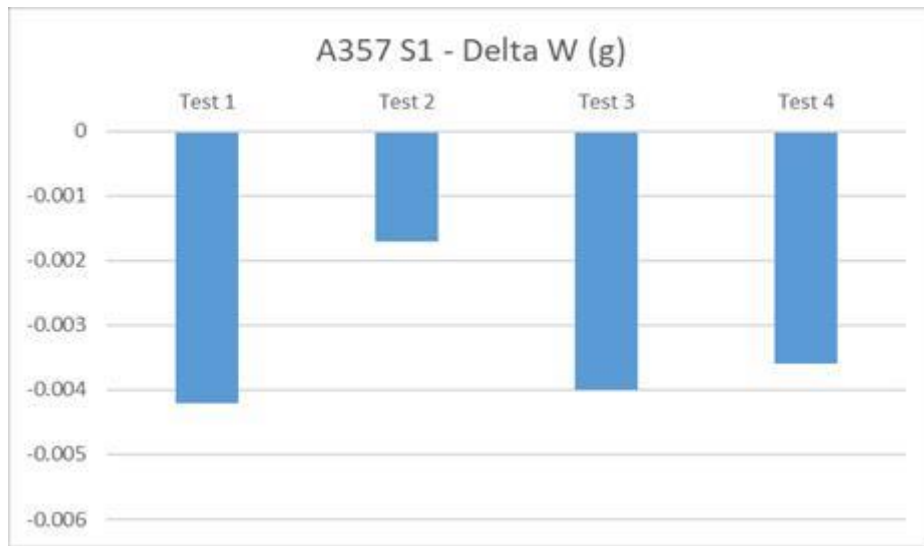


Figure 90: A357 S1 Mass lost after PoD test

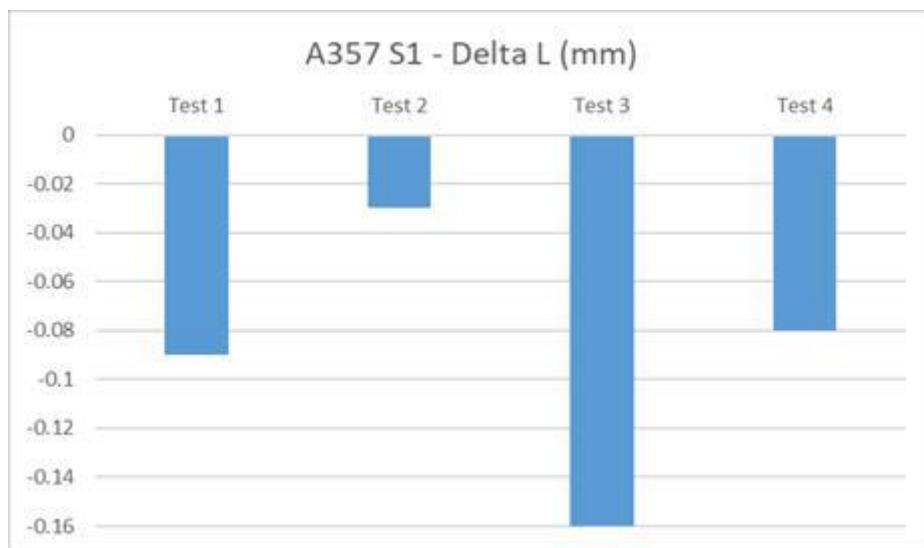


Figure 91: A357 S1 Pin shortening after PoD test



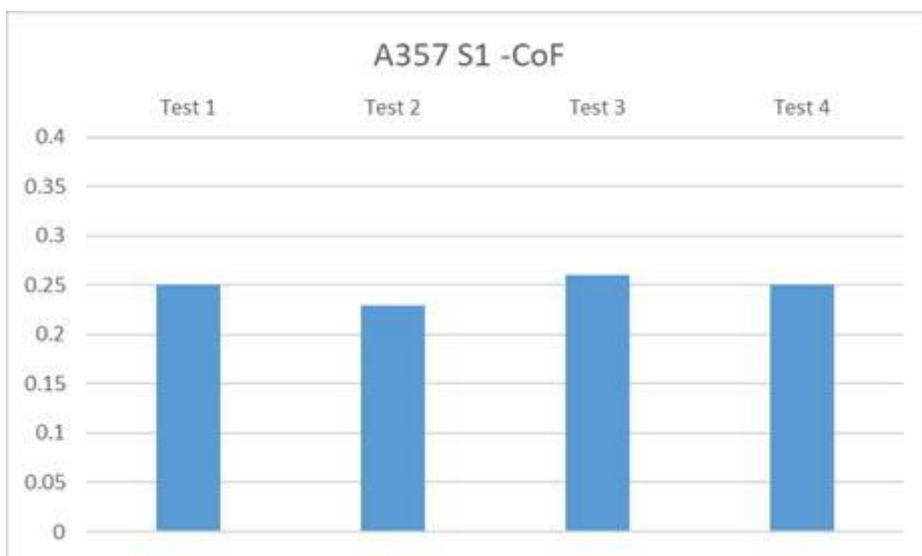


Figure 92: Average Coefficient of Friction measured during PoD test

Table 18: ODS S1 PoD test results

ODS S1	Test 1	Test 2	Test 3	Test 4	Average	Standard Deviation
Mass Loss (g)	-0.0051	-0.0024	-0.0040	-0.0039	-0.0039	0.0009
$\Delta L$ (mm)	-0.10	-0.06	-0.11	-0.08	-0.09	0.02
CoF	0.26	0.22	0.27	0.38	0.28	0.06

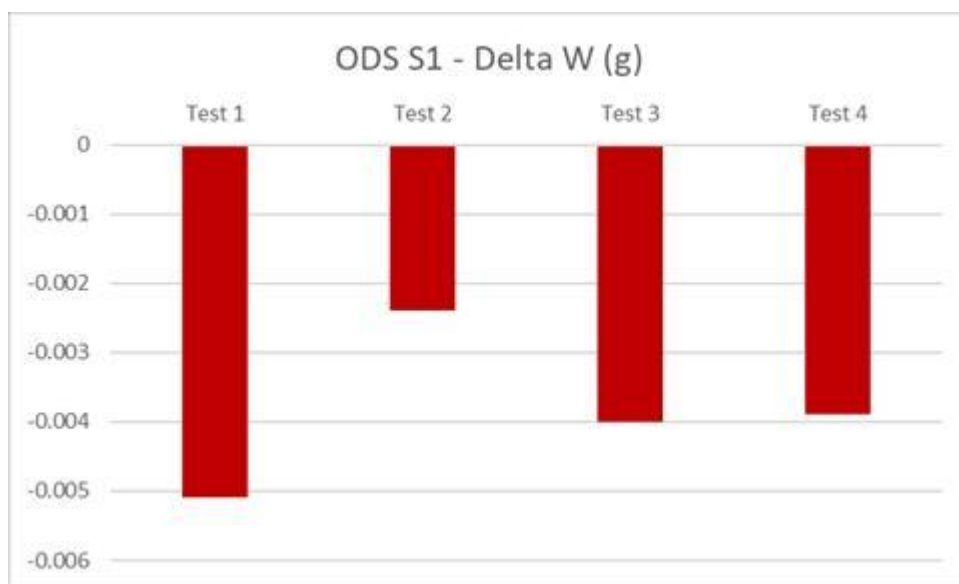


Figure 93: ODS S1 Mass lost after PoD test



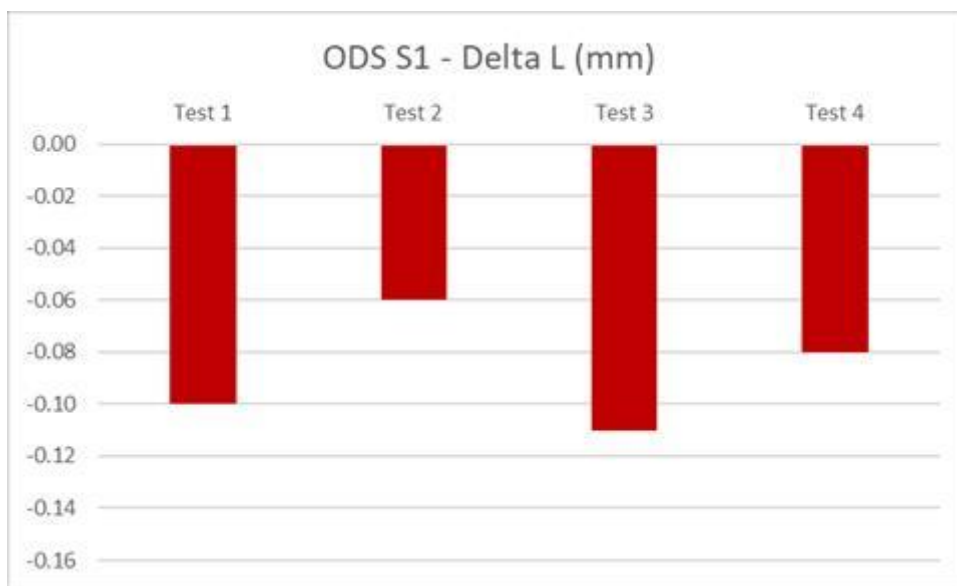


Figure 94: Pin shortening after PoD test

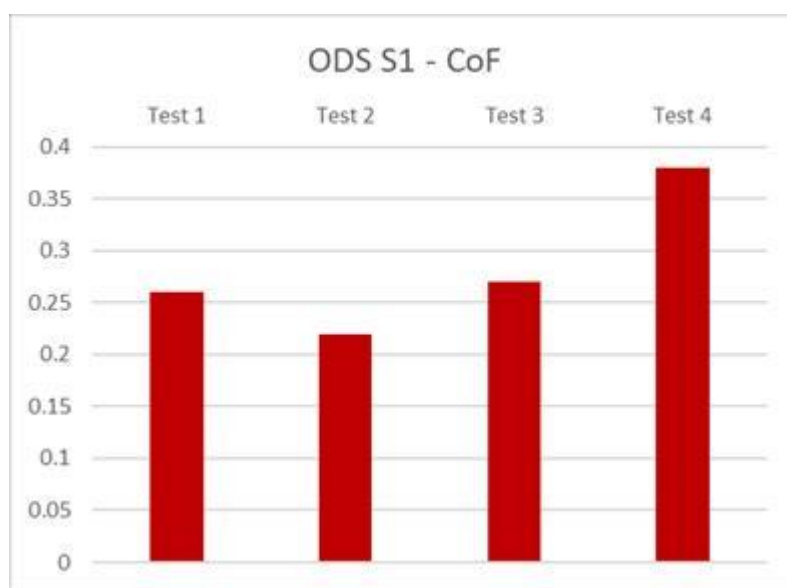


Figure 95: Average Coefficient of Friction measured during PoD test

The tribological behaviour of both A357 S1 and ODS S1 samples is comparable, no significant differences were measured in average CoF and wear rate values.

Although is important to make comparison in the same tribological conditions (counterpart material, sliding speed, distance, load etc.), a preliminary comparison with other results from bibliographic research was made.

To compare the results with the literature ones, the average wear loss of A357 S1 and ODS S1 samples was calculated using the average density, previously measured.



**Table 19: Average wear loss and CoF**

Pin	Average wear loss (mm <sup>3</sup> /m)	Average CoF
A357 S1	2.50E-04	0.25
ODS S1	3.02E-04	0.28

S. Khan used a Pin-on-disc wear test to study tribological behaviour of Aluminum Cast Alloy A356 [25]. The tests had a maximum sliding distance of 5000m under varying load up to 8 Kg in steps of 0.5 Kg. The pin used was cylindrical (8mm diameter and 40 mm length) and prepared from composite casting. It was loaded through a vertical specimen holder against horizontal rotating EN32 disc of steel with hardness 65 HRC and diameter 50 mm. Comparison of wear rate, in similar load condition, is shown in Table 20.

**Table 20: Wear loss comparison with S. Khan [25]**

Pin	Average wear loss (mm <sup>3</sup> /m)
A357 S1	2.50E-04
ODS S1	3.02E-04
Aluminum Cast Alloy A356	1.0E-03

M. Lorusso studied the tribological behaviour of AlSi10Mg Casting and AlSi10Mg DMLS using a pin-on-disk tests [26]. A constant load of 5 N and a constant velocity of 0.2 m/s, for a sliding distance of 500 m were used as parameters. Tests were conducted at room temperature and in dry condition. The used counterpart was a WC-Co pin characterized by a spherical 3 mm radius tip. Although different conditions were used in this test respect to the A357 S1 and ODS S1 tests, comparison results of wear rate is shown in Table 21.

**Table 21: Wear loss comparison with M. Lorusso [26]**

Pin	Average wear loss (mm <sup>3</sup> /m)
A357 S1	2.50E-04
ODS S1	3.02E-04
AlSi10Mg Casting	1.4E-02
AlSi10Mg DMLS	9E-03

Figure 96 shows the CoF trend during the AlSi10Mg Casting and DMLS PoD test. CoF is higher than the CoF measured during A357 S1 and ODS S1 tests (Table 19).

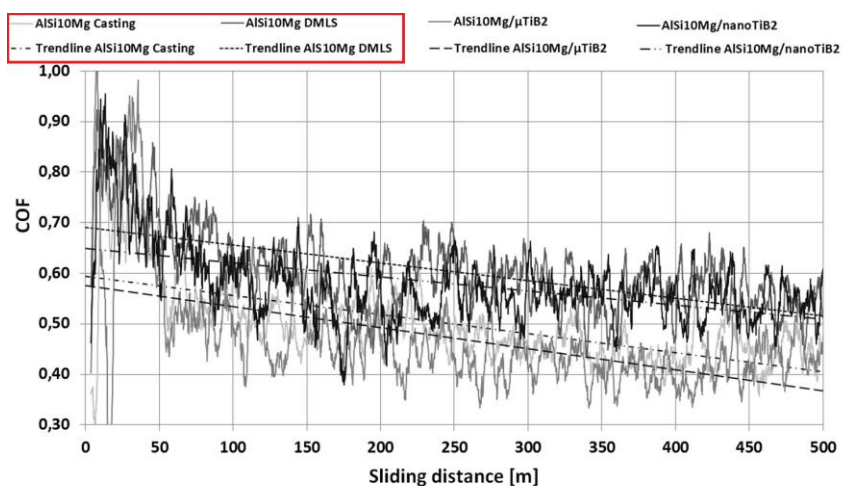


Figure 96: CoF results from M. Lorusso [26]

The comparison between the tribological behavior of literature data and both A357 S1 and ODS S1 samples showed a set of promising results. Wear loss is in the same range and also CoF is almost similar.

## 6. FDM AND ADHESION MODEL

At present, Automated Fiber Placement technique (together with the Automated Tape-Laying technique that, however, requires much more expensive starting material, i.e. tapes, and is definitely less flexible) is the only approach to automatically produce complex structures using CFRC. By complex structures we mean 3D geometries having double curvature profiles. The automation of the process is of fundamental importance to have high quality standards in the final component. The use of a robot having at least 6 dofs is mandatory in order to produce such structure and place the filaments along the lines of maximum stress.

As will be presented next, this work tries to combine the main advantage of FDM and AFP technologies. The FDM system is used with a single filament made up of continuous carbon fibers and thermoplastic matrix. In particular, the FDM allow to use a conduction heating system so to bring the thermoplastic material in a molten state with more efficient and economic mechanism. In fact, the conductive heat exchange allows to transmit power with high efficiency in a simple way. On the other hand, the AFP process uses mechanical roller that is useful in order to obtain the adhesion and the compaction between the layers. In the next sections a description of the FDM model will be reported, showing the main involved quantities. Then a discussion about the adhesion phenomenon will be presented. The AFP compaction roller is used to improve this, however no direct analysis will be conduct and in order to verify the adhesion and compaction, but tensile tests will be used in this work in order to evaluate adhesion due to external factors.

### EXTRUSION MECHANISM

In this chapter the extrusion phenomenon will be modeled and described both from the dynamic point of view and the thermal one because both fields are necessary in order to obtain good prints. The key elements of the FDM are the feeding system, that pushes the filament towards the liquefaction chamber, and the chamber itself [19].

$$v = Q / (A_f l) \qquad v = \omega_r R_r \qquad (1)$$

The feeding system is made up of two counter-rotating rollers which allow to control the volumetric flow rate of the filament entering in the hot chamber; it keeps the material supply rate as constant as possible by imposing a constant motor speed. Once the volumetric flow rate and the filament geometry are known, it is possible to calculate, by using the equation shown above, the feeding speed and then the rotation speed of the rollers (it is assumed the same radius for both the rollers). Of course, as in the case of the developed printing head, it could be necessary to take into account a transmission factor to relate the feeding roller speed and the motor speed (gear transmission is used in order to increase the torque on the feeding system). It is necessary to prevent the rollers from slipping on the filament in order to be able to keep a constant volumetric flow rate; in most cases there are grooves on at least one of the two



rollers. The two rollers are kept in contact with the filament by applying on one of that a force by means of springs. This radial force, coming from the springs, generates a tangential friction force on the filament that ensures the absence of slippage and allows to win the pressure drop of the filament along the tube between the feeding system and the nozzle exit. It is reasonable to assume the channel inside which the filament runs having a slightly larger diameter with respect to the filament diameter itself and therefore the pressure drops can be imputed only to the nozzle. It is very difficult to calculate the pressure drops so, in order to verify if the printing head is able to extrude the filament, during the development of the head only experimental tests are performed, acting on the driving roller speed and on the force exerted by the spring that assure filament-rollers contact. However, a complete model will be described.

$$F = \Delta P A_f \qquad C_m = F R_r \qquad P_m = \omega_r C_m \qquad (2)$$

$$P_{cr} = (\pi^2 E d_f) / (16 L_f^2) \qquad (3)$$

Generally, only one roller is driven (often by a stepper motor) while the second one is idler; therefore, once the force to be impressed in the longitudinal direction of the filament and the angular velocity of the driven roller are known, it is possible to use the equation (2) to evaluate the torque and power that the motor has to guarantee during the print. The geometry of the hot chamber imposes a limit value on the flow rate, in fact it is necessary to calculate by means of equation (3) (Euler buckling analysis) the ideal critical pressure value that causes the buckling phenomenon shown in Figure 97 [23]. This phenomenon prevents the correct filament movement so that an excessive material accumulation in the liquefaction zone appears, making impossible to control the amount of material coming out the nozzle. The equations can be applied even with composite filament, taking into account the elastic modulus calculated for example by the level rule. Even in this case experimental tests have been performed in order to select the right parameter for the extrusion.

Due to the difference between the filament diameter and the bore of the liquefier, the critical pressure value is calculated by multiplying the ideal one by a correction factor (typically 1.1x) [23]. The hot chamber is the component in which the filament increases its temperature until it reaches a molten state; the dynamics that rule this stage are very complex because many parameters vary according to the temperature, making therefore control algorithms difficult to be implemented.



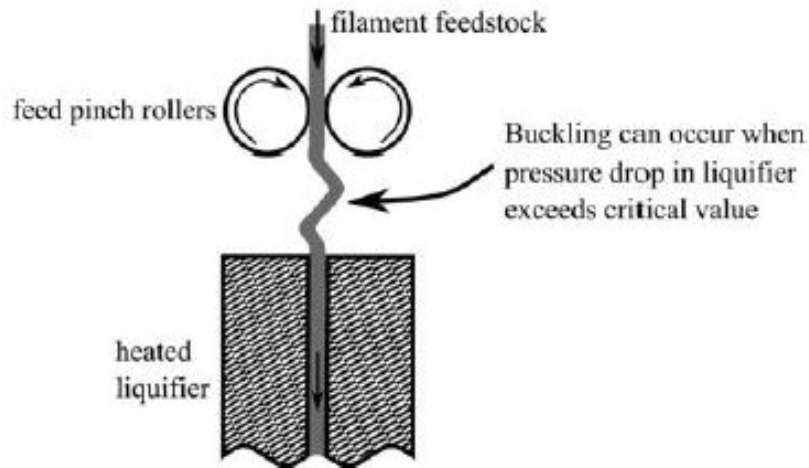


Figure 97: Buckling of a filament between the feeding rollers and the liquefier inlet [23]

$$\eta = K(\dot{\gamma})^{n-1} \qquad \eta = H(T)\eta_0(\dot{\gamma}) \qquad (4)$$

$$H(T) = \exp \left[ \alpha \left( \frac{1}{T} - \frac{1}{T_0} \right) \right] \qquad (5)$$

One of the fundamental parameters governing the filament motion between the inlet and outlet of the liquefier, is the viscosity, expressed by the Power-Law model (equation (4)); temperature dependence can be taken into account introducing the Arrhenius model reported in equation (5). This is a simplified model that does not take into account all the involved phenomena in the process but, however, it is applied to a wide range of materials commonly used in 3D printing process.

$$q = \dot{m}c_p(T - T_i) = \rho v A c_p(T - T_i) \qquad (6)$$

A further step for the construction of the model is to calculate the thermal power, by using the thermal balance equation (5), necessary to increase the material temperature and make it in liquid state. It will be used during the development of the printing head. There are two methods commonly used in order to supply heat to the system, the first one is to wrap a spiral resistance around the liquefier, the second one is to use ceramic "cartridges" inserted inside holes in the heating chamber block. The detection of the temperature for the control system is done by means of a thermistor (a sensor that measure temperature by using its resistivity variation as a function of temperature) or a thermocouple. In this work will be used hot ceramic cartridges and a thermistor sensor. It is possible to use the equation (6) under the following assumptions:



- filament is everywhere in contact with the hot chamber walls
- wall temperature is the same at each point
- the specific heat capacity coefficient  $c_p$  is assumed constant despite its great variation when the GTT is overcome

Finally, it is possible to evaluate the pressure drop inside the liquefaction chamber in order to evaluate the force required to move the filament, as mentioned before. By considering the simplified geometry of the heat chamber (composed by a cylindrical section I, a conical part II and a new cylindrical one III) shown in Figure 98, it is possible to obtain for each zone an analytical expression of the pressure drops by means of a momentum balance paired with the previously described viscosity model.

$$\Delta P_1 = 2L_1 \left( \frac{\nu}{K} \right)^{1/n} \left( \frac{n+3}{\left( \frac{D_1}{2} \right)^{n+1}} \right)^{1/n} \exp \left[ \alpha \left( \frac{1}{T} - \frac{1}{T_0} \right) \right] \quad (7)$$

$$\Delta P_2 = \left( \frac{2n}{3 \tan \left( \frac{\beta}{2} \right)} \right) \left( \frac{1}{D_2^{3/n}} - \frac{1}{D_1^{3/n}} \right) \left( \left( \frac{D_1}{2} \right)^2 (n+3) 2^{n+3} \right)^{1/n} \exp \left[ \alpha \left( \frac{1}{T} - \frac{1}{T_0} \right) \right] \quad (8)$$

$$\Delta P_3 = 2L_3 \left( \frac{\nu}{K} \right)^{1/n} \left( \frac{(n+3) \left( \frac{D_1}{2} \right)^2}{\left( \frac{D_2}{2} \right)^{n+1}} \right)^{1/n} \exp \left[ \alpha \left( \frac{1}{T} - \frac{1}{T_0} \right) \right] \quad (9)$$

$$\Delta P = \Delta P_1 + \Delta P_2 + \Delta P_3 \quad (10)$$

$$\Delta P \leq P_{cr} \quad (11)$$

The procedure used to obtain the analytical relationships is based on some hypothesis such as:

- there is no slippage between walls and fluid motion (zero speed of the melting contact with the walls of the hot chamber)
- fuse considered as incompressible
- motion of fluid is laminar and stationary

Equations from 7 to 9 report the expressions of pressure drop for each section; the total pressure drop in the liquefier is the sum of the three terms (equation 10). As shown in equation 11, the value of  $\Delta P$  must not be higher than the previously evaluated value  $P_{cr}$  if you want to have a correct print without incurring in buckling and missing extrusion problems.



This is the right procedure to verify if the printing process can take place. However, while the thermal power can be calculated and a control can be implemented, the calculation of the real pressure drop is too complex to take into consideration especially in case of composite material, so it is more convenient acts with experiments in order to find the best print conditions. So as already said the easy way to verify the extrusion is to change the motor speed and the force that keep the feeding rollers in contact.

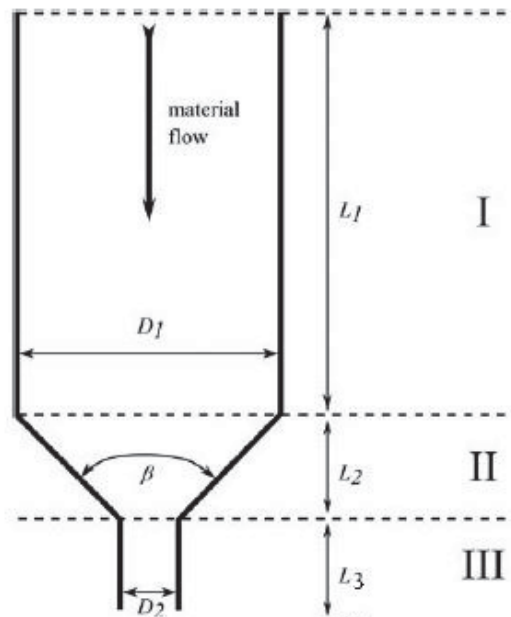


Figure 98: Model of liquefier

## CONTACT AND ADHESION MODEL

During the 3D printing process, the thermoplastic molten material adheres to the previously deposited layer through a diffusion phenomenon at the interface. The bonding forces between two different layers depends on several parameters including temperature, pressure and contact time. Figure 99 shows the process of molecular diffusion between the layers, once contact occurs; it is shown how the polymer chain bonds are formed, at the interface, therefore a hard bond is created after a certain amount of time. In order to develop this consolidation process, it is necessary to bring the thermoplastic material to a temperature  $T_m$  as shown in Figure 100, in order to provide a sufficient amount of energy to guarantee the molecules to move and complete the diffusion process [27].

$$D_{AU} = \frac{\sigma_{ad}(T, t_c)}{\sigma_{\infty}} \tag{12}$$



$$D_{AU} = D_{AU_0} + H(T)t_c^{1/4} \tag{13}$$

To evaluate the state of the bonding process between the interfaces, it is useful to calculate the "degree of bond" defined by equation 12, where  $\sigma_{ad}$  is the adhesion force and  $\sigma_{\infty}$  is the cohesion force [28]. It is possible to evaluate the degree of bonding by means of an equation 13 obtained by interpolating experimental data and using an Arrhenius temperature dependency for the  $H$  parameter.

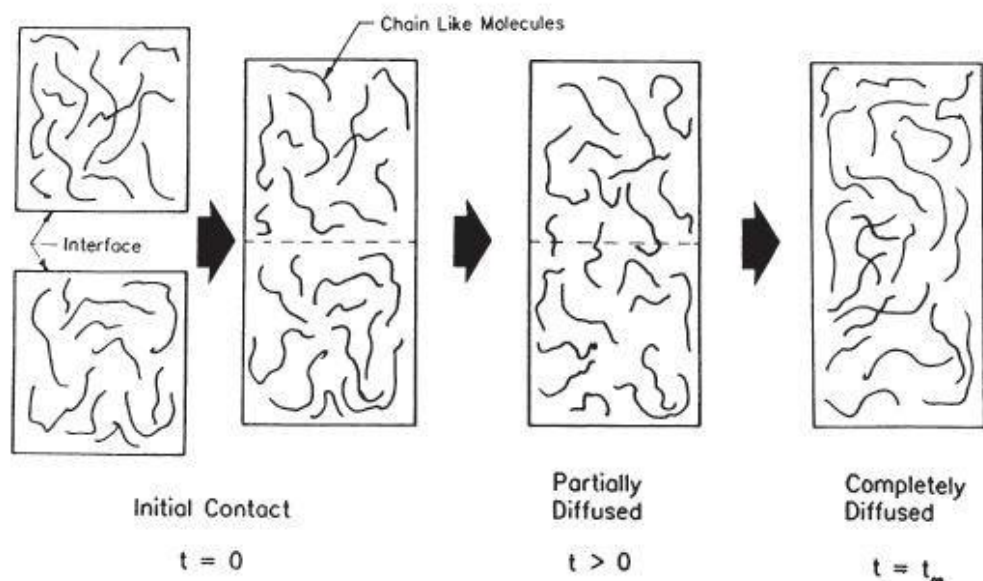


Figure 99: Illustration of the adhesion phenomenon [27]



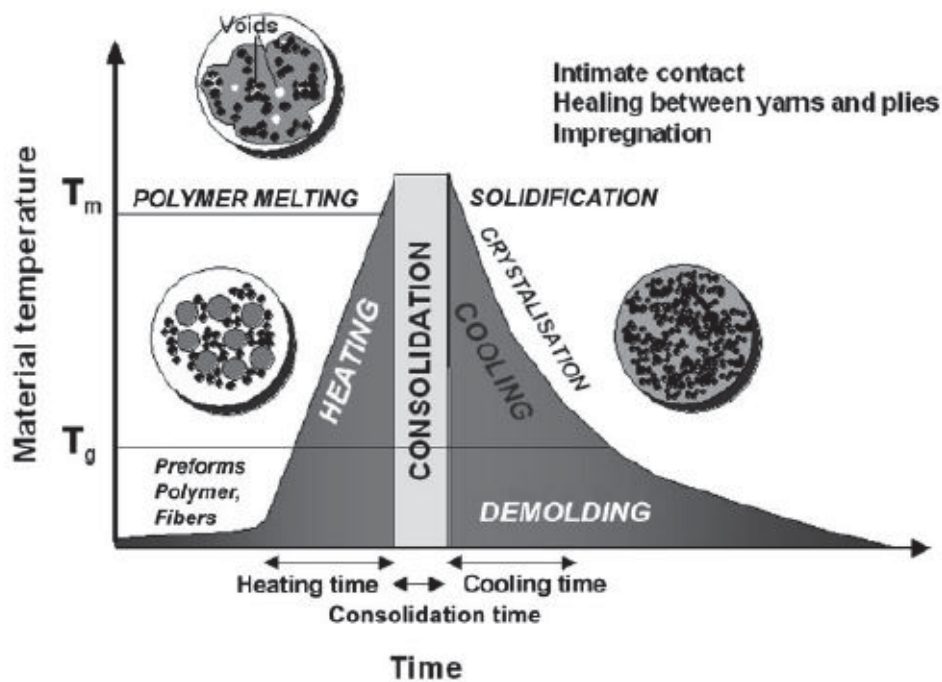


Figure 100: Compaction evolution as a function of time and temperature [27]

The cause of compaction mechanism and bonding phenomenon of two layers of a thermoplastic material has been identified as the diffusivity at the interface; all this can happen if there is "intimate contact" between the two surfaces. Also in this case it is useful to define a parameter in order to evaluate the contact status, this degree of intimate contact, as highlight in equation 14, is the ratio between the contact area and the total area projected on the contact plane [28].

$$D_{ic} = \frac{\text{contact surface}}{\text{total projected surface}} \tag{14}$$

$$D_{ic} = \frac{b}{b_0 + w_0} \tag{15}$$

Over the years, several models have been proposed in order to study this phenomenon, the main ones are shown in Figure 101; all these models describe the surface asperities as rectangle, distributed with a constant trend (Lee & Springer model) or with a statistical distribution (Weibull). The simplest model is the Lee & Springer one; according to this model the surface is formed by rectangles equal to each other with width  $b_0$  and height  $a_0$  interspersed with a gap  $w_0$ ; in this case the degree of intimate contact can be formulate by means of equation 15.



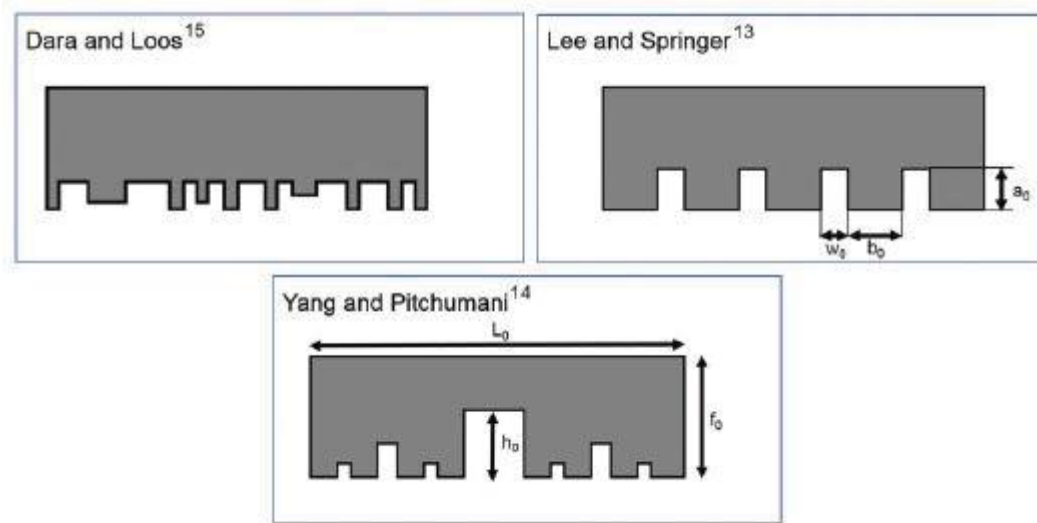


Figure 101: Representation of surface models [28]

$$D_{ic} = \frac{1}{1 + \frac{w_0}{b_0}} \left[ 1 + 5 \left( 1 + \frac{w_0}{b_0} \right) \left( \frac{a_0}{b_0} \right)^2 \int_0^{t_c} \frac{P_{app}}{\eta(T)} dt \right] \quad (16)$$

Furthermore, the degree of intimate contact can be derived by using a one-dimensional Newtonian flow model (equation 16); the evolution of intimate contact over time, can be described as a function of the applied pressure and viscosity of the material (the contact starts at  $t = 0$  and continues up to  $t = t_c$ ). For the description of the other two models see [28]. The main parameters of the adhesion phenomena are temperature and pressure applied between layers; of course instead of study the real evolution of the adhesion phenomenon, the easiest way is to perform a tensile test (once a proper extruder temperature has been selected) by changing the applied external pressure and see the how the 3D printed specimen mechanical parameters change. The use of compaction rollers coming from AFP technology, allow to modify the pressure exerted on the material during the deposition in order to evaluate if a larger pressure allow to have better mechanical properties as you would expect.

## HEAD

The printing head is designed considering the processes of FDM (concerning the feeding system and the hot chamber) and of AFP (concerning the compression system) with the idea of use continuous reinforced carbon fiber (CRCF) filament; a prototype of the extruder was developed in a previous work [29]. The printing head already developed has been tested in order to demonstrate that the CRCF filament can be 3D printed by combine the best advantages of FDM and AFP. Now, in this work, it will be modified in order to assess a more deterministic system that allow to control a fundamental parameter as the layer compaction force. In fact, as it will be presented in the next section, a measurement system has been



taken in consideration in order to evaluate the compaction force used along the entire printing. As already done, the modified printing head is mounted on a Lulzbot TAZ 4 3D printer (a commercial Cartesian printer), with a modified firmware, in order to evaluate if the modifications that will be made works in a proper way. In order to test the effectiveness of the printing head, samples with constant rectangular cross section are printed and then tested with a tensile test; it is therefore possible to extract mechanical information as the elastic modulus that is the main parameter to highlight the goodness of the compaction system. In the experiments on the Lulzbot TAZ the Markforged filament, whose characteristics are reported in Table 22, was used. The Markforged filament is composed by a percentage of 34% of continuous carbon fibers prepreg with a PA6 thermoplastic matrix. The single carbon fiber has a diameter of about  $7 \mu m$  and the final filament has a diameter of  $0.4 mm$ . With this kind of filament it is possible to have a proper homogeneous cross section filament, avoiding the necessity to feed separately and then merge the reinforcing fibers and the plastic matrix as proposed by Matsuzaki [30]. In fact, in this latter case it is easy to not achieve a good distribution of carbon fibers and thermoplastic matrix in the cross section, therefore the final object can have a very low resistance.

**Table 22: Markforged filament properties [30]**

Property	Test Standard	Carbon CFF
Tensile Strength [MPa]	ASTM D3039	700
Tensile Modulus [GPa]	ASTM D3039	54
Tensile Strain at break [%]	ASTM D3039	1.5
Flexural Strength [MPa]	ASTM D790	470
Flexural Modulus [GPa]	ASTM D790	51
Flexural strain at break [%]	ASTM D790	1.2
Compressive Strength [MPa]	ASTM D6641	320
Compressive Modulus [GPa]	ASTM D6641	54
Compressive Strain at break [%]	ASTM D6641	0.7
Heat deflection temperature [ $^{\circ}C$ ]	ASTM D648	105

### Existing Printing Head

The initial extrusion system is shown in Figure 102, it is composed by the main parts described previously: the feeding system, the heat sink, the hot chamber, the nozzle and the compaction system designed for the scope. The filament, as already said, is composed by continuous reinforcing fibers and thermoplastic resin so that the overall filament have to considered as inextensible one and so the speed at the inlet and outlet of the extruder can be considered the same; this allow to have a simpler case with respect the

traditional FDM process. In this case in fact it is possible to have the same value of speed of the head slider and of the linear feeding motion.

As already mentioned in the previous Chapters, the heat sink prevents the increase of temperature of the filament between the feeding rollers and the hot chamber, in this way the filament can act as a plunger on the heated part of filament in the liquefier and make the extrusion possible. The internal channel has a diameter of about 2 mm, in fact in order to prevent the buckling effect, it was necessary to introduce a copper tube to reduce the original diameter of the channel that connect the feeding rollers and the nozzle.

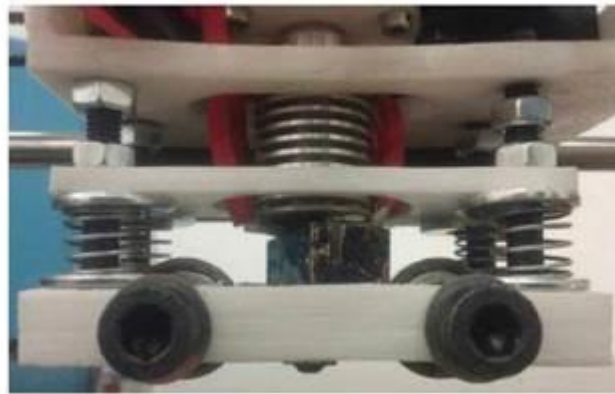


**Figure 102: Printing head and compression system of the first prototype**

In Figure 103, it is represented the compaction system developed by Dentelli [29]. It can be noted that the compaction force exerted by the two bearings, used as rollers, on the extruded material is generated by four springs that can be independently preloaded in order to set up the desired force. The rollers are mounted on a translating plate, the fixed frame (1) is the reference that allows to modify the layer height by means of four screws; the preload can be regulated by translating the plate (2) by means of nuts. The entire printing head is mounted on a slider that allows motion in x direction. With this configuration it is not possible to measure the spring preload and relate it directly to the roller compression force. In fact, the plate that supports the rollers pairs the effects due to the two rollers and it is very difficult to separate the single contribution on the layer to be compacted. A further step, that it is developed in this work, is to modify the compaction system in order to apply the desired force with the two rollers in an independent way.

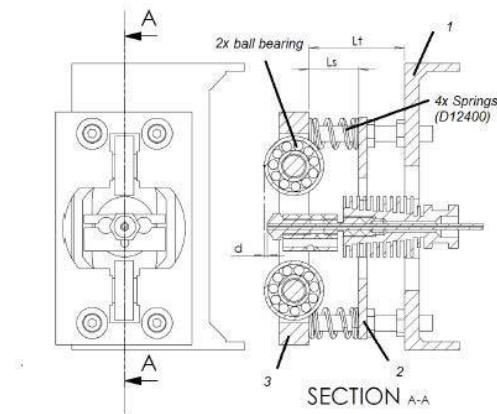


Figure 103: Schematic representation of the first compaction system [29]

A system not present on the original TAZ is the filament cutting system; now it is a useful tool in order to cut the CRCF filament in order to deposit it along specified directions so to make the fibers work always in tensile configuration. As depicted in Figure 104 by means of a four-bar mechanism it is possible to cut the filament and once the shear modulus of the filament and the motor torque are known it is easy to verify by using equation 17 that the cutting shear stress is greater than the shear stress of the filament. The shear stress calculated with the Jourawsky formula (equation 18) is then greater than the filament shear strength (70-90 MPa). The cutting system can be actuated by means of a G-CODE command; it is a useful tool in case the component layers have many discontinuities that cannot be precisely followed with a Cartesian movement system.

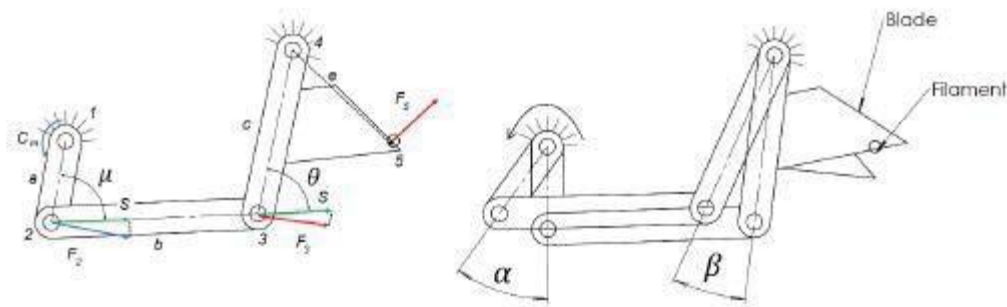


Figure 104: Schematic representation of the filament cutting system [29]

$$F_2 = \frac{C_m}{\alpha} \quad S = F_2 \sin \mu \quad F_3 = S \sin \theta \quad F_5 = F_3 \frac{c}{e} \quad (17)$$



$$\tau_{cmax} = \frac{4F_5}{3A_f} = 400MPa \quad (18)$$

The last relevant part of the printing head is the heating system. The hot chamber is made up of aluminum and it presents two holes for the heating cartridge used to heat up the filament, an M6 thread used to connect the nozzle to the feeding tube and a small hole in which take place a thermistor (Figure 105). They are placed two hot cartridges, powered by a 12V generator, and each of them generates 40W; therefore, once the overall heating power is known, it is possible to apply the equation 6 in order to evaluate the maximum ideal (without considering thermal power losses) printing speed (35 mm/min) and so the motor rotation speed. The thermistor used is a NTC sensor [31]. A thermistor is a sensor that allows to calculate the temperature knowing how the resistance value changes with the temperature itself. The equations derived by Steinhart-Hart are used to calculate the instantaneous temperature in order to make simple to maintain as constant as possible the desired temperature by means of a PID control [32]. In case of TAZ the Steinhart-Hart are not evaluate because the printer has a look-up table in its software, while when the printing head will be mounted on the robot, this equation will be really implemented in an Arduino program. In the printing head NEMA17 stepper motors with a nominal torque of 0.4 Nm are used; the choice of this kind of motor is due to the great number of advantages:

- low cost
- facility to control speed and position
- possibility to achieve high acceleration due to a low value of rotor inertia
- possibility to have low value of speed without the use of gearbox
- high holding torque

Anyway they have also some drawbacks:

- driver devices are required
- vibrations at low regimes
- the maximum speed is limited

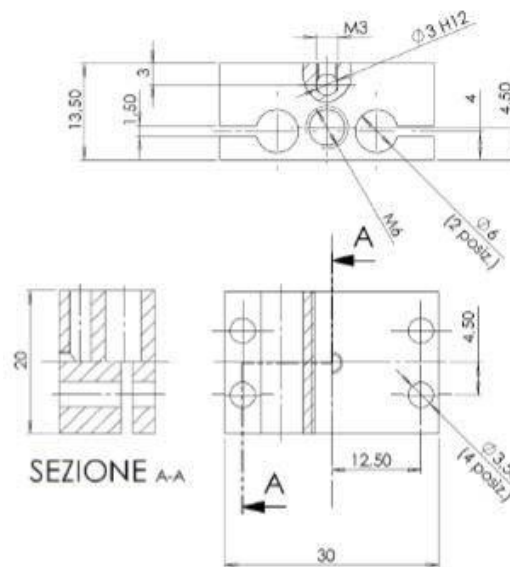
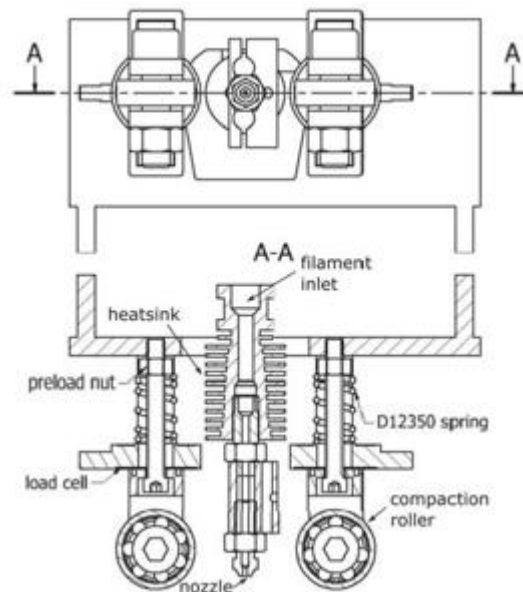


Figure 105: Schematic representation of the hot chamber block

### Modified printing head

As already said in the previous section, the printing head does not allow to set in a proper way the value of preload of the spring and with that configuration it is not easy to evaluate the compaction force exerted by the rollers. Therefore, it is necessary to develop a new structural solution that allow to overcome these problems. The solution has been found by using only two springs and positioning their axes coincident to the compaction force direction. In this way it is straightforward to measure directly the compression force. All the structural parts have been 3D printed; the first material used for the new system was the PLA, this material is quite strong and so it can be used in case large loads have to be sustained. The PLA has been used, being the most economic 3D printing material, in order to only validate the design and the size of the system. The drawback is the poor heat resistance and even if these parts are not directly in contact with the hot chamber, the heat coming from it and from the hot-bed could deflect the structure. Because the hot-bed temperature is set to 70 °C and the hot chamber to 280 °C, it was necessary to choose a material with a better heat resistance in order to make experimental tests. Therefore, the new parts have been printed with an HIPS filament; this material has the same property of ABS but it can withstand up to 100 °C. The HIPS allow to made all the tests of print and to validate the system. Of course the parts that will be mounted on the robot will be made up of steel. In addition, two fan supports have been built up, so that the fans can cool down the upper part of the structure and avoid the risk deflection. The system with the new compaction system is shown in Figure 106 and its 2D section in Figure 107. In the new compaction system has been removed the preload plate and the plate that holds the rollers; in fact, now the rollers are supported by two independent supports and a screw keeps them at the right distant with respect the fixed structure. The screws act also as support for the springs whose preload is set by means of nuts. With this solution the rollers are independent and their vertical motion can be independently from each other. The roller supports are connected with the upper frame by means of two prismatic joints; in this way the motion is only in the vertical direction.



**Figure 106: Schematic representation of the modified compaction system**

In order to measure the compaction force a donut load cell is put in series for each spring. The used sensors are FUTEK lth 300 capable to read a force up to 445 N [33]. From one side the load cell is in contact with the roller support and from the other side it is compressed by the spring so that the read value is directly the useful compaction force. The prismatic joints allow to avoid a reaction torque on the screw and so an introduction of a fictitious force that acts as a disturbance on the load cell measurements. Another important aspect of the new system is that as for the previous one, it is possible to independently change the nozzle-bed distance, by means of the screws, and the spring preload, by means of the nuts. The possibility to set a preload allow to increase the compaction force as you want keeping the layer height constant.

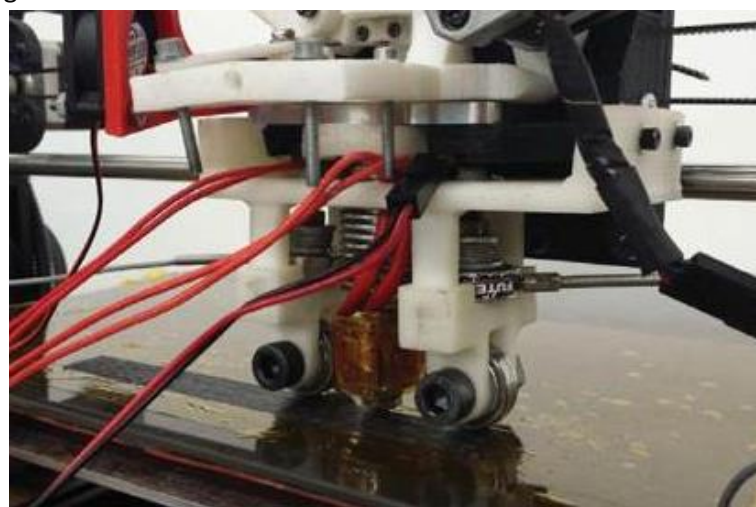


**Figure 107: New printing head during the print of a carbon-PA6 sample**

## Validation of the System

The new printing head has been tested on the Lulzbot TAZ with the Markforged filament, with a nozzle and bed temperature respectively set to 280 °C and 70 °C, a layer height of 0.2 mm and a printing speed of 11.3 mm/s. The printed samples have a length of 150 mm, a width of 20 mm and a thickness of 1.2 mm (Figure 108).



**Figure 108: Samples printed on the TAZ with the Markforged filament and the new printing head**

It was decided to print samples with three different preloads; the value of the preload for each load cell is obtained by reading the voltage coming from the sensor by using a NI DAQ conditioning system. The voltage values are then converted into force values and by means of LabVIEW program it was possible to acquire and save the load temporal history. The preload for each spring is set by looking at the value measured through the computer and then once the value is the same for both the load cell, the printing process was started. During the print, one time for each layer, short compression force histories have been saved in order to evaluate the stationarity of the process. Even if the mean value is more or less constant over time, it can be noted some fluctuation; this phenomenon can be due to some deformation of the compression structure as soon as the ambient temperature rises due to the hot chamber and hot-bed thermal power.

The printed samples are tested with a tensile test in order to determine the elastic modulus and the stress values. The test is useful to verify the functioning of the new printing head and to quantitatively define the influences of the printing parameters on the mechanical properties of the samples. In Table 23 the results of three cases are reported.

**Table 23: Tensile test first samples**

	Case 1	Case 2	Case 3
Preload [N]	3.53	4.61	6.67
E1 [GPa]	47.08	50.68	54.92
E2 [GPa]	46.96		53.94
Rm1 [MPa]	370.25	416	457
Rm2 [MPa]	351		404

Figure 109 shows the results of the tensile test in a  $\sigma - \epsilon$  chart; it is easy to see that as expected the behavior of the samples is brittle. For cases 1 and 3 two samples has been printed while for the case 2 only one sample has been printed because the preload is quite similar to the case 1 (the springs is not so rigid to allow a distinguish of many cases and so the spring will be changed as the head will be mounted on a 6-axis robot). For a preliminary analysis of the results, case 1 and case 3 can be compared. The table shows how the Young modulus is higher in the case 3 with respect case 1, so it suggests that the higher the preload the higher is the elastic modulus. As said before it was necessary to use an acquisition system in order to measure in a deterministic way the preload of the springs. In fact the main parameter to take into account is of course the compaction force; the strength of the sample however is not linear with the applied load. Figure 110 shows the results of Young modulus and UTS, the material seems to show better performances as the applied compaction load rises. At the end of the last sample, the main frame of the compression system suffered a deformation, this phenomenon indicates that the HIPS material cannot withstand to many cycles of work under a condition of applied load and heat; the structure so should be changed periodically. The simplest way to overcome the problem could be change the frame geometry in order to increase the thermal inertia or increase the complexity of the cooling system, taking into account that the fans do not have to modify the temperature gradient around the printing zone, to change the material of the frame. As mentioned before, the system that will be mounted on the robot will be made of steel.

From the acquired measurements (Figure 111), you can note some important spikes when the print is running. As can be seen, the preloads (Table 23) and the acquired loads do not really the same. The reason is that another component of force, in addition to preload, appears due to the vertical movement of the roller due to the layer height that compress further the spring (about  $2 \text{ N/mm}$ ) when the roller itself climbs the filament and starts the compaction phase.

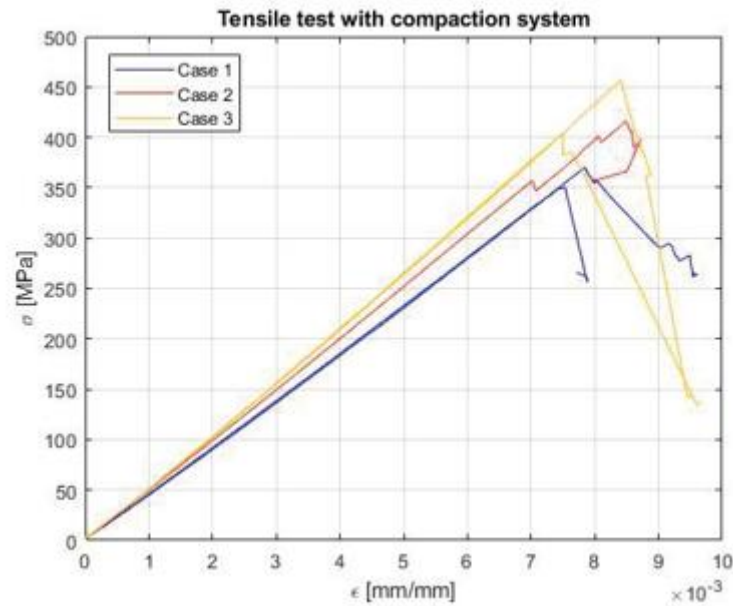


Figure 109: Graphical results of the sample tensile test

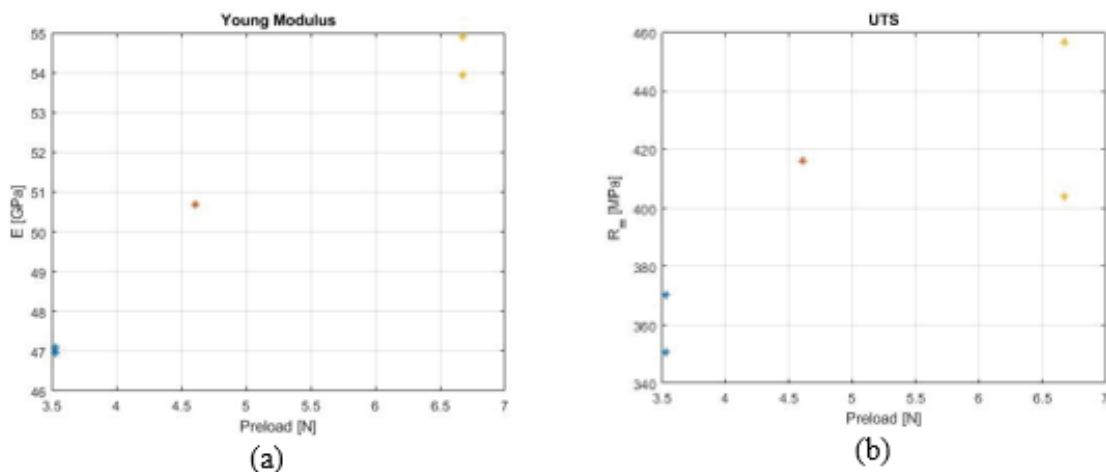


Figure 110: Tensile test results of Young modulus (a) and UTS (b)

This phenomenon will be deeper described subsequently by using acquisitions that better highlight this phenomenon. For each case previously mentioned, there was the same behavior in the signal history; the spikes appear with a regular distribution and have an equal time-space. Because in each print and with different preload this phenomenon is present, a Fourier analysis has been performed in order to investigate and search the causes of the disturbance. The FFT analysis shows for each case the presence of the same fundamental harmonic component with a frequency of about 7.3 Hz. Moreover, there is a significant contribution of the components multiple of the basic frequency. This kind of disturbance has been noted only when the printing process happens therefore the simplest thing that it was made was to calculate the frequency of all the moving parts of the extruder. The results reported in Table 24



considering a printing speed of  $11.3 \text{ mm/s}$ , show how the closest frequency to the one observed through the FFT spectrum is the one related to the belt meshing. The belt is connected to the motor that moves the printing head in the y-direction (parallel to the compaction roller rotation direction). This suggests that the belt introduces a forcing component that acts on the system. The next step is to mount the printing head on a FANUC robot manipulator and the idea will be to control it by using the information coming from the load cells. In this case the spikes would be external factors that make impossible to control the robot in a precise way; but because the belt will not be transferred on the robot, more analysis are not carried out. In any case because you know that the spikes are fictitious force coming from the belt meshing that make the force oscillating around the true mean value, it is possible to cancelled out them by applying a moving average on the original signal during the acquisition (red signal in Figure 111 (a)).

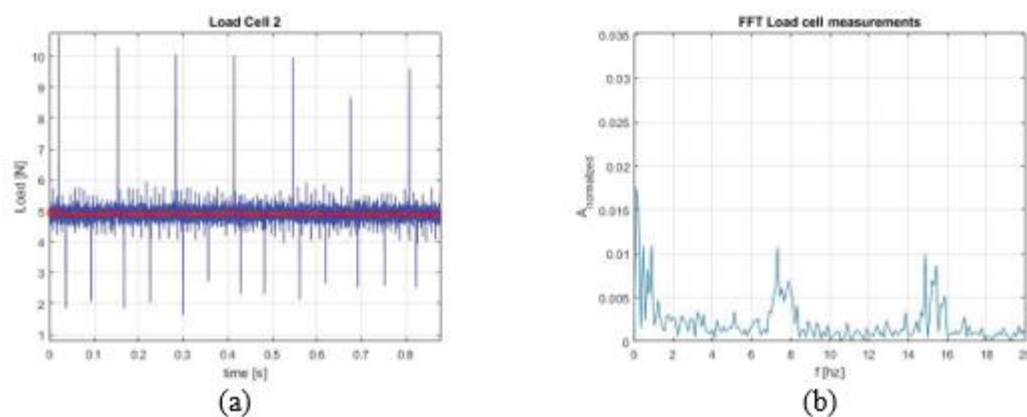


Figure 111: Load cell measurements: load time history (a) and FFT signal analysis (b)

Table 24: Natural frequencies of extruder moving parts

<b>Motor frequency [Hz]</b>	2.21
<b>Gearbox mesh frequency [Hz]</b>	22.54
<b>Roller-bearing frequencies [Hz]</b>	Train frequency: 0.39 Outer race defect frequency: 2.71 Inner race defect frequency: 4.5 Ball defect frequency: 3.91
<b>Belt meshing frequency [Hz]</b>	7.67

## ROBOT SETUP

A further step in this work is to mount the printing head developed on the TAZ 4 on a FANUC manipulator present in a Politecnico di Milano building. The extruder was put on the robot by means of a connection system able to allow the robot working in different poses. Then in order to allow the filament deposition an electronic control system based on Arduino IDE and a software based on Grasshopper were developed. The first part is used to control, as it will be described next, the main parameter of the printing system, the second one is used to create the trajectories followed by the end effector of the robot.

### Electro-mechanical Setup

The first step was to connect the printing head and the robot; this was carried on by using the system in Figure 5.1 (a) that allow to use the robot with different pose depending on the wanted trajectory. This system is composed by a flange screwed on the robot, two lateral supports that sustain a cube on which the extruder will be mounted. The cube can be assembled with a relative angle orientation with respect the supports so to have more freedom on the robot pose selection.

In order to mount the extruder on this system, a connecting plate was designed. The connecting plate is made up of steel and can be divided into two parts: one side is used to connect the ABS part of the printing head by means of six M3 screws (already assembled in Figure 112 (b)), the second side is used to connect the plate to the robot attach system (Figure 112 (a)) by means of four M8 screws.

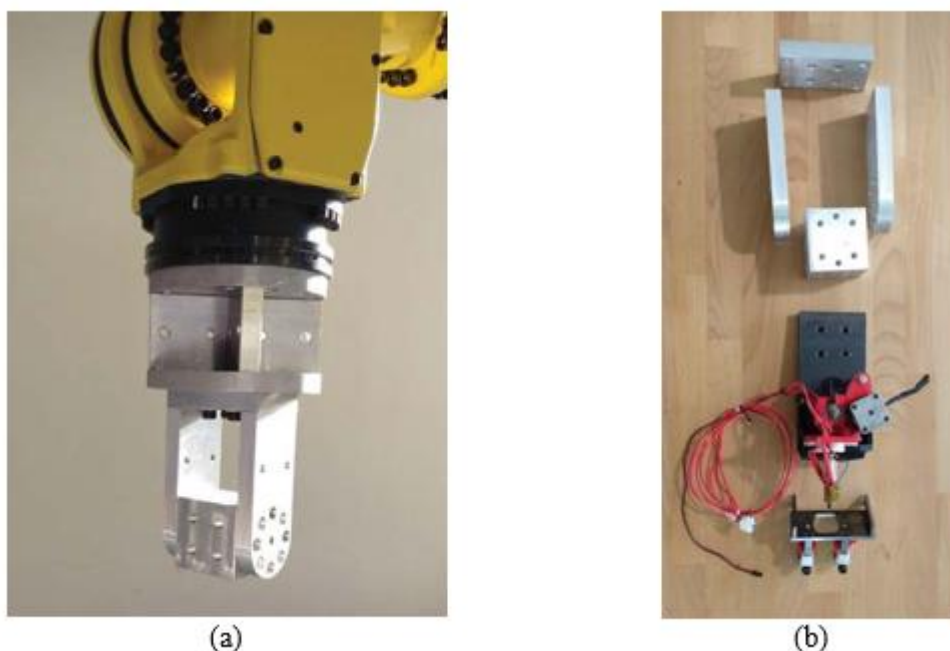


Figure 112: Robot-extruder connecting system

All the component used in the robot-extruder connection do not have a centering system because the reference position of the robot TCP (tool center point) can be modified before each print or whenever a new mounting operation of a tool is performed. In order to have success in the print it is necessary to

have the possibility to measure and control the main parameters such as temperature and extrusion velocity. This was possible by using an Arduino UNO controller able to collect data and take decisions based on sensor measurements. Arduino is an open source project mostly used in the Do It Yourself world (DIY), it is used to measure analog or digital inputs, to make calculations and to generate digital or analog (by using the Pulse Width Modulation - PWM method) signals. The printing electronic control system can be schematized as shown in Figure 113. The system can be divided into five main parts:

- filament feeding motor
- cutting system motor
- heated bed
- hot chamber
- Arduino UNO

The motors used for filament feeding and cutting systems are NEMA 17 stepper motors; stepper motors are very easily to control in position and velocity and allow to have sufficient accelerations. The feeding motors is controlled in velocity because it must continuously run during the print phase; a rotation speed is imposed so that the filament and the printing velocities in X,Y and Z directions (spacial directions) are the same ones. On the contrary the cutting motors is controlled in position because in order to cut the filament is required a single rotation. The way to control these motors is to use an A4988 driver board; the driver is a module that receives the signals from Arduino board and regulates the available currents for the motors based on the wanted performances. In order to guarantee a precise motion, the driver is set so to have a microstepping configuration; there are three PINs on the driver and depending on the imposed state (high - low) it is possible to set the rotation accuracy of the motor. The rotation of the stepper motor is discretized in a finite number of steps (commonly *200 steps/revolution*), but as already said by means of microstepping it is possible to increase these steps, reaching in our case *1600 steps/revolution*, without decreasing too much the torque. In this case bipolar stepper motors are used with a maximum torque of *0.4 Nm* if supplied with a current of *1.5A*. At the same time a driver capable to provide a maximum of *2 A* was used; the maximum current is set equal to the maximum current required by the motor by set a potentiometer and applying the formula  $V_{ref} = 8R_s I_{TripMAX}$  in order to have in our case ( $R_s = 0.05 \Omega$ ) a voltage difference between the potentiometer IN and the ground of about *0.6 V*.

The print surface used was the TAZ 4 heated bed; the bed is powered by a *12 V* power supply. The power consumed by the bed is about *100 W*, being its internal resistance of about *1.4  $\Omega$* ; the plate temperature is keep to the desired ones by means of a PID algorithm and a thermistor sensor in order to close the control loop. The same strategy was used in order to control the temperature of the hot chamber which consumes *80 W* by means of two *40 W* ceramic cartridges.

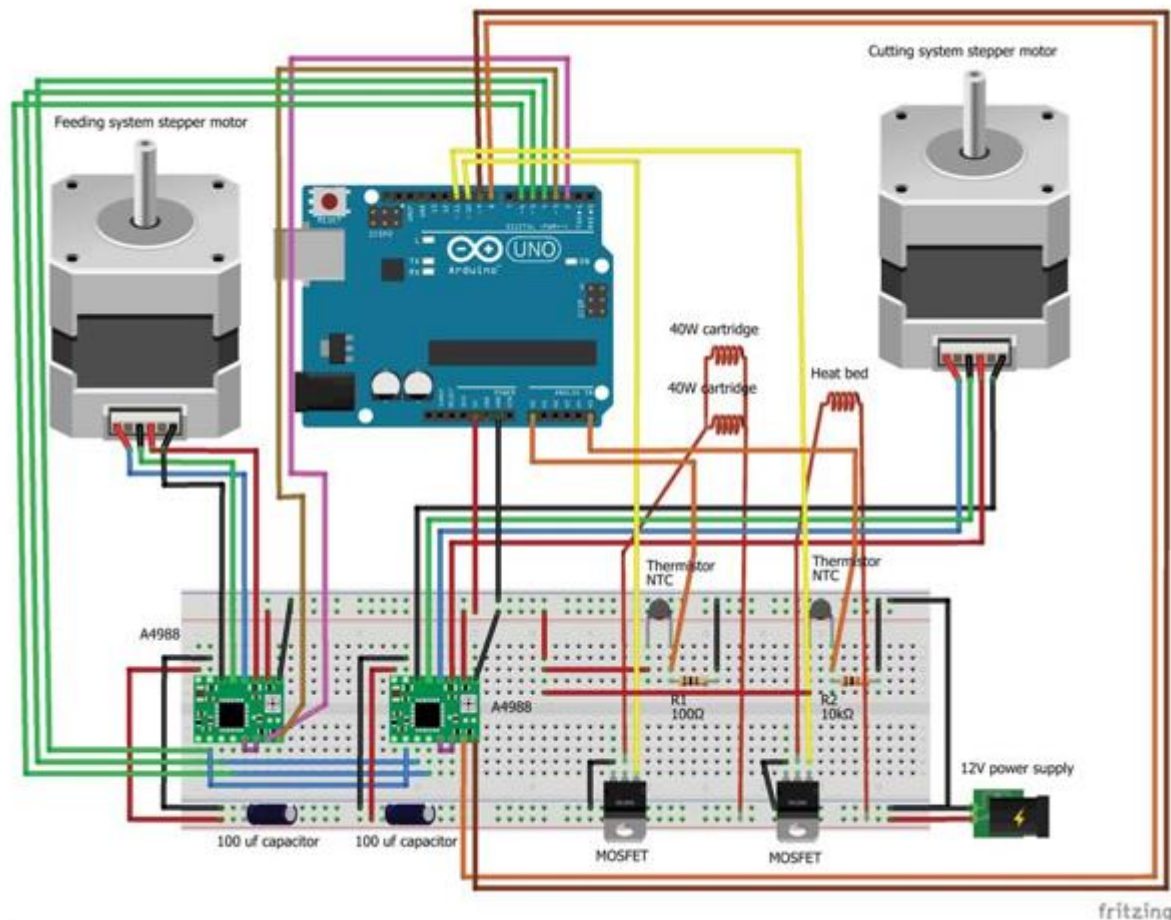


Figure 113: Scheme of the printing head circuit

As it will be presented next, a power of 80 W is enough in order to bring the thermoplastic part of the composite filament (with a cross section larger than the Markforged one) to a molten state to perform the print. The PID control as already said takes as input the temperature measured by means of a thermistor and compares it to the desired one (set point temperature). The output coming from the control algorithm is limited in the range 0-255; it represents the maximum range of the Arduino output by using the PWM method. This range represents the duty cycle of PWM signal (periodic signal with a frequency of 490 Hz or 980 Hz); 0 is related to low state (0 V) and 255 is related to high state (5 V) over the entire period of the signal. Of course by using intermediate value it is possible to modify the mean state level of the signal reaching intermediate values. In order to control the power of bed and hot cartridges, the output is sent to the MOSFET gate [28] so that according to the output value, a voltage difference appears between the electric load, connected between the MOSFET and the power supply, and the current can flow between the drain and the source pins. The MOSFET can be seen as an electrical switch, that allows the flow of current if a voltage difference is applied on the gate. Fortunately, the gate (for logic level MOSFET) requires a very low voltage to be activated so it can be use directly an Arduino PIN as shown in Figure 113. The last step is the MOSFET sizing in order to evaluate the heat dissipation



and if a heat sink is required. The power components employed in this circuit are IRLZ44N n-channel MOSFETs whose main characteristics are reported in Table 25.

$$P_{MOSFET} = I^2 R_{DS(on)} \quad (19)$$

**Table 25: IRLZ44N n-channel MOSFET properties**

Electrical quantities	Symbol	MOSFET
Drain-Source On-State Resistance [ $\Omega$ ]	$R_{DS(on)}$	0.022
Gate-Source Threshold Voltage (max) [V]	$V_{GS(th)}$	2
Maximum Junction-to-Ambient Coef. [ $^{\circ}C/W$ ]	$R_{thJA}$	62
Maximum Operating Junction Temperature [ $^{\circ}C$ ]	$T_J$	175

**Table 26: Heated bed and hot chamber properties**

Electrical quantities	Hot Chamber (One cartridge)	Heated Bed
Resistance [ $\Omega$ ]	4.2	1.4
Voltage [V]	12	12
Current [A]	2.86	8.33
Power [W]	40	100

$$P_D = (T_j - T_{amb}) / R_{thJA} = 2.42 \text{ W} \quad \text{with } T_{amb} = 25^{\circ}C \quad (20)$$

Knowing the MOSFET parameters it is possible to calculate the dissipation capacity, without heat sink, by means of equation 20 (definition of thermal resistance). By using the Table 26 and the equation 19, that refers to the power to which a MOSFET is subjected during the running of an electric load, it is straightforward verify that both for the heated bed ( $P_{MOSFET} = 1.53 \text{ W}$ ) and the hot chamber ( $P_{MOSFET} = 0.72 \text{ W}$  considering two hot cartridges) the sizing of this part of the circuit is verified. The entire circuit is controlled by Arduino and so a proper software has been developed. The first part of the program initialize the variables and the wanted values of printing velocity and temperatures are set; then a second part defines the variable to be controlled and the PID coefficients (defined by a trial and error approach). In the last part, the input-output commands are read and generated and the calculations are executed in loop. Without going into details, an Arduino-PC serial communication is introduced in order to decide



when switch on/off the motors and the heaters, by means of keyboard inputs. Nowadays the FANUC robot does not allow a communication with Arduino and cannot be controlled directly because its firmware cannot be modified by users. However, the FANUC engineers are planning to create a subroutine in the firmware in order to allow an input-output data exchange. In case the communication can be established, keyboard inputs are no more necessary and based on the TCP position of the robot it will be possible to give to Arduino the capability to make autonomously the right choice. Because of the absence of this kind of communication, it was not possible at the moment to use the cutting system (because should be activated depending on the trajectory of the manipulator) and to locally control the force (measured by means of FUTEK load cells) by changing the trajectory in real time. However, the force value and so the spring preload is set before the start of the print and it will be used an open loop approach by using the LabView program.

### Robot Trajectories

Once the system that controls the printing head has been completed, it was necessary to generate the trajectories that the robot TCP have to follow. This has been done by using Rhinoceros V5 software with Grasshopper plugin. This plugin is a 3D parametric program that allows to manage with many elements such as points, curve line and any kind of surface. Grasshopper provides a graphical script interface allowing to create almost any kind of geometries and modify them simply acting on parameters defined in the script itself. The result of the script is then shown into Rhinoceros and once saved, it can be used in other projects. Figure 115 shown the script developed in order to obtain the trajectory (polycurve) needed for the printing of the composite samples; as described next, two possible samples can be defined selecting an initial switch. The developed script is already able to generate trajectory of samples with different curvatures in x and y direction (directions of the sample edges), in order to have the more generic situation. However, this implementation is not used in this work because the focus is on planar print but it will be used in a following work and in special 3D print. The instruction flow goes from left to right. Initially there is the definition of the sample and its dimensions and the definition of the number of points along the edges; once the points in both directions are created, it is possible to create a points pattern by introducing a matrix multiplication. In this part of the script it is also possible to choose the curvature in x and y direction if you decide to print using a mold or on a moving support as presupposes for a next work. Following the script flow, there is the definition of hatching space (in plane filament deposition distance), the single layer height and the sample height. Then the last part of the script evaluates the connection strategies, between the single line, in plane and along z direction.



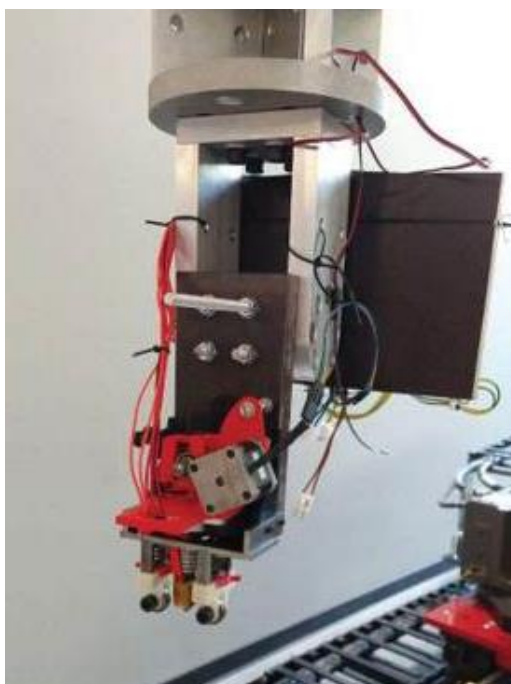


Figure 114: Final robot setup

As already said, the final result of the script is the polycurve that the robot TCP has to follow. The script allows to create sample with crossed direction layers (Figure 116) or with layers that have the same deposition direction as shown in Figure 117. This last kind of samples will be used to investigate the best print parameters. Once the polycurve has been created, it is possible to export it and by using another script, already implemented, it is possible to impose for each point of the curve, the desired kinematic quantities in terms of velocity, acceleration and arm orientation. At this point a ".txt" file is generated with all the points that the manipulator has to reach and all the relative information for the right positioning.

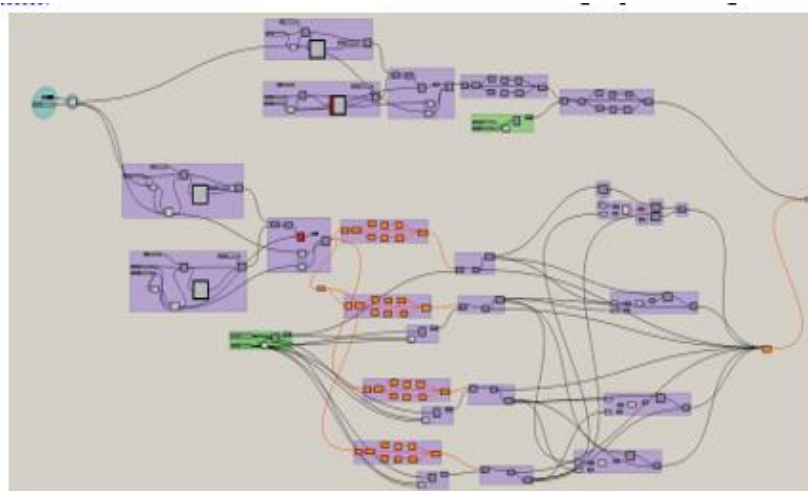


Figure 115: Grasshopper script for sample trajectory definition

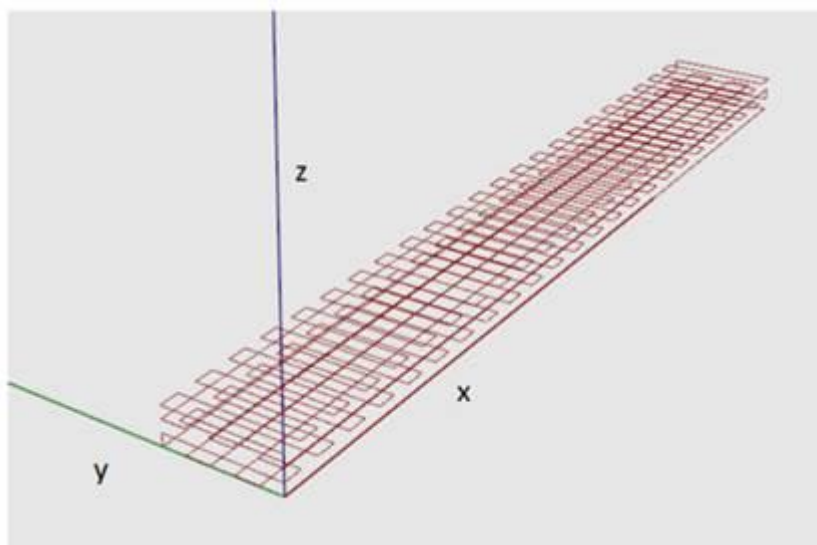


Figure 116: Example of trajectory of crossed-layer composite 3D print sample

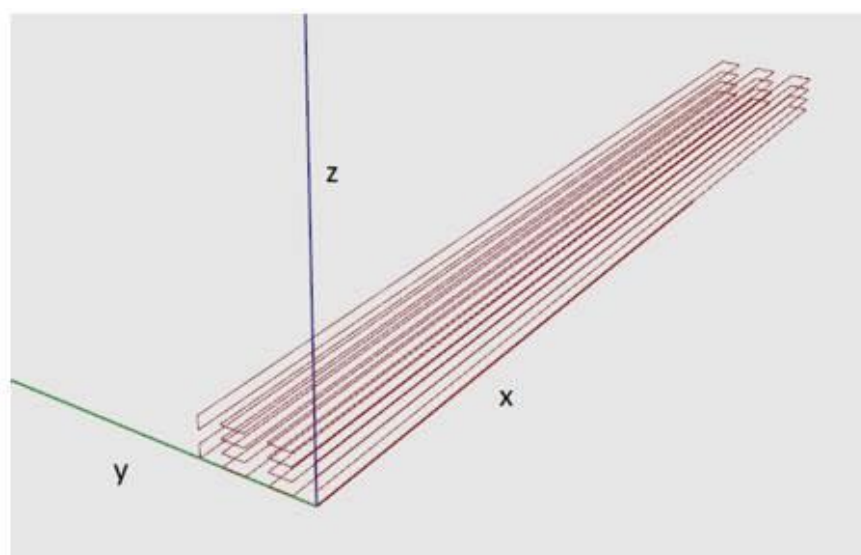


Figure 117: Example of trajectory of simple composite 3D print sample

## COMPARISON OF CCF FILAMENTS AND SAMPLE TESTS

The 0.4 mm Markforged filament, used for testing the modified printing head and for making the first tests is no more adequate because now the manipulator has a larger printing volume than the TAZ printer, so it makes more sense to use a filament with a larger cross section in order to increase the productivity and the volume building rate. The 3D printing with CRCF filament is a new technology so a proper filament that can be easily extruded is not so easy to find on the global market and the cost of this kind of filament is very high. A solution that has been find is to use a prepreg twisted commingled yarn



composed by continuous carbon and polyamide fibers. Three filaments have been acquired by the "Concordia Fibers" firm, one composed by a volume fraction of 41% of AS4A carbon fibers (12K) and 59% of nylon PA6, one changing the PA6 with the PA12 and the last composed by a volume fraction of 39% of AS4C carbon fibers (3K) and 61% of nylon PA6 (with a diameter smaller than the first two filaments). The PA has been selected as matrix resin because of its chemical stability, relative low extrusion temperature and high mechanical strength. The carbon fiber percentage has been chosen in order to have good mechanical properties maintaining a certain level of toughness and the possibility to have a good prepreg of the filament. The initial filament is twisted so to ensure a more circular cross section with a diameter of almost 2 mm. The choice to use a filament with this dimension derives from two necessities: increase the building rate, as already mentioned, and the geometric dimension of the nozzle and heat break commercially available. The PA resin, as for the Markforged filament, has been chosen because of the high maximum service temperature (80-95 °C) combined with a relative low extruder temperature (220-270 °C) and a low cost. The initial filament (Figure 118) is composed by twisted fibers prepreg but not consolidated so it does not have the consistency to be extruded and pushed by the feeding system.

The idea is to consolidate the filament so to achieve a filament that can be 3D printed and verify if this operation can be made without complex and high cost machines, achieving good results in terms of strength. In order to better see and evaluate the degree of prepreg and evaluate how it modifies during the consolidation, an analysis was performed with the Scanning Electron Microscope system (SEM) in "Politecnico di Milano" Mechanical Department. The not-consolidated filament, shown in Figure 119, has PA6 ( $vm = 0.59$ ) nylon with a diameter of 43  $\mu m$  and 12k AS4A carbon fibers ( $vf = 0.41$ ) with a diameter of 7.5  $\mu m$ . In Figure 120 it can be possible to observe that the carbon fibers do not have a smooth surface so it suggests that they are individually prepreg and in some zone they are grouped even if the consolidation process has not performed yet.

A first attempt to consolidate the filament has been done by manually pulling the yarn through the hot nozzle at a temperature of almost 295 °C for PA6 and 285 °C for PA12 filaments so to assure a uniform melting of the nylon fibers and of the nylon coat on the carbon fibers. As shown in Figure 121 the filament has a more compact structure and a more regular diameter. This consolidated filament can be used for printing because the thermoplastic PA resin used as matrix element can be melted more time without degrading the material.

A further step was to use the SEM as already made on the not-consolidate filament, in order to verify the molten nylon distribution along the filament and the level of compaction of the carbon fibers. Figure 122 highlights how the molten fibers of nylon, after the consolidation phase, increase the surface in contact with the carbon fibers and a comparison between Figure 123 and Figure 121 shows how the prepreg carbon fibers itself stick together creating a more compact structure. In this way, even if the compaction speed was not controlled, this test has demonstrated that the consolidation can increase the consistency of the filament allowing it to be used for 3D printing process and that the thin coating of nylon on carbon fibers is sufficient.



Figure 118: Not-consolidated commingled yarn

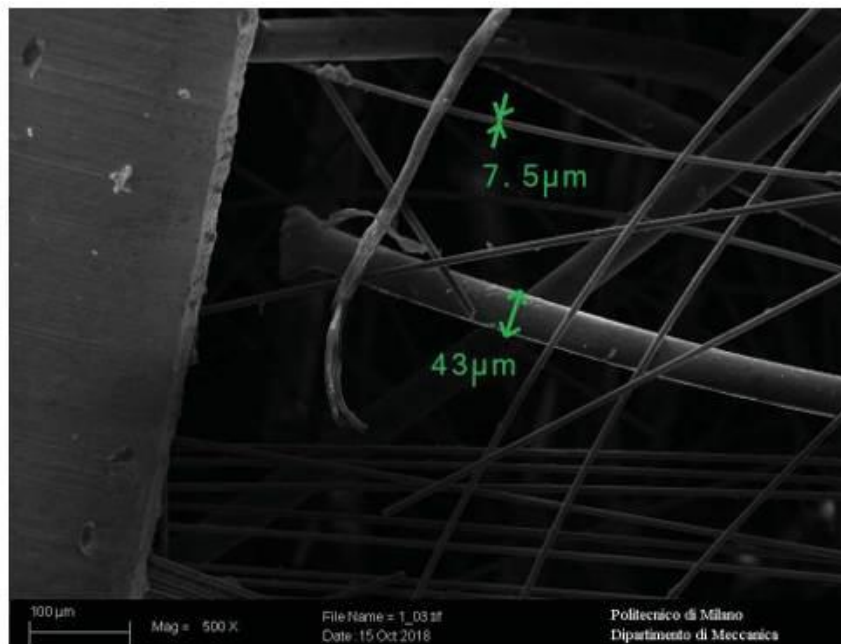


Figure 119: Not-consolidated commingled yarn - SEM 500X

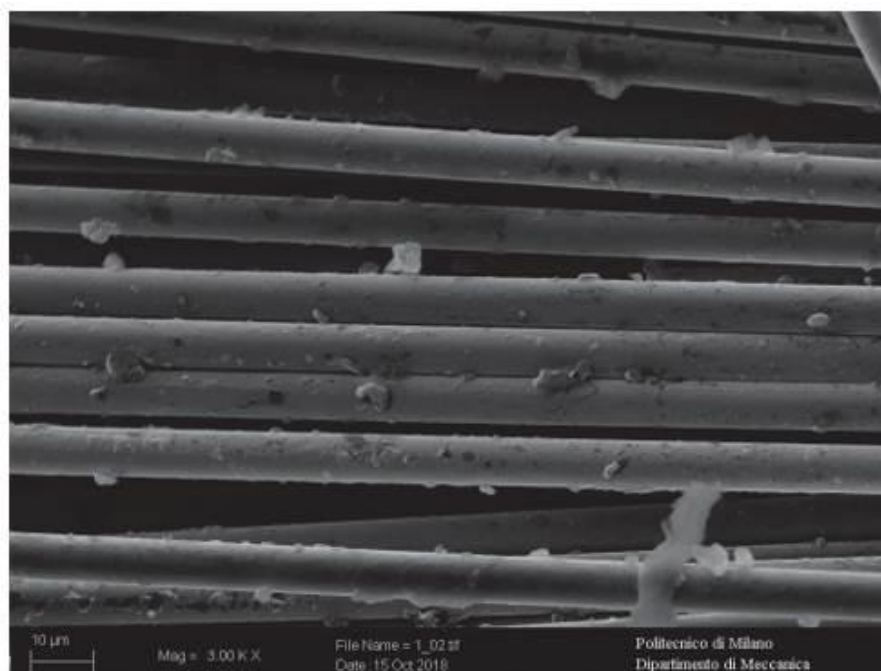


Figure 120: NOT-consolidated commingled yarn - SEM 3.00K X

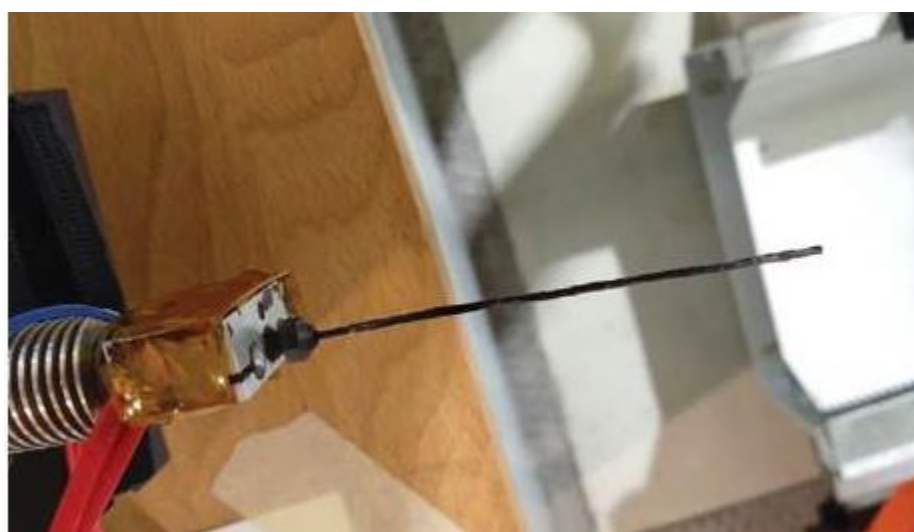


Figure 121: Manual consolidation of commingled yarn

### Filament Tests

At this point it was interesting to perform a tensile test in order to investigate if the consolidation phase has any effect on its mechanical properties. The results are compared in terms of displacement and force, being the filament the same and due to the difficulty to calculate the real diameter of the initial not-consolidate filament and the impossibility to use an extensometer. All the tensile tests have been performed on a MTS machine with a maximum load capacity 150 kN and all filaments have been tested in the same way. The results of the tests related to the PA6 12k AS4A filament are reported in Figure 124. As



you can see the consolidated filament has a maximum strength higher than the not consolidated one. The reason can be traced back to the fact that the twisted fibers of the not-consolidated filament are not all loaded at the same instant and the load drops down as some of them break and rises again as soon as new fibers are tensioned; this behavior lead to a saw tooth curve. In fact during the test the fibers break one after the other and not at the same time. Moreover the nylon in this state is not able to transmit the internal stress among the carbon fibers. For this reason and due to the less compaction state of the fibers, the elongation is very high; however the nylon fibers are very elastic so they contribute to avoid load going to zero. In case of consolidated filament, on the other hand, the fibers break all at the same time and a complete brittle failure of the samples is detected. As already said, in the consolidated filament the carbon fibers are more grouped so that the thermoplastic matrix allows for a better distributing of the load among the fibers.

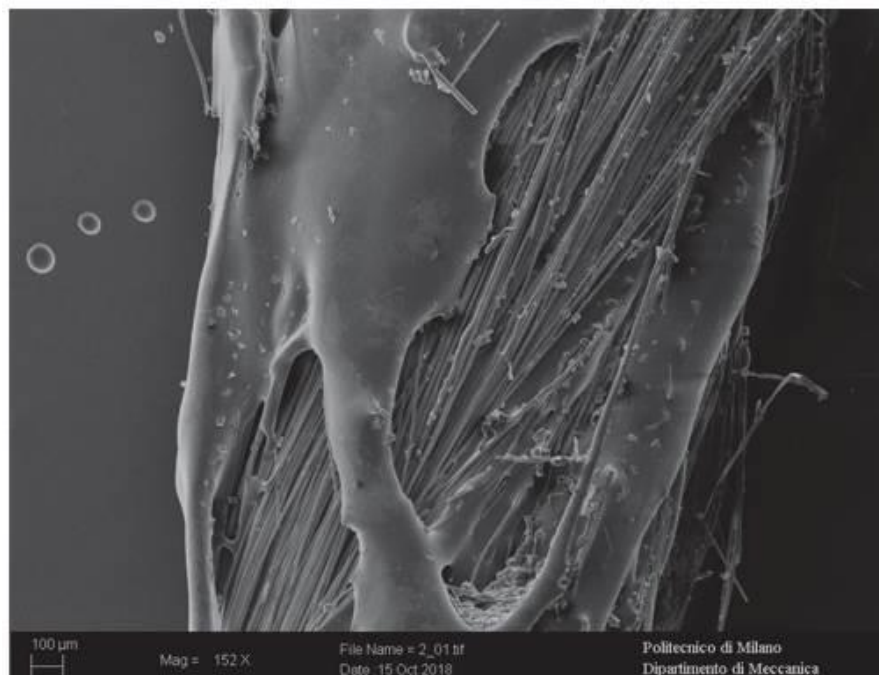


**Figure 122: Consolidated commingled yarn - SEM 152X**

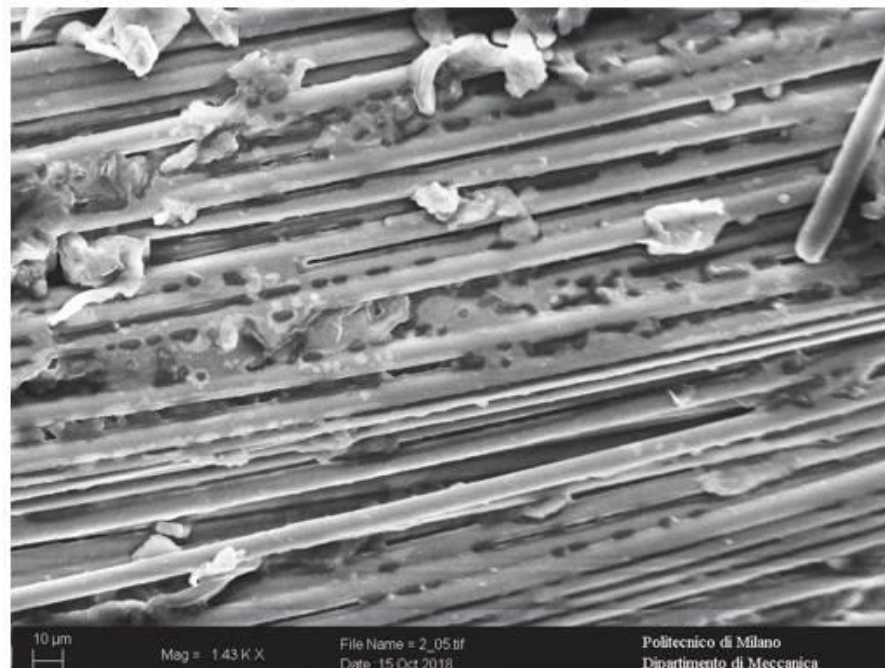


Figure 123: Consolidated commingled yarn - SEM 1.43K X

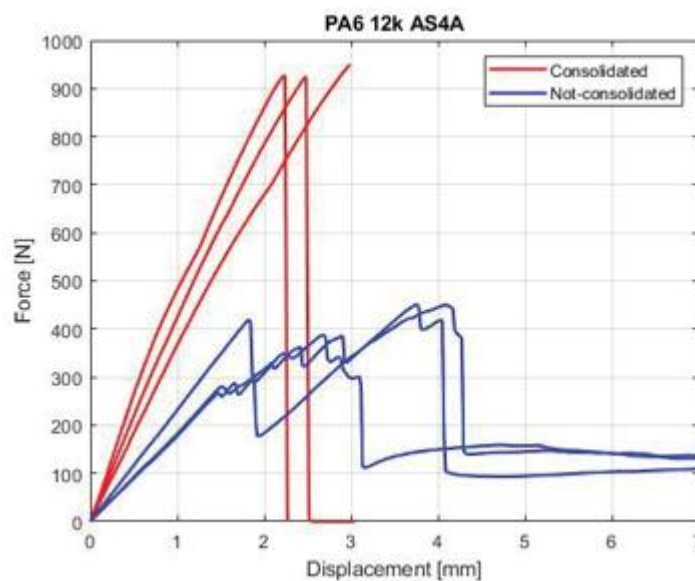


Figure 124: Tensile test comparison between consolidated and not-consolidated filament (PA6 12k AS4A)  
 Figure 125 and Figure 126 show the results respectively for PA12 12k AS4A and PA6 3k AS4C filament. The figures show how all the three kinds of filament have a significant increase of strength after the consolidation.

Table 27 reports the mean value of the breaking load of all the three filaments before and after the consolidation stage and the increment of strength due to this treatment. It will be verified if the strength of the consolidated filament can be maintained or not after the print.



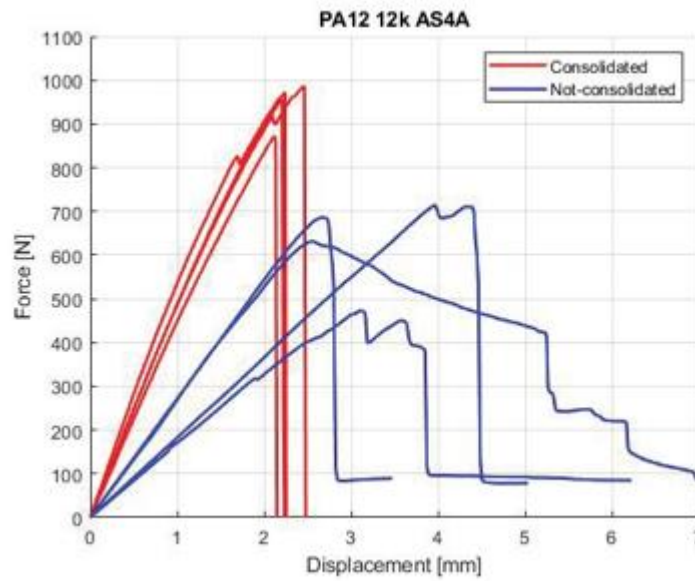


Figure 125: Tensile test comparison between consolidated and not-consolidated filament (PA12 12k AS4A)

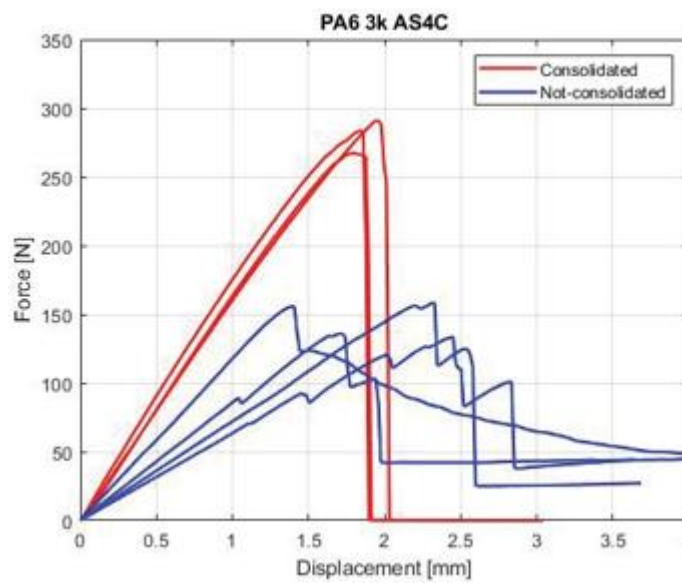


Figure 126: Tensile test comparison between consolidated and not-consolidated filament (PA6 3k AS4C)



**Table 27: Results of filaments tensile test**

	PA6 12k AS4A	PA12 12k AS4A	PA6 3k AS4C
Max load consolidated [N]	934.1	947.3	283.3
Max load not-consolidated [N]	441	626.5	145.9
Strength increment %	52.84	33.86	48.52

The results show how the consolidation of the filament allow to achieve better performances and to have a filament with the needed compactness to allow the extrusion. The next steps will be the evaluation of the best way to let the filament stick on the printing hot bed during the printing. After some trials a temperature of 70 °C has been selected for the heated bed. This temperature coupled with the use of a PVA based glue, that is affine to polyamide thermoplastic material allows the material to stick on the bed. If the hot bed temperature is too high the glue seems to loss its stick capability and the filament does not stick. The glue has been spread not directly on the bed glass, but on a layer of Kapton tape in order to allow a better heat distribution. In order to test if the filament can be 3D printed, it was used the set-up shown in Figure 127, the compaction system has been removed so that it cannot affect the print capability.


**Figure 127: PA12 12k AS4A filament printing test**

In fact, the compaction system can be used only when the filament stick properly and naturally to the bed. The nominal distance between the bed and the nozzle is set to  $0.8\text{ mm}$  (with a deviation of  $\pm 0.2\text{ mm}$  due to the FANUC manipulator positioning precision in Z direction). The consolidated filament has the right compactness and consistency to be feed by the feeding system without any slippage and the thermoplastic PA does not exhibit any problem to be heated up a second time after the consolidation phase; after the print the sample has an appearance similar to the consolidated one and no filament separation appears.

It is interesting to perform tensile tests on a single filament 3D printed in order to evaluate in a quantitative way the goodness of the process and compare the results with the ones previously mentioned. Being the compaction system removed during these prints, the results depends only on the process itself and on the filament behavior. This experiment was performed only PA12 12k AS4A filament (PA6 and PA12 comparison will be made by printing some samples and it will be discussed next) and the results (Figure 128) show that there is an increase of the maximum load that reaches a mean value of  $1108\text{ N}$ . With respect to the consolidated filament, by simply print it, there is a percentage increment of about 14.5%. This increment can be due to the natural compaction of the filament as soon as it came out of the nozzle; the filament is slightly pressed on the hot bed because of the back-pressure.

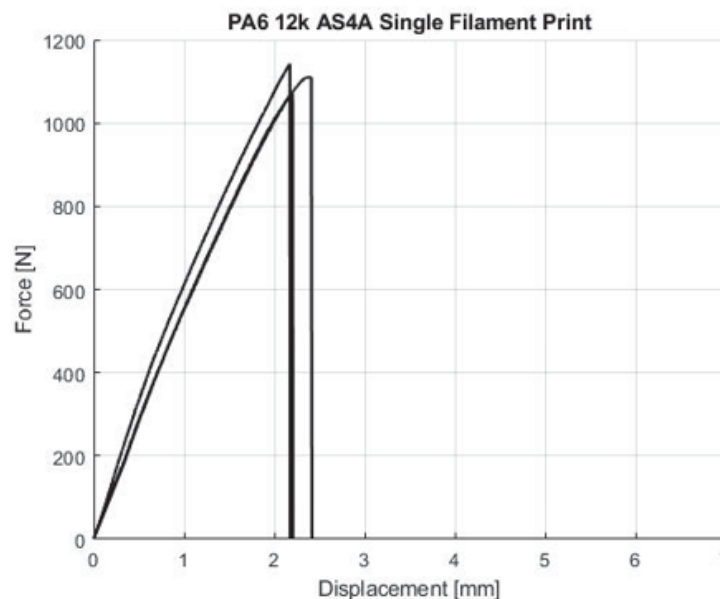
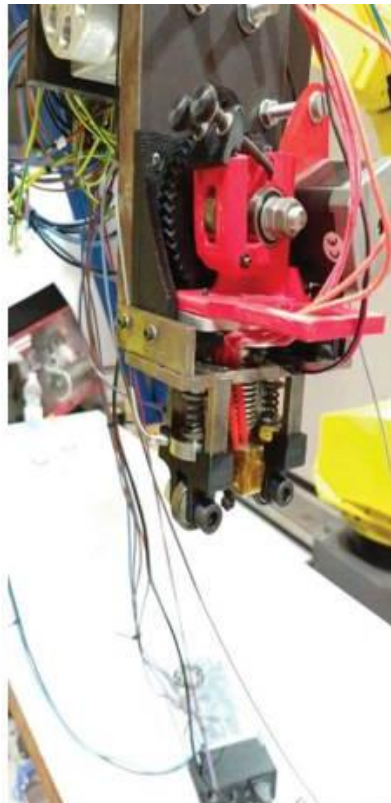


Figure 128: Tensile test of a single PA12 12k AS4A filament 3D printed

## Sample Tests

Once it has been verified that the PA resin easily melts again after the consolidation and the filament can be 3D printed without any slippage in the feeding system, some samples have been printed by using the configuration with the load cells and compression system shown in Figure 129. As for the samples printed by using the TAZ printer, also in this case a tensile test will be performed in order to evaluate the effects of the load applied to compact the layers. As reported in

Figure 130 eight samples for PA6 12k AS4A and PA12 12k AS4A filaments have been printed. Some preliminary tests have been performed in order to choose some printer parameters as the hatching space, the temperatures of nozzle and hot bed, the layer height, and the print speed in order to obtain a good adhesion of the first layer on the bed. The samples are printed by imposing  $0.8\text{ mm} \pm 0.2\text{ mm}$  as nozzle bed distance, hatching space of  $1\text{ mm}$ , a bed temperature of  $70^{\circ}\text{C}$ , nozzle temperature of  $295^{\circ}\text{C}$  for PA6 and  $285^{\circ}\text{C}$  for PA12, velocity of extrusion of  $3.5\text{ mm/s}$ . In order to study the influence of compaction system on the mechanical properties, samples formed by two layers have been printed.



**Figure 129: Head setup for sample printing**



**Figure 130: Samples of PA6 12k AS4A and PA12 12k AS4A**

The external compaction load conditions for the two filaments used are the ones summarized in Table 28 and Table 29.

**Table 28: Tensile test results of PA6 12k AS4A specimens**

	Load [N]	UTS [MPa]	E [GPa]
1	0	167	14.92
2	0	175	15.33
3	40	257	22.93
4	40	225	18.50
5	50	235	28.43
6	50	222	28.34
7	60	209	24.07
8	60	198	18.05

**Table 29: Tensile test results of PA12 12k AS4A specimens**

	Load [N]	UTS [MPa]	E [GPa]
1	0	192	24.86
2	0	191	31.44
3	40	272	32.31
4	40	277	35.46

5	50	237	29.53
6	50	295	29.43
7	60	271	33.11
8	60	291	29.78

Four cases, based on the compaction load, can be identified and for each cases two samples have been printed and tested. The load has been measured by load cells, as reported in previous Chapters for the samples printed by using Markforged filament. However, in this case there is only electric noise and the harmonic components with frequency multiple of 7.3 Hz are no longer present; this confirms that the reason of the force peaks shown on the acquired signal during the print on the TAZ were due to the belt that is not present on robot. In order to eliminate electrical noise with high frequencies (coming from Arduino and electrical circuit), it is possible to use a low pass filter; this operation can be useful if a closed loop control system, based on the applied load measures, will be implemented. During these printing tests, the measures are performed before the start of a print and during it in order to verify the open loop behavior. The springs used on the TAZ (D12400) have been replaced with more rigid springs (D12350) in order to manage with a larger filament. The springs have an elastic constant ( $k_s$ ) of 37.27 N/mm and can exert a maximum force of 200 N.

The applied load is composed by a preload component ( $F_p$ ) and a component due to the spring compression when the roller climbs and presses the filament ( $F_s$ ). The two components are highlighted in Figure 132 and the overall applied force ( $F_l$ ) can be calculated by using equation 21.

$$F_l = F_p + F_s \cong F_p + k_s \cdot \text{layer height} \quad (21)$$

The preload has been set to 10 N, 20 N, 30 N as shown from the acquired signal in Figure 131. The second force component appears only when the rollers act on the filament and compact it; this is due to the displacement imposed to the compaction rollers times the spring elastic constant (about 30 N).

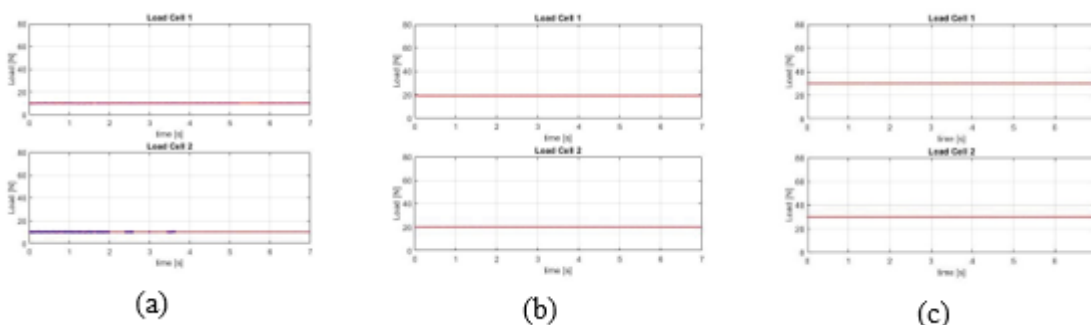


Figure 131: Spring preload: 10N (a), 20N (b), 30N (c)

The combination of these components can be appreciated from Figure 133. In fact, it is visible that when the rollers are not in contact with the filament, the measured load is only the set preload while when the compaction roller acts on the layer, the load is, as already said, the combination of two parts and the final

loads, reported in Table 28 and Table 29, are achieved. The maximum load has been experimentally determined in order to guarantee that the roller can climb the filament at the beginning of the print; in fact, as shown in Figure 134 if the force  $F_x$  is higher than the tangential stick force between filament and plate, the filament slips and the printing process cannot start automatically. Moreover, two samples are printed removing the compaction rollers in order to show the expected lower mechanical properties and highlight the necessity of a compaction system.

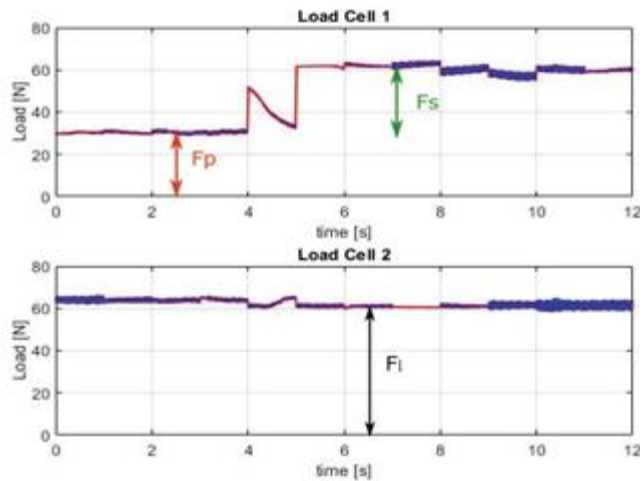


Figure 132: Compaction force components

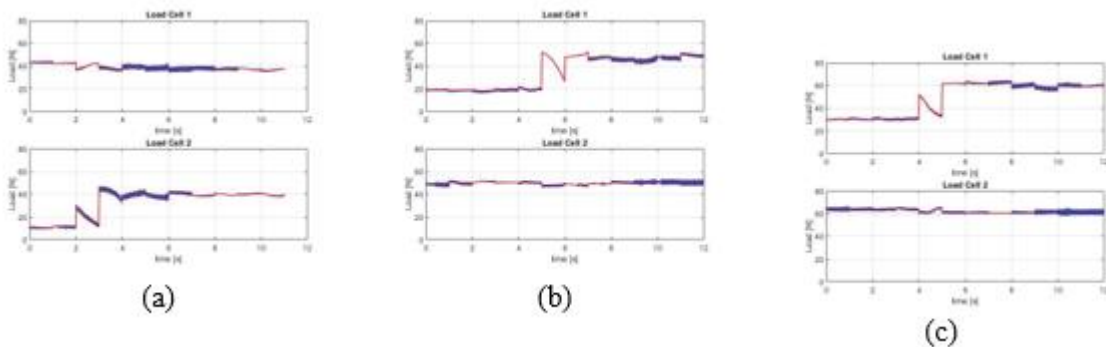
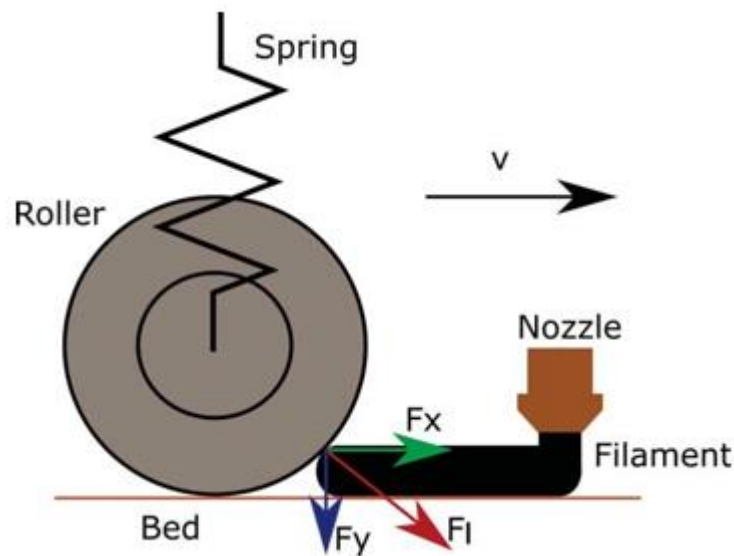


Figure 133: Load cell acquisitions during printing with different spring preload: 10N (a), 20N (b), 30N (c)



**Figure 134: Force between roller and filament at compression start:  $F_i$  is the overall force exerted by the compaction roller,  $F_x$  is the component parallel to the extrusion direction and  $F_y$  is the component in vertical direction**

The samples are tested by means of tensile test performed on a MTS machine with a maximum load capacity of 150 kN and the graphical results are shown in Figure 135 for each specimen. From the tests, UTS and Young modulus have been extrapolated. Figure 136 and Figure 136 show the mechanical parameters as a function of the external applied load. The maximum stresses adopted as an index in the sample comparison. It can be verified that for both filaments, the compaction system is able to increase the UTS value but the PA12 filament is less sensitive to the imposed load in the evaluated load range.

The PA12 filament shows better mean mechanical properties and even if the plastic matrix has a low level of strength if compared to PA6 (PA12 and PA6 tensile strength is respectively about 50 MPa and 74 MPa), with a slightly lower density (1.02 g/cm<sup>3</sup> for PA12 and 1.14 g/cm<sup>3</sup> for PA6), it seems to be more adapt to transmits the stress to the carbon fibers. The results in terms of tensile curves, UTS and Young modulus are however lower if compared with the results obtained with the Markforged filament (lower  $v_f$  than Concordia Fibers filaments) used in the previous tests on the TAZ. The results suggest that even with a manual consolidation, the print process can be performed and the compaction system allow to increase the mechanical properties. However, the manual consolidation is an operation without control on the filament parameters and so by introducing a more deterministic and automatized consolidation stage just before the print, it is possible to increase further the mechanical properties of the specimens. These printing tests allow to verify the capability to achieve high strength-to-weight ratios (results summarized in Table 30) that can reach values higher if compared to the ones of many commercial metallic materials (aluminum, steel and some titanium alloys).

**Table 30: Maximum achieved strength-to-weight ratio for PA6 12k AS4A and PA12 12k AS4A specimens**

	PA6 12k AS4A	PA12 12k AS4A
Strength [MPa]	257	295
Density [g/cm <sup>3</sup> ]	1.4065	1.3357
Strength-to-weight ratio [kN · m/kg]	182.72	220.86

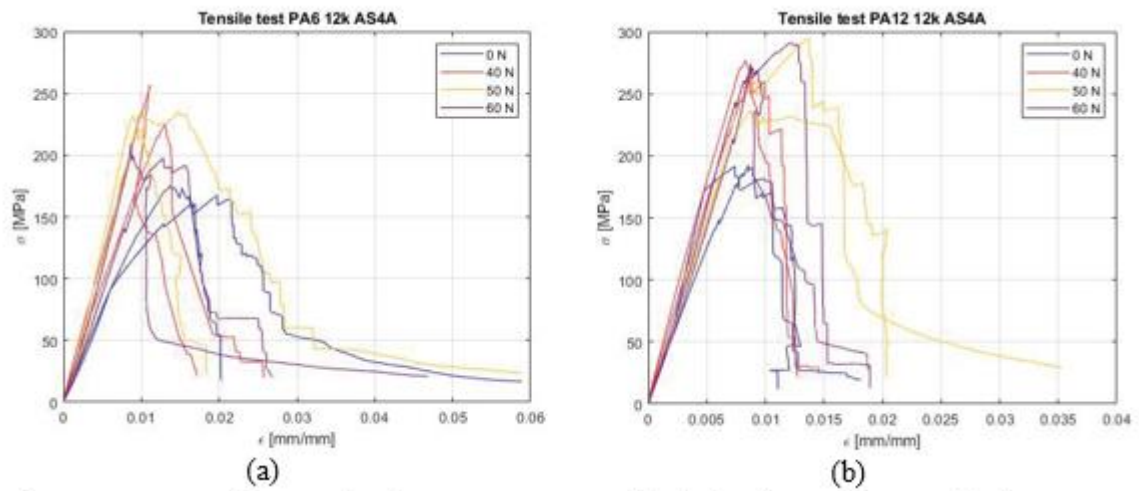


**Figure 135: Tensile test of 12k AS4A PA6 samples (a) and Tensile test of 12k AS4A PA12 samples (b)**

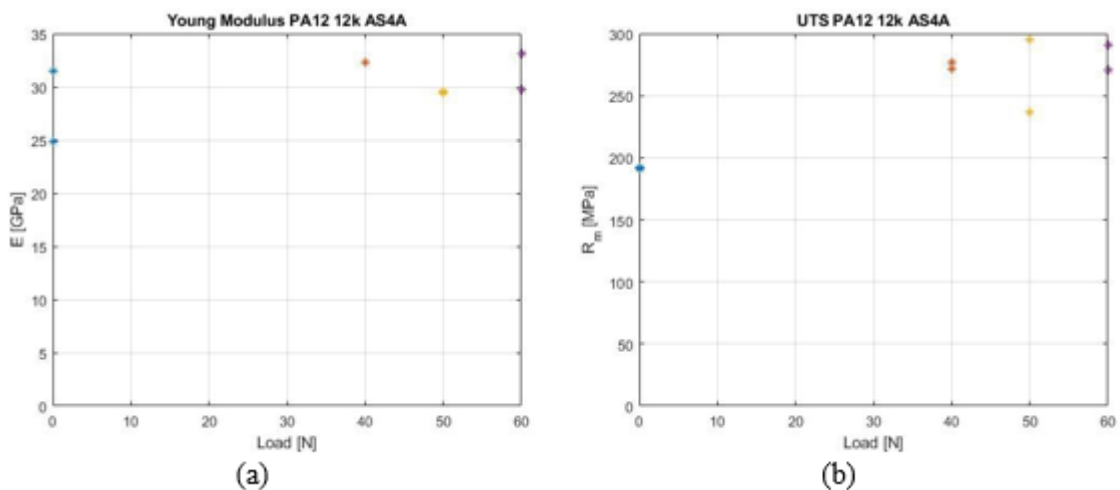


**Figure 136: PA12 12k AS4A: tensile test results of Young modulus (a) and UTS (b)**



## 7. CONCLUSIONS AND FUTURE WORK

The RUN2RAIL project explores an ensemble of technical developments for future running gear, looking into ways to design trains that are more reliable, lighter, less damaging to the track, more comfortable and less noisy. In this contest, one of the main thematic work stream is the “Optimised materials & manufacturing technologies” one.

The use of novel materials and manufacturing methods in combination with intelligent / active suspensions to enable nonconventional running gear concepts were analysed and discussed.

In particular, Additive Manufacturing (AM) was evaluated as an alternative technology in the railway sector, highlighting its strengths. Nowadays, it can be considered the key technology of the fourth industrial revolution, known as "Industry 4.0", which aims to improve the production methods and business models currently used in industrialized countries.

It allows more degrees of freedom for designing and manufacturing components with complex shapes which would be impossible to make through traditional methods. Furthermore, it also allows to obtain lighter structures with topological optimizations.

BLUE performed a concept design concerning a bogie frame and a single axle gear. BLUE identified two structural components in accordance with the SLM (Selective-Laser-Melting) working volume actually at disposal:

- axlebox for bogie
- link arm for the single axle running gear

These components were optimized considering the advantages given by AM. In fact, a lattice structure was defined for the axlebox and an optimized configuration was taken in account for the link. Moreover, the last one includes a joint created directly during the AM process.

A bibliographical research showed that actually the selected components are made generally by steel. For example, axlebox spheroidal cast iron GJS is used. This very ductile iron is also known as nodular cast iron, spheroidal graphite iron, spherulitic graphite cast iron and SG iron. In addition to spheroidal cast iron, light alloy, for example AlSi7Mg is used as alternative to achieve a lighter design.

**Table 31: Axlebox material [35]**

Axlebox material examples					
	Housing EN-GJS- 400-15	EN-GJS- 400-18 LT	AlSi7Mg0.6	Components such as end caps S235JR      S355JO	
Standard	EN 1563	EN 1563	EN 1706	EN 10025	EN 10025
Type	SG iron	SG iron	Light alloy	Steel	Steel
Density (kg/m <sup>3</sup> )	7 100	7 100	2 700	7 800	7 800
Yield limit (MPa)	250	240	210	235	355
Ultimate strength (MPa)	400	400	250	340-510	450-680
Young modulus (MPa)	169 000	169 000	71 000	206 000	206 000
Poisson ratio	0,275	0,275	0,33	0,3	0,3
Elongation (%) <sup>1)</sup>	15	18	1	17-21	14-18

One of the main objectives of the project is to combine the intrinsic lightness of the material (AlSi7Mg) with a further lightening granted by a topological development, and an increase of the mechanical performance allowed by an oxide dispersion.



Therefore, Rina CSM and POLIMI focused on rapid prototyping of components made by this alloy. The aluminium alloy reinforced by alumina dispersoids was analysed to improve mechanical properties for the final application. In particular, Rina CSM manufactured the metal powder through VIGA (Vacuum Inert Gas Atomization), while the additive manufacturing process was performed by POLIMI. Different types of specimens were produced using aluminium alloy powders in SLM process and, subsequently, mechanically and tribologically characterized.

The results obtained show that, in general, the samples produced by the AM process are mechanically and tribologically superior to those obtained by casting. The mechanical and tribological behaviour of ODS specimens and dispersoids - free specimens is comparable, no significant differences were measured in average CoF and wear rate values. Nevertheless, there is still a wide margin for improving the ODS powder characteristics and its processability by SLM.

One of the key factors for a wider use of SLM technology in railway industry is related to the component size manufacturable by the commercially available systems. Figure 137 shows the current platform areas against maximum build height for the commercially available SLM systems. It can be noticed that the technology has been mainly developed for small to mid-sized component manufacturing, where most of the systems are found. Larger components are required by several industries including automotive, aerospace and energy. Therefore, the system manufacturers have been driven towards producing larger machines. Conventional systems currently go up to 800 mm build height with a square based platform area or shorter build heights at 500 mm with a longer rectangular based chamber.

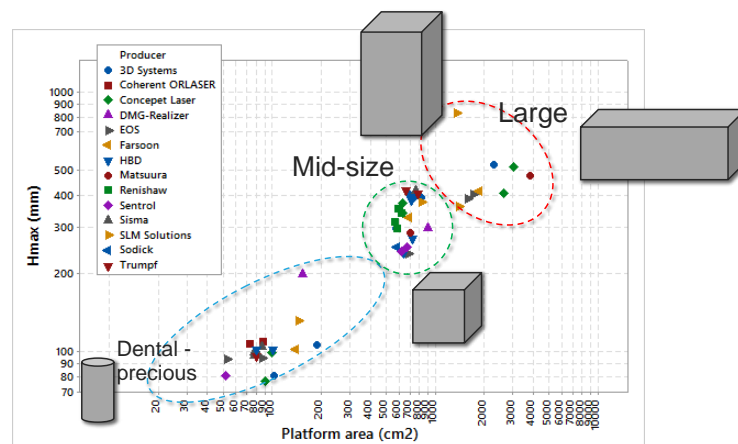


**Figure 137: Commercial SLM machine dimensions and build envelope geometries. Data provided by system manufacturers' websites.**

The drive for producing larger components also accelerated the development of one-of-a-kind or project systems. Aerosuf in South Africa developed a large area SLM system for processing Ti-alloys (see Figure 138). The Adira system from Portugal relies on a tiled SLM process, where the laser head is carried around on a large surface area (1x1 m<sup>2</sup>) with a 1 m build height. GE Additive have demonstrated their Atlas project where the company aims at a build envelope of 1 m<sup>3</sup>. More recently GE Additive demonstrated a rotary powder bed able process large axial-symmetric components. The powder bed is continuously fed with powder on one side (continuous recoating), while the lasers process the powder bed on another side of the rotary bed (simultaneous laser exposure), providing increased productivity. The main issues in producing large SLM systems are related to the increased production time and the management of large

quantities of powder. These issues are expected to be resolved in the upcoming years. However, the cost of these large systems are expected to be significantly higher than the existing commercial systems also due to the employed solutions.



**Figure 138: Aerosud – South Africa 2000 x 500 mm<sup>3</sup>**

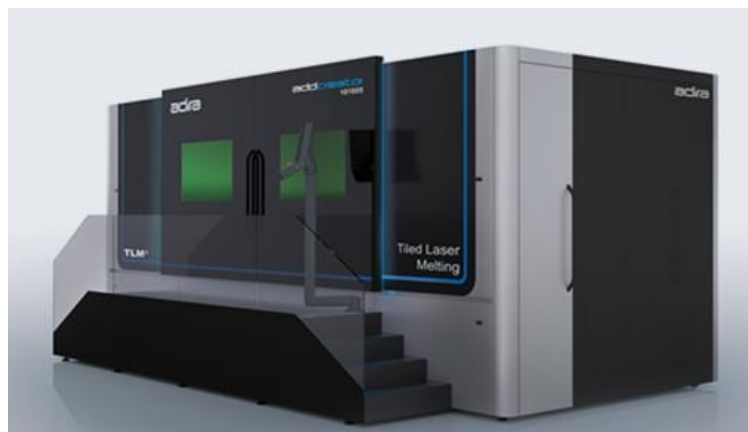


**Figure 139: Adira - 1000 x 1000 x 500 mm<sup>3</sup>**



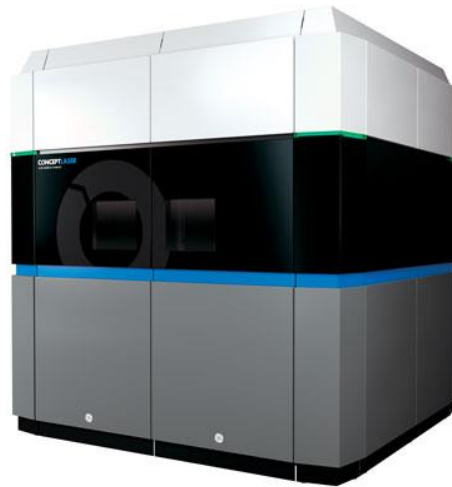


**Figure 140: GE Atlas -1000 x 1000 x 1000 mm<sup>3</sup>**

Moreover, POLIMI contributed in the innovative production of the bogie frame composite material, using a robotic system for the laying of composite fibres. This process enables the laying of the composite fibres according to the direction of stresses in the component as obtained from the structural analysis performed by BLUE. Mechanical properties were simulated and compared with required load cases. In conclusion, both selected additive manufacturing processes (SLM and AFP) resulted very promising to produce lighter components for bogie frame with improved mechanical characteristics.

## REFERENCES

- [1] - <https://www.makepartsfast.com/will-aluminum-become-new-hot-new-material-in-metal-additive-manufacturing/>
- [2] – J.M. Benson, E. Snyders “The need for powder characterisation in the additive manufacturing industry and the establishment of a national facility”, South African Journal of Industrial Engineering August 2015 Vol 26(2) pp 104-114
- [3] – <https://www.globenewswire.com/news-release/2018/02/28/1401368/0/en/SmarTech-Issues-New-Report-Addressing-Opportunities-in-Aluminum-Additive-Manufacturing.html>
- [4] – A. Colaneri “Production of ODS aluminum powders for Additive Manufacturing processes”, Master’s thesis 2019, Università degli studi di Roma Tre
- [5] – Dongdong Gu et al. “Selective Laser Melting Additive Manufacturing of TiC/AlSi10Mg Bulk-form Nanocomposites with Tailored Microstructures and Properties”, December 2014, Physics Procedia 56:108–116
- [6] – Quanquan Han et al. “Selective laser melting of advanced Al-Al<sub>2</sub>O<sub>3</sub> nanocomposites: Simulation, microstructure and mechanical properties”, Materials Science and Engineering: A, Volume 698, 20 June 2017, Pages 162-173
- [7] – Jiubin Jue et al. “Microstructure evolution and mechanical properties of Al-Al<sub>2</sub>O<sub>3</sub> composites fabricated by selective laser melting”, December 2016, Powder Technology 310
- [8] – P.K. Mallick. “Fiber Reinforced Composites Materials”, Manufacturing, and Design. CRC Press, 3rd edition, 2007
- [9] – Yakout Mostafa; Elbestawi Mohamed “Additive manufacturing of composite materials: an overview” Conference: 6th International Conference on Virtual Machining Process Technology (VMPT), Montréal, Canada 2017
- [10] – J. V. Milewski “Whiskers and short fiber technology” Polymer Composites, vol. 13, pag:223 – 236, June 1992
- [11] – Jens Schäfer “Process–structure relationship of carbon/ polyphenylene sulfide commingled hybrid yarns used for thermoplastic composites”, Journal of Industrial Textiles, Vol 45, Issue 6, 2016
- [12] – B.-D. Choi, O. Diestel, Philipp Offermann “Commingled cf / peek hybrid yarns for use in textile reinforced high performance rotors” 1999
- [13] -Konrad Kozaczuk “Automated fiber placement system overview”, Transactions of the institute of aviation, n4 (245), pag. 52–59, 2016
- [14] – Junqiang Wu “Investigation of novel microwave components enabled by additive manufacturing”, PhD at University of Arizona, 2017
- [15] – I. Gibson, D. Rosen, B. Stucker “Additive Manufacturing Technologies - 3D Printing, Rapid Prototyping, and Direct Digital Manufacturing”, Springer, New York, NY
- [16] – M. Grasso and B.- M. Colosimo “Process defects and in situ monitoring methods in metal powder bed fusion: a review”, Measurement Science and Technology, 2017, Volume 28, Number 4
- [17] – D.-A.r Türk, R. Kussmaul, M. Zogg, C. Klahn, B. Leutenecker-Twelsiek, M, Meboldt “Composites part production with additive manufacturing technologies” Procedia CIRP, 66:306 – 311, 2017.
- [18] – S.-Y. Kim et al. “Mechanical properties and production quality of hand-layup and vacuum infusion processed hybrid composite materials for gfrp marine structures” International Journal of Naval Architecture and Ocean Engineering, 6(3):723 – 736, 2014
- [19] – M. L. Chiasson “Low cost processing of commingled thermoplastic composites”, Master’s thesis, Carleton University (Canada), 2012



- [20] – D.H.-J.A. Lukaszewicz, C. Ward, K. D. Potter “The engineering aspects of automated prepreg layup: History, present and future”, *Composites Part B: Engineering*, 43(3):997 – 1009, 2012
- [21] – Aström “Manufacturing of polymer composites” London, UK: Chapman &Hall; 1997
- [22] – M. N. Grimshaw, J. Manuel, L. Diaz “Advanced technology tape laying for affordable manufacturing of large composite structures” pages 2484–2494, *SAMPE*, 2001
- [23] – B. N. Turner, R. Strong, S. A. Gold “A review of melt extrusion additive manufacturing processes: I. process design and modelling” *Rapid Prototyping Journal*, 20(3):192–204, 2014
- [24] – J. Belnoue et al. “Understanding and predicting defect formation in automated fibre placement prepreg laminates”, *Composites: Part A* 102 (2017) 196–206
- [25] – S. Khan “Analysis of wear rate and tribological behavior of aluminum cast alloy A356 and Granite composite at different speeds” *International Journal of Engineering and Advanced Technology (IJEAT)*, 2249 – 8958, Volume-5, Issue-3, February 2016
- [26] – M. Lorusso “Tribological and wear behavior of metal alloys produced by Laser Powder Bed Fusion (LPBF)” DOI: <http://dx.doi.org/10.5772/intechopen.85167>, 2015
- [27] – Erin Quinlan “Structures and composite materials laboratory”(slides) February 2009
- [28] – P.M. Schaefer, T Guglhoer, M.G.R. Sause, K. Drechsler “Development of intimate contact during processing of carbon fiber reinforced polyamide-6 tapes” *Journal of Reinforced Plastics and Composites*, 36(8):593–607, 2017
- [29] – A. Dentelli “Design and testing of a deposition apparatus for additive manufacturing with continuous carbon fibre reinforced thermoplastic polymers” Master’s thesis, Politecnico di Milano, 2017
- [30] - Pedram Parandoush, Dong Lin “A review on additive manufacturing of polymer-fiber composites” *Composite Structures*, 182:36 – 53, 2017
- [31] - ATC Semitec Ltd. “The GT-2 Thermistor” <http://www.atcsemitec.co.uk/gt-2-glass-thermistors.html>
- [32] - Chiachung Chen “Evaluation of resistance–temperature calibration equations for NTC thermistors” *Measurement*, 42(7):1103 – 1111, 2009.
- [33] - FUTEK LTH300 <http://www.futek.com/product.aspx?stock=FSH03968>
- [34] - Haavajõe A., Mikola M., Osali H., Pohlak M., Herranen H. “Experimental study of steered fibre composite production”, *Proceedings of the Estonian Academy of Sciences*, 66:295 – 299, 01 2017.
- [35] <https://www.skf.com/binary/76-62734/RTB-1-03-Axlebox-designs.pdf>

